SAPIENZA
UNIVERSITÀ DI ROMA

Development of a Light Driven Biohybrid Microbot

Scuola di dottorato Vito Volterra
Dottorato di Ricerca in Fisica (XXXVI cycle)

Ojus S. Bagal
ID number 1981279

Advisor
Prof. Roberto Di Leonardo

Co-Advisor
Nicola Pellicciotta

Academic Year 2020/2023

Thesis defended on 23 September 2024
in front of a Board of Examiners composed by:

Prof. Michele Ortolani (chairman)

Prof. Giovanni Volpe

Prof. Silvia Picozzi

Development of a Light Driven Biohybrid Microbot
PhD thesis. Sapienza University of Rome

This thesis has been typeset by LaTeX and the Sapthesis class.

Author's email: inboxojusbagal@gmail.com

to Aai and Baba
and Kanha

Acknowledgments

This journey through my PhD thesis has been filled with challenges, growth, and countless moments of inspiration and support. I am deeply grateful to everyone who has been a part of it.

First and foremost, I owe my deepest gratitude to my advisor, Prof. Roberto Di Leonardo. Your support, insights, and incredible patience have guided me every step of the way. I am truly privileged to have had the opportunity to learn from you. To my thesis referees, Prof. Antonio De Simone and Prof. Giovanni Volpe, thank you for your invaluable suggestions and feedback.

I want to express my deep appreciation to the amazing individuals who have contributed to my journey: Silvio Bianchi, Filippo Saglimbeni, Giacomo Frangipane, Helena Massana Cid, Maria Cristina Cannarsa, Claudio Maggi, Giulia Proia, Carlo Gioretti, Filippo Liguori, Giacomo Donini, Farnoosh Jouleian, and Viridiana Carmona Sosa. Your support, conversations and shared moments of joy have helped me in ways I cannot fully express. Additionally, I am immensely grateful to Irene Iacuitto for her invaluable assistance in navigating the complex Italian bureaucracy, especially considering the challenges posed by my limited language proficiency since my arrival in Rome.

A special thanks to my friend and mentor, Nicola Pellicciotta, for being my guide throughout this microbot journey. I am really fortunate to have the opportunity to work with you and learn from you.

I am grateful to MSCA ActiveMatter ITN for the financial support that made this work possible.

To my parents, Satish and Amita Bagal and to Kanha, thank you for your unconditional love. Your support and sacrifices have been the foundation to my success. To Anna and Aaji, your dreams have always been my inspiration.

I want to give a shoutout to my dear friend who has been my rock throughout this journey. Dolly Katoch, your patience, understanding, and encouragement have meant the world to me. Thank you for being there through the late nights, the frustrations, and the celebrations.

This thesis is a testament to the collective effort, love, and support of all these incredible people.

Grazie di cuore...

Abstract

'The cell attached on a slight rise just on the edge of the stomach. It stood on its own and looked out over a broad spread of the Gastrointestinal System. Not a remarkable cell by any means – it was about 2 μm long, rod-shaped, made of proteins, and had four flagella with rotary motors set in the membrane of a size and proportion which more or less exactly succeeded to stimulate your mind.'
— The Hitchhiker's Guide to the Galaxy.

Escherichia coli (*E. coli*) is a Gram-negative, rod-shaped bacterium that is commonly found in the lower intestine of warm-blooded organisms. Its presence is crucial for human health as it aids in the absorption of nutrients. Growing in aerobic and anaerobic environments, it is highly adaptable and a versatile model organism for different scientific studies.

E. coli has been extensively studied in molecular biology, genetics, and biotechnology due to its relatively simple genome, rapid growth rate, and the ease with which it can be manipulated genetically. It was one of the first organisms to have its genome sequenced, and this accomplishment has paved the way for numerous advances in genetic engineering and synthetic biology. The bacterium's ability to express foreign genes has been harnessed to produce proteins, enzymes, and other biological compounds. An example of this is being used for the production of insulin and bringing down its cost by a huge factor.

In a way, it acts like a biological circuit board, where one can hack into its programming and modifying its properties and behaviour. This also makes it a good candidate to study physical phenomena.

This thesis explores the development, optimization, and applications of microbots that are powered and controlled by such genetically modified *E. coli* bacteria. The important gene modification we do makes the bacteria sensitive to green light, and through this we can gain control over its speed. By integrating biological elements with micro-robotics we investigate different complex phenomena. The research is divided into two main parts: the theoretical foundations and practical applications of microbots, and the methodologies for their fabrication and use in bacterial baths.

The first part of this thesis is regarding the microbot. In the first chapter, we get an introduction to the *E. coli* bacteria, the hydrodynamics of flagellar motion, the gene modification done to make these bacteria and the study of proteorhodopsin, the bacterial light switch. We take an overview of the current trends and principles of microbotics as well as scaling laws of the physical forces on a micron scale and their limitations, framing key research questions guiding this study. The second chapter, focuses on the development and optimization of the microbot design, including the two-photon fabrication parameters and calibration of bacterial chambers. We take a look at the measurement of drag coefficients and the effects of connector length on a two-propeller design.

In chapter 3, we briefly describe the methods used in our studies and present results about the microbot behaviour under uniform illumination and dynamic feedback conditions. We discuss the Development of tracking and control algorithms to enhance microbot efficiency. Chapter 4 focuses applications of microbots for

transporting cargo beads within microfluidic environments and to study geometric optics approximation in self-propelled particles. This chapter also has sections on other projects that have been carried out in the duration of this thesis. These include the investigation of using 3D microstructures, including active pressure around curved boundaries and torque measurement with light mills.

Part 2 of this thesis focuses on the methodologies used in the development of microbots. Chapter 5 is focuses on the two-photon polymerization. This is a versatile tool that can be used in rapid prototype development of 3D structures in micron and sub-micron scale. We also go through the protocols for sample preparation and microbot post-processing that were developed in the course of this study. Chapter 6 explains the techniques used for bacterial cell culture and investigation of bacterial speed using differential dynamic microscopy.

In the course of this thesis, I developed a unique micro-robotic system that integrates bacteria into synthetic 3D microstructures to extract mechanical work. I designed and 3D fabricated the synthetic chassis using the two photon polymerization process, calibrated it for the bacterial cells, developed coating protocols to reduce surface interactions and develop a code to analyze and control the trajectories of multiple microbots continuously captured through the microscope.This system can control individual microbots autonomously and required a multi-disciplinary approach, from research topics in physics, microbiology, synthetic biology, material sciences, robotics and control theory and computer science. This system can find applications in different fields of study.

Contents

Part I

BIOHYBRID LIGHT DRIVEN MICROMACHINES

Chapter 1

An introduction to micro-robotics

Robots are autonomous machines programmed to execute specific tasks. To operate effectively, a robot must have two critical components: actuation and decision-making.

The decision-making system processes external data to determine the appropriate actions. Actuators then carry out these actions based on the system's decisions. This combination allows robots to perform their assigned tasks independently.

As we progress forward, so has our ability to build, study and exploit robots just a few microns in dimensions. Microrobotics is a multidisciplinary field of study, encompassing physics, biology, material science, chemistry and computer science.

Multiple different types of microbots exist depending on the type of actuation, like the use of magnetic microbot [1, 2, 3], light driven microbots [4, 5, 6] and biohybrid microbot [7, 8, 9], however for the scope of this thesis we only focus on biohybrid and light driven micro-robots.

This is because we wanted our system to have precise and independent control over individual agents. While the use of external magnetic fields controls the group dynamics of magnetic microrobots, optically driven microrobots can display self-regulating and autonomous behavior [10].

However, as we delve into this chapter, we will find that this field has very unique set of challenges to overcome. While the same laws of classical physics that govern the macro-world are present in the microcosm, the magnitude of interacting forces changes. Microrobotics is not simply about making traditional robots smaller. It requires having new intuitions and better models to get work done on a very small scale.

We take a look at the scaling of the forces in reference to micro-object and the current trends in light driven and biohybrid microbots, and the progress towards formulation of the research question this thesis is trying to answer.

1.1 Scaling of physical laws

Scaling laws are fundamental principles that describe how various physical properties change with the size of a system. In context of microrobotics and microfabrication,

understanding these laws is crucial for optimizing design, efficiency, and functionality. They govern the relationships between the dimensions of an object and its physical properties, such as mechanical strength, surface area, and volume. These laws are particularly significant in the realm of micro and nanotechnology, where the reduction in size to the microscale or nanoscale can result in dramatic changes in behavior and performance. As objects are scaled down, the surface area to volume ratio increases. This means that smaller objects have proportionally more surface area relative to their volume compared to larger objects.

The characteristic length L is a fundamental dimension of a microrobot, such as its length, width, or diameter, that significantly impacts its physical properties and performance. As dimensions scale linearly with L other physical properties scale differently due to their dependence on volume and surface area. The mass and inertia of the microrobot scale with volume. As L decreases, the robot's inertia decreases proportionally to L^3. Similarly, the weight of the microrobot scales with volume. However, the frictional forces that act on the surface of the microrobot scale with its surface area. As L decreases, surface forces become more significant compared to body forces. Forces like adhesion, surface tension, and electrostatic forces dominate at smaller scales due to their dependence on surface area. As L decreases, materials often exhibit higher relative strength and stiffness. This is due to the reduced presence of defects and the increased influence of surface properties. These scaling effects must be considered in the design of microrobot components to ensure they can withstand operational stresses without deforming or breaking.

Van der Waals forces

Adhesion forces are crucial in the operation and design of microrobots, particularly because these forces become increasingly significant as the size of the devices decreases. Understanding the scaling behavior of adhesion forces relative to other forces is essential for optimizing microrobot performance. Adhesion forces arise from interactions at the surfaces of materials. These forces are always present and can dominate the behavior of small-scale systems, affecting movement, manipulation, and stability of microrobots. Weak intermolecular forces arise from induced electrical interactions, electrostatic forces due to charge distributions on surfaces while capillary forces due to the presence of a liquid meniscus between surfaces. At microscale, adhesion forces can become dominant, affecting the microrobot's ability to move, manipulate objects, and interact with its environment. Microrobot designs must account for the increased importance of adhesion forces. Excessive adhesion can cause unwanted sticking, requiring careful control of contact surfaces. Strategies such as surface coatings and texturing are often used to manage these forces [12, 13]. Microrobots used in medical applications, such as drug delivery, must navigate through complex environments where adhesion to tissues and cells can either aid in targeted delivery or hinder movement [14].

To understand the impact of scaling, consider how the Van der Waals force changes with the characteristic length. The van der Waals force F_{vdW} between a sphere of radius R and an infinite halfspace can be given by

$$F_{vdW} = \frac{HR}{8\pi x^2} \tag{1.1}$$

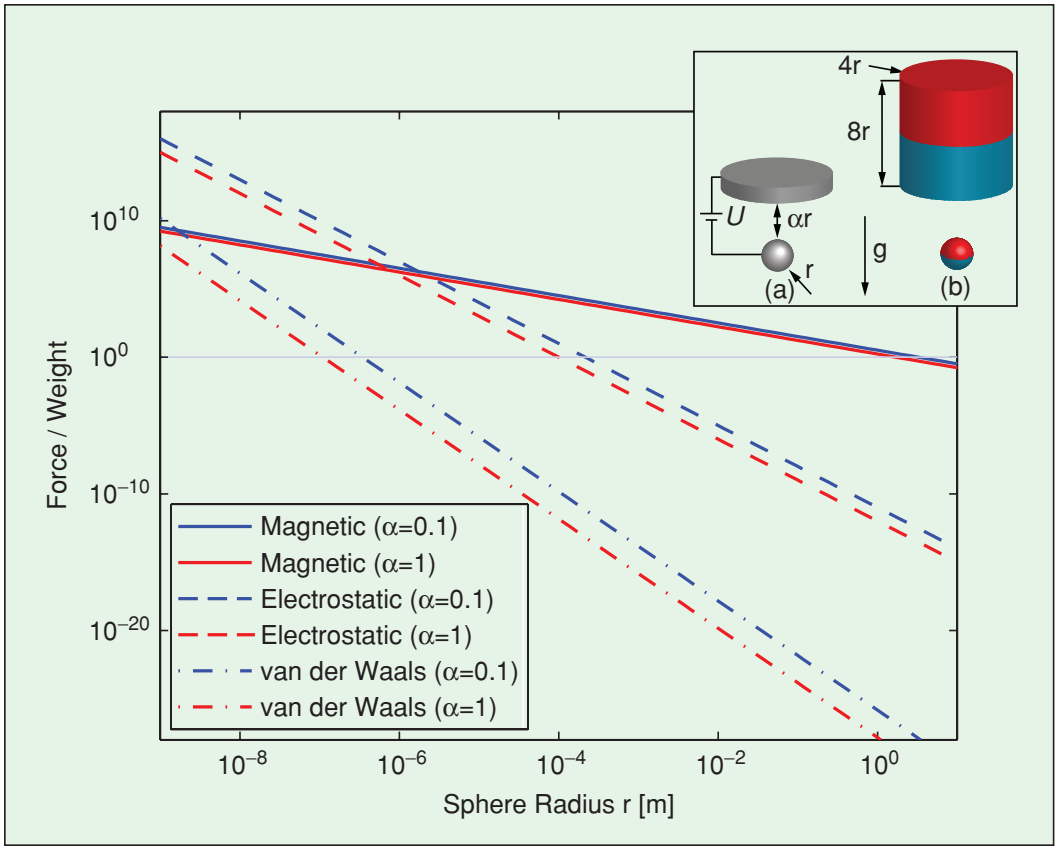

Figure 1.1. Comparison of scaling of attractive forces: Typical values were used in the calculations: density (ρ) of 6.72 $\times 10^3 kg/m^3$, voltage (U) of 100V, and magnetization (M) of 1.1 $\times 10^6$ A/m. When the radius (r) is less than 1 meter, the magnetic force can lift the sphere. For radii smaller than 10^{-4} meters, the electrostatic force surpasses the gravitational force. When the radius drops below 10^{-7} meters, the van der Waals force exceeds the sphere's weight. Figure taken from the reference[11].

where, H is the Hamaker constant, which depends upon the material (typically on the order of 10^{-21}J to 10^{-20}J) and x is the separation distance between the sphere and the halfspace [15].

At close contact $x \approx R$, then

$$F_{vdW} \propto \frac{R}{R^2} = \frac{1}{R} \tag{1.2}$$

Thus, the Van der Waals force increases as the characteristic length decreases, highlighting its growing importance at smaller scales .

Electrostatic Forces

Electrostatic forces also play a significant role in the operation and design of microrobots, especially when considering components like actuators. To examine how the electrostatic force between two surfaces is affected by scaling, we'll look at how capacitance C, voltage U, and charge Q are related, and how these relationships

change with scaling. The capacitance C between two surfaces, in fluid environment is given by:

$$C = \epsilon \frac{A}{\lambda_D} \tag{1.3}$$

where, ϵ is the permittivity of the dielectric material between the surfaces, A is the surface area of the surfaces. and λ_D is the Debye length, which is the lenght at which the electrostatic forces are reduced by a factor of $1/e$.

The relationship between the voltage U applied to the surfaces and the charge Q accumulated on each surface is:

$$Q = CU \tag{1.4}$$

The electrostatic force F between the surfaces can be expressed in terms of the energy W.

$$W = \frac{1}{2} CU^2 \tag{1.5}$$

and the force F between the surfaces can be derived from the change in energy with respect to its Debye length λ_D.

$$F = -\frac{dW}{d\lambda_D} \tag{1.6}$$

The scaling behavior of electrostatic forces between parallel surfaces depends significantly on whether the voltage or charge is held constant and how the dimensions and gap distance are scaled. When only the surface dimensions are scaled, the force with constant voltage F_U scales as $\sim L^2$, while the force with constant charge F_Q scales as $\sim L^{-2}$. When both the surface dimensions and gap distance are scaled, the force with constant voltage F_U remains unchanged, whereas the force with constant charge F_Q still scales as $\sim L^{-2}$ [11].

Magnetic Forces

To examine the scaling of magnetic effects at the microscale, let's see the forces between two identical magnets using the point dipole model. Here, we will provide a explanation of these effects, focusing on how magnetic forces scale with size. For two identical magnets with magnetization M and volume v, aligned along their dipole axes and separated by a distance x, the magnetic field $H(x)$ created by one magnet along its axis can be expressed using the point dipole model.

$$H(x) = \frac{Mv}{2\pi x^3} \tag{1.7}$$

While, the attractive/repulsive force F on the other magnet is given by:

$$F = \mu_0 M v \left| \frac{\partial H}{\partial x} \right| = \frac{3\mu_0 M^2 v^2}{2\pi x^4} \tag{1.8}$$

where, μ_0 is the permeability of free space. Incorporate the fact that the magnetization M remains constant during scaling, as it is an intrinsic property of the material [11].

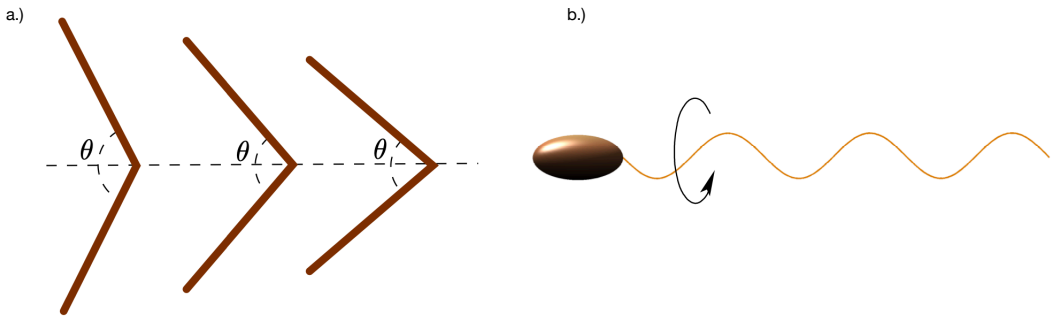

Figure 1.2. Comparison of motion in low Reynolds number(a) Reciprocal motion in scallops cannot provide any propulsion in low Reynolds number, having only one degree of freedom. (b) Propulsion provided in low Reynolds number regime by the cork screw motion of flagellar bundle in *E. coli* [17].

As with electrostatic forces, here as well we have to consider two cases:

1) where scaling the magnets down by L and holding distance x constant leads to $F \propto L^6$ The force scales as $\sim L^6$, indicating very poor scaling. As the magnets become smaller, the force decreases rapidly.

2) where scaling both the magnets and the distance by L leads to $F \propto L^2$. The force scales as $\sim L^6$, which is significantly better. The force remains substantial even as the size decreases.

However, in scenario 2, if we take the force-to-volume ratio instead of just the force, then $\frac{F}{v} = \frac{1}{L}$, meaning the ratio increases as the size decreases. This suggests that the efficiency of force generation per unit volume improves at smaller scales [16].

The figure 1.1 we report the comparison of the scaling behaviour of different forces with respect to each other.

Low Reynolds number hydrodynamics

As most microbots discussed in this thesis are suspended and operate in fluids, we need to take a look at how fluids behave on a micron scale.

To understand the dynamics of objects swimming at the micro-scale it is essential to study the force distribution on the microrobots. We therefore need to solve for the flow field u and pressure p in the fluid surrounding the microbot. In case of an incompressible Newtonian fluid with density ρ and viscosity η, the Navier–Stokes equations states:

$$\rho\left(\frac{\partial}{\partial t} + (u \cdot \nabla)\right) u = \eta \nabla^2 u - \nabla p \tag{1.9}$$

where, the left hand side part of the equation represents the inertial force a fluid element experiences while accelerating and the right hand side represents the intermolecular forces; namely pressure p and viscosity η, exerted by the surrounding fluid elements.

Consider an object, having dimensions L and moving through a fluid with a velocity v for a characteristic time T, the Reynolds number Re is defined as the

ratio between the inertial and the viscous forces and is a dimensionless quantity,

$$Re = \frac{\rho L v}{\eta} \tag{1.10}$$

For water, viscosity is 10^{-3} Pascal· sec and density is 10^3 Kgs/m^3. A human swimming in water with a length in meters and velocity in meter per seconds, Reynolds number in the range of 10^5. However, For a bacterium with lenght of around 2 μm and velocity of around 20 μm/sec this number is very small 10^{-5}.

Now, the force required to move objects in fluid (F) when $Re = 1$ is η^2/ρ [18], i.e.

$$\mathrm{F} = Re\frac{\eta^2}{\rho} \tag{1.11}$$

So, for water, the force required to move an object for a human is around 10^{-4} N, while in the case of bacteria it is 10^{-14} N.

When the Reynolds number is small, the left hand side of equation 1.9 can be neglected, as the viscous forces dominate the inertial forces allowing the fluid dynamics to be expressed by linear stokes equations :

$$\eta\nabla^2 u - \nabla p = 0 \tag{1.12}$$

A special property in low Reynolds number regime can be described as the time derivative in the equation has been removed. This is called kinematic reversibility.

The best way to explain it is using the scallop example 1.2. A scallop like organism that swims using reciprocal motion, can move in high Reynolds number regime. However the same movement would provide no propulsion in low Reynolds number regime, as it is based on a movement which has only one degree of freedom. A way to move in this regime is using cyclic body deformation, like the one in *E. coli*, where it rapidly rotates its flagella to push the surrounding liquid in a cork-screw motion [18]. This will be further elaborated in later in the chapter section 1.2.

1.2 *E.coli* motility in low Reynolds number

The motility of a single (*E. coli*) cell is very efficient and rapid in the low Reynolds number regime. Despite its small size, approximately 2 μm in length and 0.8 μm in diameter, *E. coli* can swim at speeds of up to 20 μm per second. Seeing its motion reveals that *E. coli* alternates between two distinct swimming modes: smooth swimming and tumbling. During smooth swimming, the bacterium moves in a relatively constant direction for about a second. This is periodically interrupted by brief tumbling episodes, during which the bacterium changes direction in an erratic manner [19].

The propulsion of *E. coli* is driven by its flagella, which are helical filaments composed of the protein flagellin. These filaments can vary in length from 5 to 10 μm but maintain a constant diameter of approximately 20 nm. Each flagellum is connected to the hook, which in turn is connected to the rotor. The rotor is the rotating part of the motor, embedded within a complex protein structure forming the stator [20].

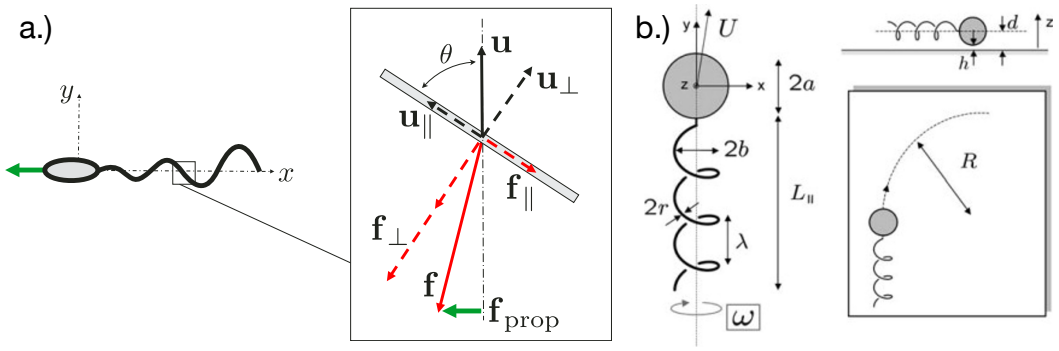

Figure 1.3. Swimming of bacteria in low Reynolds number regime (a) The physics of drag-based thrust in bacteria involves a net force density from fluid that is directed along the helix axis due to the larger fluid drag for motion of the local perpendicular. This also results in a generated net moment that opposes the rotation, causing the cell to counter-rotate.[23]. (b) Mechanical model of E. coli swimming near a solid surface.When it spins around the y-axis, the cell body is close to the surface. In the x-direction, a viscous force affects the cell body. The bacterium's rotation around the z-axis is influenced by both the cell body and the helical bundle. [24]

The flagellar motor is situated in the cell envelope, which consists of a cell wall positioned between two plasma membranes: the cytoplasmic membrane and the outer membrane. The inner membrane is slightly permeable to protons, while the outer membrane, embedded with porins (ion channels), allows protons to pass through, thus equilibrating the periplasmic pH with the external environment [21].

As protons translocate into the periplasm space, an electric potential is generated across the inner membrane, which acts as a dielectric in a capacitor. This electric potential drives the rotation of flagellar motor, enabling the bacterium to swim. The motor operates with impressive efficiency, converting chemical energy into mechanical work, thus propelling the cell through its aqueous environment.

1.2.1 Hydrodynamics of flagellar motion

The direction of flagellar rotation in *E. coli* plays role in its run-and-tumble swimming behavior. Flagella can spin either clockwise (CW) or counterclockwise (CCW), and these rotations dictate the swimming patterns of the cell. When all flagella spin CCW, viewed from the end of a filament towards the motor, they form a cohesive bundle that propels the cell forward in a steady motion along its long axis. This phase is known as the "run" state. In contrast, when one or more flagellar motors switch to spinning CW, the flagellar bundle disassembles, resulting in the independent motion of the flagella. This causes the cell to reorient in a erratic manner, a behavior described as "tumbling."

This motility system allows *E. coli* to navigate efficiently, adjusting its swimming patterns in response to environmental stimuli [22].

The rotating flagellum of a bacterium experiences a net hydrodynamic moment that resists its rotation. This also produces drag force along its axial direction that enables the generation of drag-based thrust, which is essential for bacterial propulsion (see figure 1.3 a) [25].Typically, bacterial flagella rotate at a frequency

of approximately 100 Hz. To remain torque-free, the cell body counter-rotates, at a lower frequency of around 10 Hz. [26, 27]. The interaction between the rotating flagella and the counter-rotating cell body enables effective propulsion through the environment. Locomotion powered by helical filaments relies on this mechanism; without the cell body, the necessary torque balance cannot be achieved [28, 23, 29].

Typically, this forward movement occurs approximately in a straight line. However, when the axes of flagellar filaments are not perfectly aligned with that of the cell body, the bacterium follows helical paths with small amplitudes. This slight misalignment introduces a subtle curvature to the trajectory, causing the bacterium to trace out a helical path rather than a perfectly straight line (see figure 1.3)[30].

The behavior of bacteria is significantly influenced by the presence of surfaces. One of the most notable effects is the tendency of swimming bacteria to be attracted to surfaces [31, 32]. This phenomenon results in a marked increase in bacterial concentration near boundaries. Studies have shown that the steady-state concentration of swimming bacteria can increase up to tenfold near surfaces compared to their concentration in the bulk fluid [33].

A feature of bacteria swimming near surfaces is the qualitative change in their trajectories. While flagellated bacteria far from walls typically swim along straight or wiggly paths between reorientation events, their trajectories near rigid surfaces become circular. When viewed from above the surface in the fluid, these circular paths are typically clockwise (CW). This change in swimming behavior near surfaces can be attributed to hydrodynamic interactions between the bacterial flagella and the surface. The proximity to a boundary alters the flow fields generated by the rotating flagella, resulting in a circular motion [34, 35].

1.3 Light driven microbots

Harnessing light as an external energy source to power microrobots offers several benefits. These advantages include wireless, remote control capabilities with high spatial and temporal precision, as well as dynamic programmability. Depending on their operational mechanisms, light-driven microrobots can be broadly categorized into two primary types: 1) Optical and Optoelectronic Micromanipulation and 2) Light deformable Microrobots. These categories are defined by their propulsion methods, although some microrobots may employ multiple strategies and thus fall into more than one category.

Optical and Optoelectronic Micromanipulation Microrobots utilize optical micromanipulation technologies to control and adjust optical or other physical fields, which generate actuation forces on the microrobots [36, 37, 38, 39, 40]. Light deformable microrobots, on the other hand, depend on the interaction between light and photosensitive, mechanically responsive soft materials such as liquid crystal polymers (LCPs) to function like artificial muscles [4, 41, 42, 43].

Finally, other optical microrobots use photochemical reactions to generate propulsion forces, thereby converting chemical energy into mechanical motion [44, 45].

1.3.1 Optical and optoelectronic micromanipulation microrobots

Since their creation, optical tweezers have found applications across various natural science fields, including manipulating bacterial cells and viruses [46], measuring the mechanical strength of DNA molecules [47, 48], micro and nano-assembly, trapping and manipulating neutral particles and atoms [49, 50]. The system functions by transferring photon momentum to particles when laser light interacts with them, enabling particle trapping near the beam focus due to the intensity gradient force. Additionally, the optical radiation pressure force, which arises from the absorption and scattering of light by the object, also plays a role in the trapping mechanism. By precisely balancing the optical gradient force and optical radiation pressure force, the position of the sample can be controlled in three-dimensional space. Furthermore, light possesses angular momentum, which can be utilized in optical tweezers. For example, in a circularly polarized optical field, the electric field vector rotates in a plane perpendicular to the wave's direction. If an object alters the light's polarization state (e.g., from circularly polarized to linearly polarized), a torque is exerted on the object, causing it to spin due to the conservation of momentum [49].

A standard optical tweezers system comprises several key components: a laser source that generates the coherent light needed for trapping, an optical microscope setup that allows for the visualization and precise focusing of the laser beam, and a polarization controller that converts the typically linearly polarized laser light into a circularly polarized state with angular momentum using a quarter-wave plate. For manipulating microrobots, holographic optical tweezers (HOT) are commonly employed. These systems are equipped with a spatial light modulator (SLM) that can produce multiple Gaussian light beams, enabling the simultaneous control and manipulation of several microrobots. This technology ensures stable control by providing a holding force at multiple points [51].

Microbots utilizing optical tweezers

The optical tweezer (OT)-actuated birefringent microrobot, as demonstrated in [52], serves as a prime example of this technique. Fabricated using electron-beam lithography patterning, this microrobot resembles a microgear with nano-sized trenches in the center. When exposed to a circularly polarized light beam, the microrobot can rotate at a controllable rate by acting as a half-wave retardation plate, effectively harnessing angular momentum from the light beam. This design facilitates precise rotational control, which is essential for applications requiring fine mechanical movements (see figure 1.4 a, b).

Another noteworthy microrobot is the syringe-function microrobot [5], fabricated using two-photon polymerization (TPP). This microrobot features a hollow body with four spheroidal handles and is equipped with a syringe-like function. It has two openings: one for loading and ejecting cargo and another at the top, which allows for the generation of photothermally induced convection currents. This OT-actuated microrobot can load, transport, and unload cargo such as dielectric microbeads. Laser beams provide the actuation force and create photothermally induced convection currents for unloading cargo (see figure 1.5 a).

Several spinning microrobots actuated by OT have been utilized to generate

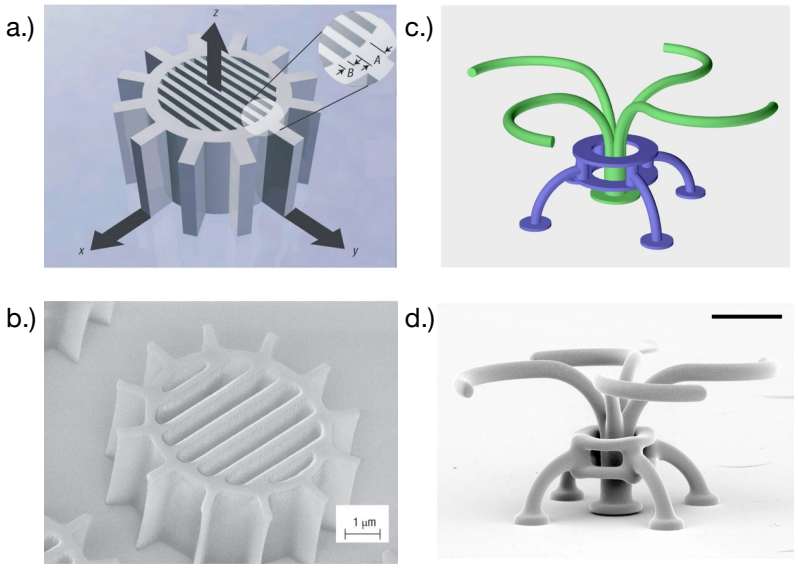

Figure 1.4. Optical tweezer microbots (a) Schematic of birefringent microrobot. (b) SEM image of birefringent microrobot. A one-dimensional photonic crystal is created on the microgear using geometric anisotropy, resulting in the fabrication of microgears with a known birefringence. These microgears are then manipulated within a standard optical trap by rotating them and controlling the input polarization. [52] (c) Schematic of optical turbine microstructure. (b) SEM image of optical turbine microstructure. 3D Structures that are able to redirect incoming optical power accurately into several output channels. These micro-turbines use optical reactions to efficiently harness the momentum of light and produce a powerful, consistent, and adjustable torque. [53]

micro-vortices and exert hydrodynamic forces to manipulate or influence surrounding objects. These microrobots can create localized fluid flows, beneficial for applications in particle sorting, mixing, and targeted delivery [54, 55, 56, 57]. To improve the efficiency of converting optical energy into rotational movement, microrobots with beam-shaping structures have been designed, fabricated, and demonstrated. These structures redirect the input light beam and effectively capture optical momentum, enabling more efficient rotational motion. Such microrobots are ideal for applications requiring high-efficiency energy conversion and precise control of rotational dynamics (see figure 1.4 c, d) [53, 58].

The use of OT-actuated rotatable microrobots to generate hydrodynamic forces for indirect optical manipulation has garnered significant research interest in recent years. This approach enhances the capabilities of OT technology for manipulating delicate and light-sensitive biological samples that are challenging to handle directly with OT. By generating micro-vortices and exerting hydrodynamic forces, these microrobots can influence or manipulate surrounding objects without direct contact, thus preserving the integrity of fragile samples.

Microbots utilizing optoelectronic tweezers

Optical tweezers (OT) generate forces on the order of piconewtons (10^{-12} N). This constraint limits the size and material choices for microbots, as well as their

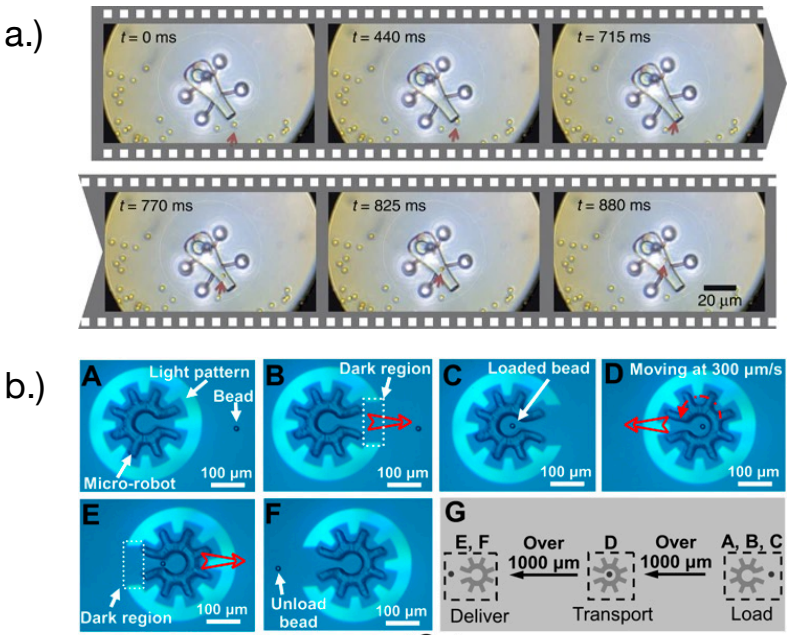

Figure 1.5. Optical tweezers and Optoelectronic microrobots (a) Syringe function optical tweezers microbot. The 3D robot can load and unload cargo by utilizing photothermally induced convection currents within its tool body. [5]. (b) Cog wheel functional Optoelectronic Microbot. An image of a microrobot shaped like a "cogwheel," with a partially enclosed central chamber and an opening on one side is depicted. Bright and dark regions are created on the substrate to form "virtual electrodes," which generate a non-uniform electric field in the liquid medium above the substrate. This electric field interacts with objects in the liquid, creating a force called dielectrophoresis (DEP) that can manipulate their positions. [59]

potential applications. While multiple microbots can be manipulated simultaneously using OT, this requires sophisticated and costly beam-modulation equipment and control software, increasing the system's complexity and expense. To address these challenges, alternative optical micromanipulation technologies, such as optoelectronic tweezers (OET), which offer improved capabilities and broader application potential have been exposed.

Optoelectronic tweezers (OET), invented by Ming C. Wu and his team in 2005, offer a powerful alternative for optical micromanipulation [60]. Unlike optical tweezers, which require a coherent laser light source with high optical intensities, OET utilizes light-induced dielectrophoresis (DEP) force[59].

OET systems typically use a digital micromirror device (DMD) with an LED to project animated light patterns onto a photoconductive substrate, often made of hydrogenated amorphous silicon (a-Si:H). The photoconductive substrate exhibits unique properties: it acts as a resistor in the dark but transforms into a conductor when illuminated[61, 62]. By creating bright and dark regions on the substrate, "virtual electrodes" are formed, inducing a non-uniform electric field in the liquid medium above the substrate. This field interacts with objects in the liquid, producing a DEP force that can control their positions [63].Compared to optical tweezers, OET can exert stronger manipulation forces (on the order of nanonewtons, $10^{-}9$ N) and

handle larger objects (over 100 micrometers). Additionally, OET is well-suited for parallel manipulation, capable of creating thousands of traps simultaneously, making it an ideal tool for controlling multiple microbots and those with larger features.

Another application of OET is the actuation of a "cogwheel"-shaped microrobot. This microrobot, over 200 micrometers in size, can be mass-produced using UV-curable polymer materials and standard photolithography techniques. A negative relief of the microrobot's perimeter is created using a light pattern, producing a negative DEP force that traps the microrobot in the "dark" central region of the projected light pattern. By manipulating this light pattern, the "cogwheel"-shaped microrobot can be programmed to move, rotate, and perform complex, multi-axis operations. One notable application demonstrated involves a sequence of operations—"load," "transport," and "deliver"—which can be used to manipulate micron-sized payloads, such as mammalian cells. This method has shown to exert less stress on delicate biological samples compared to direct OET manipulation (see figure 1.5 b)[6]. Another advanced application involves a "cogwheel"-shaped micromotor, which can generate localized hydrodynamic forces to control the motion of nearby micro-objects. Multiple micromotors can work together as micromachines, such as a touchless microfeed roller that controls microparticle movement in three dimensions. The coordinated motions of multiple micromotors can form various micromechanical systems, including micro-gear trains. For instance, a micro-gear train can consist of an active micromotor driving the rotation of a passive micromotor, effectively transferring mechanical momentum. By adjusting the sizes and configurations of the micromotors, torque multipliers with mechanical advantages greater than one can be created, amplifying the input torque. Additionally, micro-rack-and-pinion systems have been developed to convert rotational motion into linear movement, useful for applications like microfluidic valves controlling flow within channels [64]).

Microbots utilizing optically inducted thermal gradient

Optically induced temperature gradient relies on creating temperature gradients through light absorption. By designing the temperature gradient and leveraging the mechanical response of microrobots to this gradient, various microrobots can be developed for micromanipulation and micro-assembly applications [65, 66].

An example is a microrobot with a rocket-like triple-tube structure that is actuated by a near-infrared (NIR) laser. The laser causes the tail of the microrobot to heat more than the head, creating an asymmetric temperature gradient. This results in a thermophoretic force that propels the microrobot forward. This microrobot can achieve a moving speed of 2.8 mm/s in a blood-mimicking viscous glycerol solution and can be tracked , such as in the ear of a mouse, using photoacoustic imaging.

Other examples include microrobots actuated by optothermal mechanisms where a laser focused on a photothermal substrate creates a surface bubble. This bubble can act as a microrobot to translate, rotate, lift, and drop micro-parts, assembling them into interconnected entities. By controlling the laser's power and position, the bubble microrobot's generation, growth rate, and motion can be precisely managed. This method has been demonstrated for applications such as microtissue fabrication and studying cancer metastasis [67, 68].

Light deformable soft microrobots

The use of flexible polymeric materials with smart behavior presents considerable opportunities for advancing light-driven microrobots [41, 69, 70] (see figure 1.6 c, d). In contrast to optical and optoelectronic micromanipulation microrobots, which are made from rigid polymeric materials with fixed shapes, light deformable microrobots employ smart materials that can alter their shape in response to environmental stimuli. The adaptability of these materials is largely influenced by their formulation, with typical Young's modulus values ranging from tens of kPa for hydrogels [71] to MPa for liquid crystalline networks (LCNs) [72]. The Young's modulus for materials created using two-photon polymerization has not been extensively investigated and may significantly differ from macroscale values. These smart materials are ideal for constructing microrobots that emulate the functional properties of biological tissues or microorganisms [73]. In these microrobots, light acts solely as an energy source, while the microrobot structures perform mechanical tasks such as gripping and movement through dynamic shape changes.

Hydrogels, which are hydrophilic networks capable of retaining substantial amounts of water, are particularly valuable in microrobotics, especially for microrobots designed to operate in liquid environments. Chemically crosslinked hydrogels are of special interest due to their versatility. By incorporating thermoresponsive polymers such as poly(N-isopropylacrylamide) (PNIPAm), these materials can undergo shape changes by modulating their degree of swelling. This shape transformation is spatially isotropic and fully reversible upon cooling [74].

To harness the shape-changing capabilities of these materials for microrobotic tasks, various methodologies have been developed to control or direct their deformation. A prominent example is the microgripper, which mimics the structure of a Venus flytrap Ṫhis device comprises a polymeric bilayer, where a PNIPAm layer is paired with a non-thermoresponsive hydrogel made from polyethylene glycol diacrylate. The fabrication process involves two-step photolithography. The differential swelling properties of the two layers cause the microgripper to close in water and open when heated to $40°C$ due to the deswelling of PNIPAm. Further enhancement is achieved by doping the responsive PNIPAm layer with graphene oxide particles, enabling shape control through near-infrared (nIR) light. When irradiated by a 785nm laser, the hydrogel heats up due to dissipative effects, leading to complete deswelling within a subminute timeframe. This allows the microgripper to open and release a cargo stored inside its closed form upon light activation [75].

Möller and colleagues developed a method to replicate both flagella and cilia using light-responsive hydrogels. Their approach focused on bilayer compositions with asymmetric swelling of the PNIPAm layer. By doping the hydrogel with gold nanoparticles, they achieved rapid heating, with temperature increases of over $20°C$ in milliseconds upon near-IR laser irradiation. This rapid heating, achieved with short light pulses, introduced asymmetry in the otherwise isotropic deswelling process due to nonequilibrium conditions where temperature changes outpace volume adjustments, leading to asymmetric shape deformation. Furthermore, they enhanced the 2D printed microstructures by sputtering them with a rigid gold "skin," enabling the creation of various 3D shapes . By adjusting parameters such as the thickness of the PNIPAm and gold layers, spiral, helical, or hollow-tube 3D structures from the

same 2D hydrogel microstructures have been produced [76]. These 3D structures were fabricated using photolithography. For instance, the helical structure, when irradiated for 80 milliseconds, unwound and then reversed its twisting direction. This deformation and recovery process exhibited nonreciprocal changes in both the length and diameter of the spiral. By adjusting the irradiation sequence to 16/20 milliseconds on/off, the helix rotated along an axis perpendicular to its long axis. In confined environments, such as between two glass surfaces, this structure exhibited directional motion displacement. This method shows great promise for motion and manipulation in microfluidic channels, which are crucial components of lab-on-a-chip devices that are gaining significant attention for various applications (see figure 1.6 b)[77].

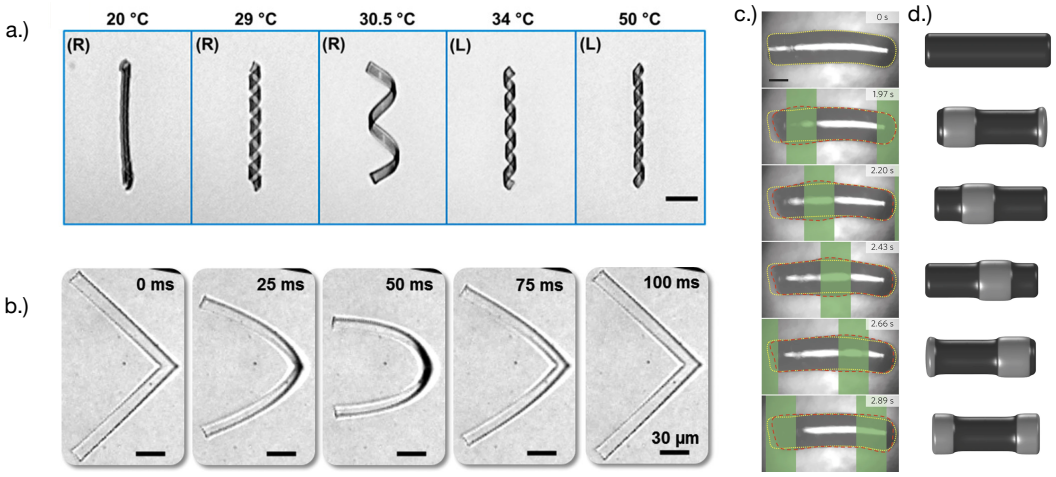

Figure 1.6. Light-responsive hydrogel microbots (a) Microbot based on bilayer compositions with asymmetric swelling. The concept relies on the capacity of tiny hydrogel particles to experience intricate, high-magnitude movements when changes in volume are connected to distortion patterns under non-equilibrium circumstances.[76]. (b) Photothermal actuation of an L-shaped hydrogel ribbon. The microrobot's composition involves a microgel and is powered by the non-equilibrium volume changes controlled by light. The microgel's photothermal reaction, which contains plasmonic gold nanorods, allows for rapid heating and cooling dynamics. [77]. (c) Deformation of an anchored cylindrical microrobot under a periodic light pattern. (d) Simulation result. Artificial microswimmers that create traveling wave movements to propel themselves without requiring external forces or torques. [4]

An intriguing case involves crawling robots, where reciprocal actuation, such as a simple contraction-expansion cycle, has been shown to enable efficient movement by exploiting head-to-tail asymmetry of surface friction on ratchet surfaces. Microrobotic crawlers made from photoresponsive PNIPAm embedded with gold nanoparticles, and arranged in a simple shape with dimensions of $100\mu m \times 50\mu m \times 30\mu m$, exhibit a contraction-expansion cycle when irradiated on one side. This results in net displacement due to the friction hysteresis cycle with the surface during the deformation process. The movement direction is parallel to the line connecting the irradiation spot to the robot's center of mass, allowing precise control over the crawling direction. This concept was also demonstrated with a U-shaped microrobot. By irradiating one of its rectangular elements, the U-shaped microrobot can be

steered within the movement plane. Alternatively, simultaneous irradiation of both ends can induce straight movement [78].

Liquid crystalline soft microrobots

Another promising class of soft materials for light-driven microrobotics includes liquid crystalline elastomers (LCEs) and liquid crystalline networks (LCNs) [4, 41, 79, 80, 81, 82] . These polymers are created by incorporating liquid crystal (LC) moieties, or mesogens, into a polymeric network, resulting in an anisotropic molecular structure. When exposed to stimuli such as heat, the molecular order is gradually disrupted, causing the entire material to deform. Specifically, contraction occurs along the liquid crystalline alignment direction, while expansion happens in the perpendicular direction [80].

A notable feature of LCEs and LCNs is the reversibility of the movement once the stimulus is removed, and the ability to program various deformations solely by adjusting the LC alignment [4, 81, 83]. Unlike hydrogels, LCNs do not require bilayer structures or crosslinking gradients to achieve out-of-plane movements. Additionally, LCNs can function in environments other than water, as deformation can occur in other solvents. The engineering of LC alignment can easily induce bending, torsional, or rotational movements, making these materials highly versatile for a range of applications in light-driven microrobotics [84].

Various bioinspired light-sensitive robots based on light-sensitive LCEs, with dimensions ranging from millimeters to centimeters, have been described [85, 42]. However, scaling down to the micrometer level to produce LCE-based microrobots is less common, likely due to the challenges associated with material actuation at smaller scales [4]. Palagi et al. addressed this challenge by utilizing LCNs prepared through the photopolymerization of acrylate-based mesogens to fabricate different swimming microrobots [4]. The primary concept to achieve nonreciprocal motions involved inducing a traveling wave deformation in the microrobotic bodies by actuating them with a dynamic light pattern. The LCN was doped with an azodye, which could heat the material up to 100°C depending on the power density [86]. Synchronized movement can be used as propulsion mechanism by employing diffused UV or green light to generate a photomechanical response in microstructures made of azobenzene-containing LCE. This reduces the need of high power lasers to drive biomimetic swimmer made from such materials as demonstrated by Sartori et al. [87]. Selective irradiation of specific parts of the LCN caused asymmetric deformation. By scanning the projected light, the traveling deformation enabled the microrobots to swim. An LCN cylinder prepared by manual fiber drawing, and a microdisk fabricated through photolithography [88]. The microdisk is capable of swimming along various 2D pathways, and multiple swimmers can be controlled simultaneously using a simple optical setup that includes a spatial light modulator (SLM).

Direct laser writing (DLW) has been effectively employed to develop light-driven microrobots made from liquid crystal networks (LCNs) that function in air, including walking robots [89] and microgrippers [90]. The walking microrobot features an LCN body with four rigid, conical legs designed to minimize surface interactions and decrease adhesion forces. When exposed to intermittent light, the body's cyclic

contractions enable the microrobot to move incrementally across a glass surface [89]. For the microgripper, a star-shaped LCN structure with diverse liquid crystal (LC) alignments was created. Upon activation, the segments bend towards the center, emulating the gripping motion of a human hand, which allows for the manipulation of microblocks composed of various materials [90].

These instances demonstrate the potential of integrating materials with distinct properties and utilizing multiple LC alignments to achieve asymmetric deformation within a single platform via multistep writing processes. The speed and degree of contraction under light or heat can be tailored through various methods, such as altering the crosslinking agent in the monomer mixture [91], increasing the flexible spacer length of the mesogens to boost material flexibility [92], or adjusting DLW fabrication parameters to obtain different polymerization levels [93].

1.4 Bio-hybrid microrobotics

Biohybrid robotics represents an approach that integrates synthetic fabricated structures with living biological systems. This strategy leverages the characteristics of biological cells and tissues, which have been refined through years of natural evolution. A primary focus in this field is actuation, which serves as a key motivator for developing biohybrid robots. Biohybrid robots hold the promise of delivering unparalleled performance at the macroscale and facilitating the creation of self-powered microrobots [94].

Tissue engineering based microbots

Cardiomyocytes are muscle cells of the heart that can form coordinated contraction when grown in contact with each other. This characteristic makes them an excellent candidate for biohybrid actuators, particularly in tissue engineering applications. Leveraging the inherent properties of cardiomyocytes, these actuators can create powerful, scalable, and versatile biohybrid robotic systems.

Cardiomyocytes from neonatal rat or mouse hearts are frequently used due to their developmental plasticity, allowing them to integrate with artificial substrates and form functional devices. Xi et al. created a walking biohybrid microrobot by seeding cardiomyocytes on a silicon-based micromechanical structure, achieving a speed of 38 $\mu m/s$ (see figure 1.7 a)[95]. Tanaka et al. developed a micropump powered by cardiomyocytes, with a flow rate of 2 nl/min, demonstrating the flexibility and scalability of cardiomyocyte-based systems [7].

A swimming crab-like robot, in a 2007 study, using cardiomyocytes and polydimethylsiloxane (PDMS), reached an average velocity of 100 $\mu m/s$ [96]. Feinberg et al. introduced biohybrid microrobots with patterned monolayers of cardiomyocytes on PDMS, capable of gripping, pumping, walking, and swimming [97]. Chan et al. utilized 3D printing to create miniaturized biobots from hydrogels and cardiomyocytes, achieving a walking speed of $\sim 236 \mu m/s$ [98]. Williams et al. developed PDMS filaments with cardiomyocytes, mimicking flagella behavior and achieving propulsion at 81 $\mu m/s$ [99].

In 2016, Park et al. developed a biohybrid device inspired by a ray, using a four-layer elastomeric/metal structure patterned with cardiomyocytes. These

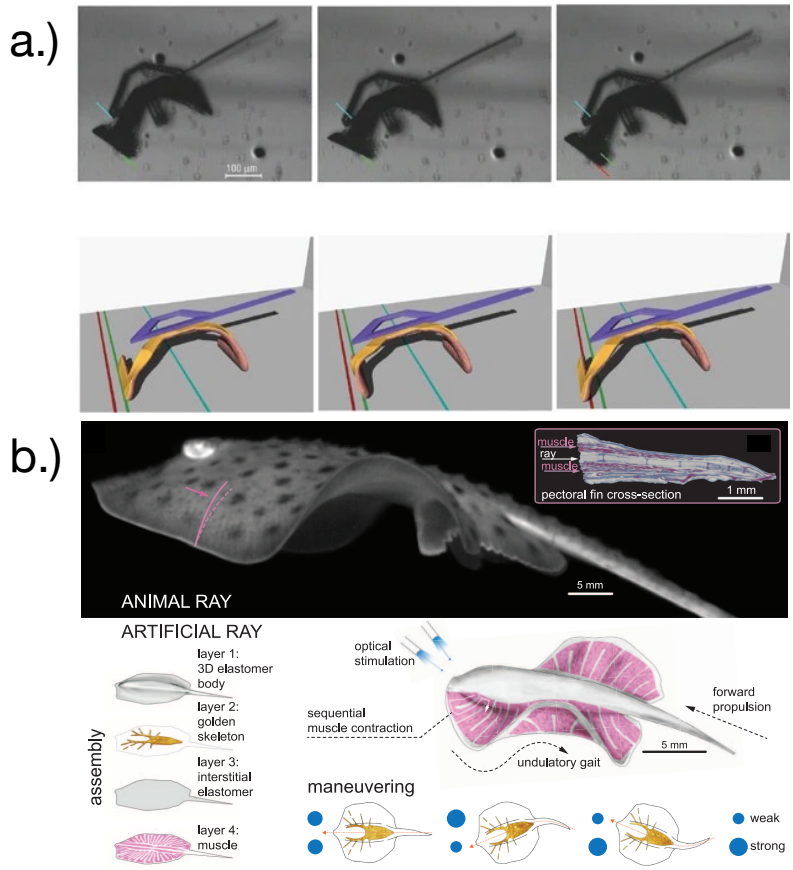

Figure 1.7. Biohybrid microbot utilizing cardiomyocytes for actuation (a) Silicon based micro mechanical walking microbot seeded with cardiomyocytes, capable of assessing the mechanical characteristics of muscles in their natural environment and propelled by the coordinated contraction of muscle bundles. [95]. (b) Light controllable stingray capable of swimming upto 1.5 mm/s. The cardiomyocytes were genetically modified to respond to light signals, causing the robot to move through water in the direction of the light source. [100].

cardiac cells were genetically modified to express channelrhodopsin-2 (ChR2), a light-sensitive ion channel, making them responsive to blue light at approximately 10 mW. The cardiac syncytia on the construct could propel the device forward through undulatory fin movements. The device's speed and direction were controlled by adjusting the frequency of light stimuli and synchronously or asynchronously triggering right and left serpentine circuits embedded in the device. This allowed the ray-inspired biohybrid robot to navigate curved paths by alternating between forward motion and turning maneuvers. The robot achieved an average speed of 1.5 mm/s and could travel continuously for distances up to 250 mm, which is 15 times its body length. The system had a lifespan of six days, maintaining above 80 % of its initial speed throughout this period (see figure 1.7 b)[100].

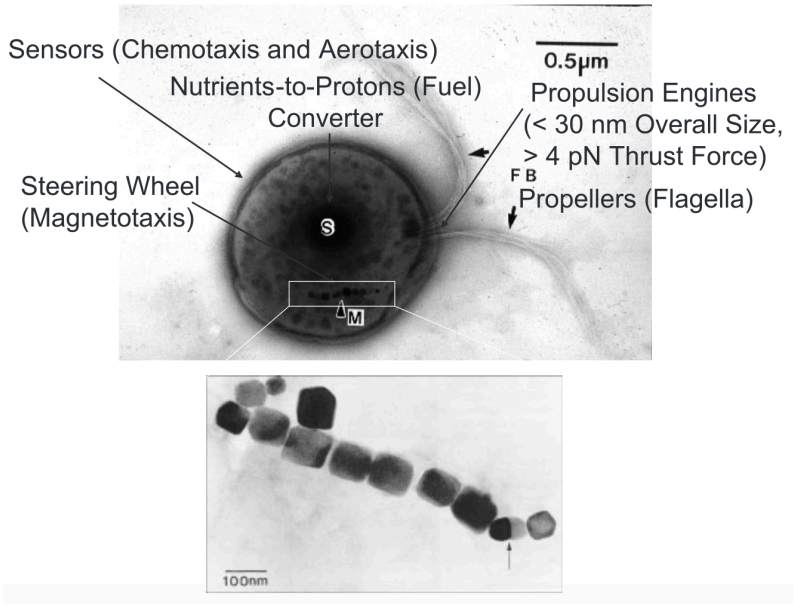

Figure 1.8. Magnetotactic bacterial microbot for medical application Computer-controllable bio-actuator with its flagella bundles (FB) for propulsion and its chain of magnetosomes that allow steering control through magnetotaxis. The two flagella bundles used for propulsion and the chain of magnetosomes used for directional control are visible in the image. [101]

Bacterial cell based biohybrid systems

Microbots based on bacteria and other motile cells are notable for their small dimensions, typically ranging from 1 to 10 μm. This size compatibility allows them to navigate through human capillary networks and interstitial spaces, making them ideal candidates for applications such as drug delivery systems within the vascular network [101, 102]. Their key characteristics can be Chemotaxis (movement toward chemical gradients), Magnetotaxis (movement in response to magnetic fields), Galvanotaxis (movement in response to electric fields), Phototaxis (movement toward light), Thermotaxis (movement in response to temperature gradients), Aerotaxis (movement toward areas with specific oxygen concentrations) (see figure 1.8)[103].

These affinity responses enable the microrobots to autonomously navigate towards environmental stimuli, enhancing their functionality for targeted applications. While this variety of behaviors doesn't allow for complete external control, it enables the robots to sense their environment and move autonomously toward pre-programmed stimuli. The small size and autonomous navigation capabilities of these biohybrid actuators make them particularly suited for precise medical applications, such as targeted drug delivery. Their ability to navigate the complex environments within the human body, responding to specific stimuli, provides significant advantages for minimally invasive treatments and diagnostics [104].

Park and colleagues developed a bacteriobot using attenuated *Salmonella typhimurium* attached to a polystyrene microbead [105]. This microrobot was endowed with chemotactic abilities to navigate towards tumor spheroids. The bacteriobot showcased its theranostic capabilities by effectively targeting solid tumors in mice,

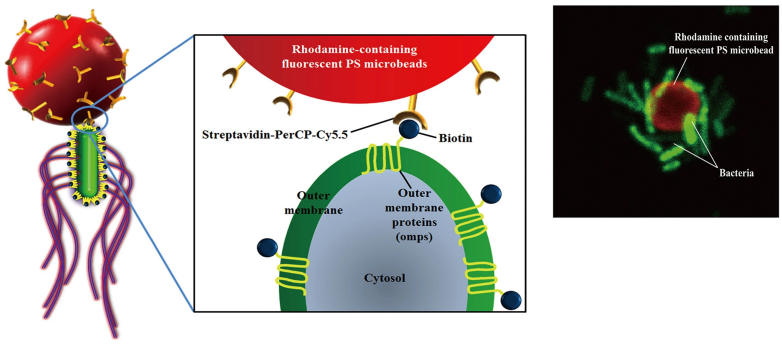

Figure 1.9. Biohybrid bacterial microbot for tumor targeting Bacteriobot using Salmonella bacterium attached to polystyrene bead for tumor targeting. The bacteriobots demonstrated a higher migration velocity towards tumor cell lysates or spheroids compared to normal cells. In the CT-26 tumor mouse model, the bacteriobots alone were injected, and a Cy5.5 signal was detected from the mouse model's tumor site. [105]

highlighting its potential for cancer treatment (see figure 1.9). While, Singh et al in another study, *E. coli* was combined with a soft double-micelle microemulsion to facilitate the active transport and delivery of various cargos, including imaging agents, genes, and drugs [106]. his biohybrid system was tested *in vitro* on cultured cells, demonstrating its capability to deliver therapeutic and diagnostic materials to specific cellular targets. research has concentrated on modeling and optimizing the motion of bacteria-based microswimmers, particularly when carrying cargo and navigating towards chemotactic stimuli. These studies aim to enhance the efficiency and effectiveness of biohybrid microrobots in medical applications [107].

The potential of bacterial strains as tumor-targeting vectors has been extensively highlighted. However, nonrobotic strategies, while improving drug targeting, often fall short of optimal efficacy. These approaches typically involve systemic drug delivery, which can raise issues of systemic toxicity and reduce the therapeutic index [108, 109].

Some microswimmer exhibit chemotactic ability towards tumor tissues and can be steered remotely using external magnetic fields, enhancing targeting precision and reducing systemic exposure. Park et al. developed a microswimmer for targeted active drug delivery. This system involved attaching *E. coli* to the surface of drug-loaded polyelectrolyte multilayer microparticles embedded with magnetic nanoparticles [110].

Felfoul et al. described a biohybrid robot using the magnetotactic bacterium *Magnetococcus marinus*, which was loaded with liposomes containing an anticancer drug. This system combined magnetotaxis and aerotaxis for dual navigation. The aerotaxis-based self-steering, along with remote magnetic steering, allowed efficient targeting of colorectal xenografts in mice, penetrating even the hypoxic regions of tumors [111].

Both of the above described systems have limitations. While the cardiomyocytes with optogenetic control effectively combine the strong contraction forces control [112], the current system only allows modulation of speed and direction but cannot fully switch the robot's activity on and off. On the other hand, the bacteria based systems lacks the actuation flexibility needed for creating scalable robots

This is why the focus, this thesis is exactly a combination of optogenetic control over bacterial species which provide a platform for biohybrid microbots. By using bacterial cells, our method allows for the creation of biohybrid robots that can be scaled up or down according to specific needs and supports the development of actuation suitable for a wide range of application.

1.5 Research questions

Microrobots have been suggested for a wide range of applications, including biomedical therapy and environmental pollution cleanup. However, even basic task of manipulation of biological cells is extremely tough as precise and energy efficient control of multiple microbots simultaneously remains challenging.

However, where our research sets us apart in the development of micro-robots is the use of bacteria for propulsion. Previous works have shown that the biological circuitry of an *E. coli* cell can be hacked to allow for control over its swimming speed [113]. This has led to extraction of mechanical work in a bath of swimming bacteria [114]. Furthermore, 2D free floating microfabricated structures have be shown to utilize bacterial propulsion and light actuation to limited directional control [115, 116].

Given this foundation, we can move towards developing 3D microfabricated, self-assembled systems with consistent behavior, allowing them to be independently controlled to perform complex tasks. The specific questions addressed in this thesis are:

1. How can we design a 3D microbot to incorporate swimming light driven bacteria optimal propulsion?
2. What can be the control and driving strategy of such a microbot ?
3. What application can we exploit the microbot for?

The first question is explored in Chapter 2, while the second. Finally, the last question is closely examined in Chapter 4.

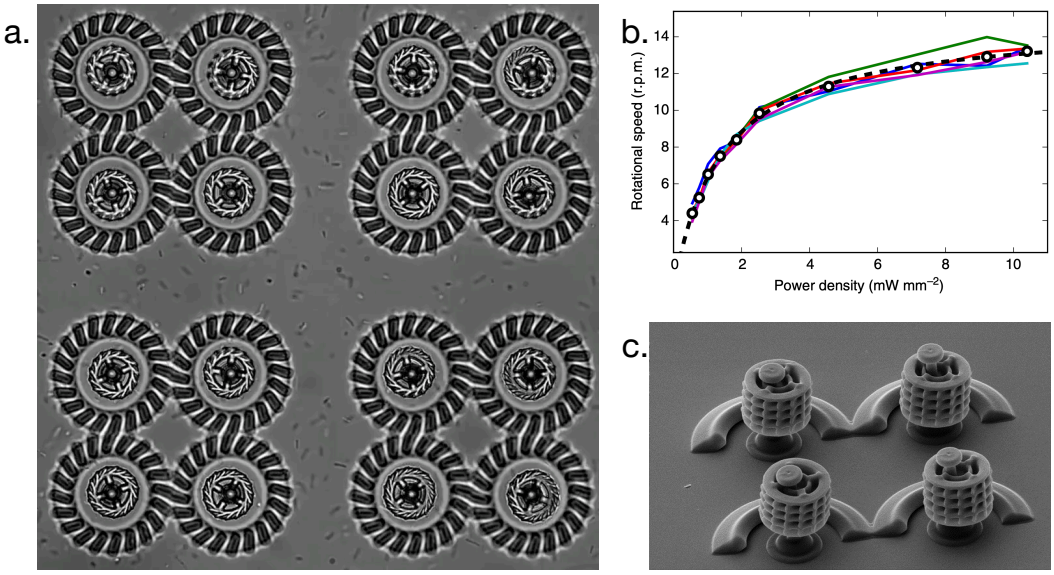

Figure 1.10. Light controlled 3D micromotors powered by bacteria. (a) Rotor array used for the rotational dynamics characterization. (b) Rotational speed of 5 micromotors obtained by changing the illumination power (c) SEM image of the 3D fabricated micromotor array (Figures taken form [114])

Chapter 2

Development and optimization light driven bio-hybrid microbots

Studies regarding drag coefficient measurement and connector length shown in this chapter have been published in the supplementary section of 'Light Driven Biohybrid Microbot'. [117].

Active particles, bacteria alike, are capable of generating mechanical forces [118]. Utilizing this idea, an approach to creating bio-hybrid micromotors that are propelled by genetically engineered *E. coli* bacteria and controlled by light was developed [114]. This included the use of 3D microfabricated micromotors that were fixed and had chambers that could trap moving genetically engineered *E. coli* bacteria. The speed of these bacteria and thus the rotational speed of the micromotors could be controlled by adjusting the green light intensity shown on the sample.

Inspired by this line of research, we developed self-propelled microbots capable of independent steering along two-dimensional trajectories on solid substrates, such as the bottom glass of a microfluidic chip. We employed two-photon polymerization to fabricate the microbot chassis from SU-8 photoresist. The structures are fabricated in arrays on cover glasses pre-coated with a sacrificial dextran layer.

We utilized a smooth swimming strain of *E. coli* bacteria expressing the light-driven proton pump proteorhodopsin. In the absence of oxygen, aerobic respiration is inhibited, allowing proteorhodopsin to control the proton motive force driving the flagellar motors. Consequently, the bacteria's speed is determined by the local intensity of green light. Upon introducing the aqueous solution containing the bacteria into the sample contain microbots, the dextran layer dissolves, releasing the structures from the cover glass.

Although this explanation looks simple, it required months of careful optimization on every level of development. In this chapter, we take a look at the main power and actuation source for these microbots, i.e. the genetically modified bacteria and the optimizations required for the microbot chassis to accommodate them. In the last two sections, we investigate the effects of the design consideration of the microbot which influences its dynamics later on.

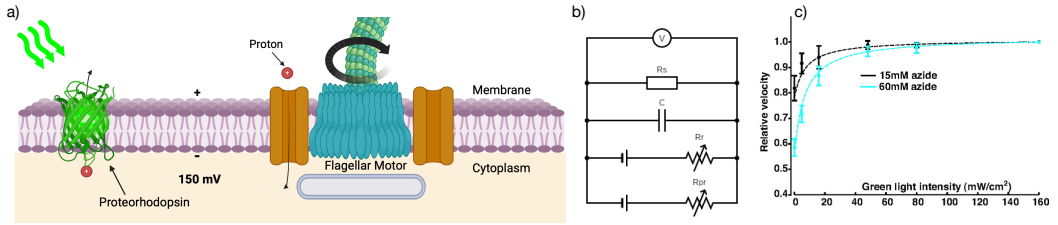

Figure 2.1. Scematic of working of proteorhodopsin. a) Proton transfer and proteorhodopsin working principle. b) Model including sources of PMF (respiration and proteorhodopsin), R_s being sinks (such as the flagellar motor and ATP synthase), and the membrane capacitance. The variable resistors R_{res} and R_{PR} model the effect of azide and light on proton extrusion by respiration and PR, respectively. The voltmeter (top-most circuit element) measures the potential difference across the membrane (equivalent to the PMF). c) The rotation speed of PR+ cells depends on the intensity of green illumination. Individual PR+ spinner cells were exposed to six intensities of green light. The mean angular velocity at each intensity is plotted (n = 5–6 cells for each intensity), normalized by the velocity at maximum illumination. [122]

2.1 Proteorhodopsin: The bacterial light switch

As discussed in section1.2, *E. coli* bacteria are able to move due to flagellar rotation, by the virtue of proton transfer across cell membrane.

Through synthetic biology, we can enhance the light responsiveness of *E. coli* by introducing genes encoding photoreceptors from other organisms. This genetic engineering enables *E. coli* to detect light better, expanding its behavioral to include responses typically found in other species [119]. Photokinesis refers to the regulation of a cell's speed in response to light stimuli, which involves altering the energy supply to the flagellar motor. This phenomenon allows bacteria to modulate their movement based on the presence and intensity of light[120].

The discovery of proteorhodopsin (PR) in 2000, a light-powered proton pump, revolutionized the understanding of bacterial phototrophy[121]. In 2007, Walter et al. utilized PR-expressing (PR+) *E. coli* cells to demonstrate that light can power the flagellar motor [122]. They showed that the speed of the flagellar motor in single, smooth-swimming PR+ cells tethered on a glass slide could be controlled using green light (532 nm) in an environment where the proton motive force (PMF) could not be maintained by oxidative phosphorylation (see figure 2.1 a).

Here, the speed of flagellar motor is directly proportional to the proton motive force (PMF). In the presence of light, the outer proton flux created by PR can power the rotation of flagellum. As protons re-enter the cell through motor, they generate the necessary torque to drive flagellar movement. This process underscores the potential of light as a tool for controlling bacterial motility.

Walter et al. proposed an analogous electrical circuit to represent the functional relationship between proton motive force (PMF), respiration, and proteorhodopsin (PR) in a membrane with proton sinks [122]. (see figure 2.1).

In this model, the maximum speed of the bacterial flagellar motor, which is proportional to the PMF, is determined solely by the PMF generated by PR. This

relationship is described by the following equation:

$$\mathrm{PMF}_{PR} = \frac{V_{PR} R_{sink}}{R_{sink} + R_{PR}(I)} \tag{2.1}$$

where, V_{PR} is the the maximum potential PR can generate by using free energy from photon absorption, R_{sink} includes sinks (such as the flagellar motor and ATP synthase), and the membrane capacitance and $R_{PR}(I)$ is the resistance dependent on light intensity I, modeled by Michaelis-Menten kinetics:

$$\mathrm{R}_{PR}(I) = \left(\frac{V_{max}}{K_m + I} \right)^{-1} \tag{2.2}$$

Here V_{max} represents the maximum effect of PR when saturated and K_m is Michaelis constant.

The dynamics of system when light intensity is reduced are described by the following equation:

$$\mathrm{PMF}_{PR}(I, t) = V_0 exp\left(-\frac{t}{\tau_{off}} \right) \tag{2.3}$$

where, V_0 is the initial PMF at $t = 0$, and $\tau_{off} = R_{eff} C$. The effective decay resistance $R_{eff}$is the parallel combination of $R_{PR}(I)$ and R_{sink}. Thus, the PMF decays exponentially to a steady state with a time constant determined by the new level of light intensity I.

To explore the control of bacterial motility using light, we engineered the *E. coli* strain AUYG, building on the previously utilized strain AB1557 $\Delta unc :: cmR$ [123]. The construction of this new strain involved several genetic modifications and transformations to ensure precise control over bacterial swimming behavior.

Using lambda red recombination with the recombination plasmid pKD46, we targeted and deleted the cheY gene, which is responsible for the tumbling behavior in bacteria [124]. This gene deletion was achieved by replacing cheY with a kanamycin resistance (KnR) cassette, flanked by 50 bp homology arms. These homology arms were amplified using the template pKD4 and the following primers:

Forward primer: GCAAAAATTAGTGCCGGACAGGCGATACGTATTTAAAT-CAGGAGTGTGAAGTGTAGGCTGGAGCTGCTTC

Reverse primer: CTGAATGCTCGTCAGCAGGTTTGATTGATGGTTGCATC-ATAGTCGCATCCATGGGAATTAGCCATGGTCC

PCR reactions confirmed the successful deletion of the cheY gene, resulting in the strain AB1557 $\Delta unc :: cmR \Delta cheY :: knR$. This new strain lacked the gene necessary for the tumbling behavior, ensuring it exhibited smooth swimming.

Next, we transformed the modified strain with the plasmid pBAD-His C, which encodes the SAR86 γ-proteobacterial proteorhodopsin (PR). The introduction of this plasmid allowed the bacteria to express PR, a light-driven proton pump, enabling control of bacterial speed using light. The resulting strain, AUYG, exhibited smooth swimming behavior with the ability to modulate its speed in response to light intensity.

The newly constructed strain AUYG was similar to the previously described strain AD57, used in earlier studies [125]. However, the integration of PR and the

deletion of cheY gene provided a better capability to control motility with light, offering a tool for developing bio-hybrid robots.

A we calibrated the bacterial motility for different light intensity by doing differential dynamic microscopy (DDM). A detailed discussion, along with analysis, for this is presented in chapter 6 section 6.2.

2.2 Chassis design optimization

Utilizing bacterial propulsion for microstructures introduces a distinct array of challenges and potential benefits. Here, we examine the design journey of microbots powered by bacteria, focusing on the intricacies of microstructure design, the integration of bacteria, modifications and the impact of surface forces on movement. It traces the path from initial concept to a working prototype, emphasizing the iterative nature of solving the various challenges encountered.

The first design iteration for our microbot featured a straightforward model comprising two microfabricated chambers connected by a narrow bridge. The primary idea was to capture bacteria within each chamber and utilize their propulsion to move the entire structure. The fabrication of all microstructures were done on our custom built two-photon polymerization setup mentioned in detail in Part II of this thesis, chapter 5 section 5.

Wedges microbots

Among the various propeller designs considered, wedge-shaped propellers joined by a connector proved to be the most straightforward to conceptualize. This was based on the concept of swim pressure of active particles [126]. The swim pressure measures the average force that microswimmers exert on confining walls in a nonequilibrium state [127].

The microbot chambers were designed as triangular wedges, with the wedge angle varied between 15° and 90°. This variation aimed to identify a structure that could best accommodate the bacteria while maximizing propulsion speed. The catching efficiency can be regulated by adjusting the apex angle of the trap, which determines the wedge's sharpness [128]. By systematically adjusting the wedge angles and testing each configuration, we sought to determine the optimal design that balanced bacterial retention and effective propulsion (see figure 2.2 a) .

Initially the length of wedges was also varied from 5 μm to 20 μm. However, it was quickly realized that the longer side lengths are useless as the bacteria that contribute to the propulsion stay only in the region closer to the wedge. This is why the side length was kept at 10 μm. Another design for the wedges consisted of two U-shaped propeller joined by a connector.

For all these designs, the microbot were able to achieve propulsion with a low persistence length and high diffusive behavior. This was due to the bacteria escaping the microstructure. To remedy this issue, a small area between the wedge was fabricated as a roof and a floor, creating a chamber for the bacteria to accumulate and stop from escaping.

This strategy proved to be counterproductive. The flagellar bundle was not able to exert enough hydrodynamic drag onto the surrounding fluid to give a decent

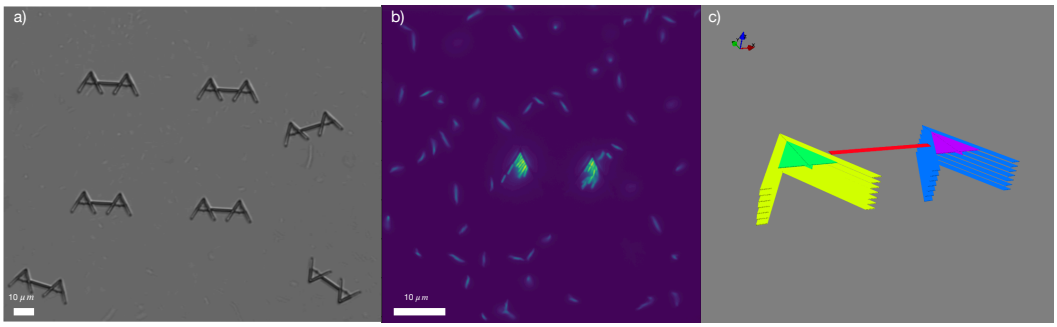

Figure 2.2. Snapshots from the experiment with wedges microbot (a) snapshot of a wedge microbot during design optimization tests. Image taken under bright-field using a 10X objective. (b) Image of the same wedge microbot using fluorescent bacteria to see how the chamber are filled. It can be clearly seen that the bacteria do not align symmetrically in both the chambers thus exerting unbalanced forces. (c) Show the 3D rendering of the microbot done during two photon fabrication process

propulsive force. The floor, too caused the structure to have more surface drag. Further investigations using fluorescent bacteria showed an imbalance in the filling of wedge chambers. The bacteria had ordered themselves more towards one of the side walls then the other. This creates an unbalance in the forces exerted by the bacteria. The combination of these two factors prevented to these first iteration of microbots to from having any effective motion.

Mother-machine microbots

The mother machine, introduced by Wang and his colleagues in 2010, is a widely-used microfluidic platform designed for long-term, high-throughput imaging of individual cells [129]. It has become the standard for extended imaging of bacteria like *E. coli* and *Bacillus subtilis* [9]. In this device, thousands of single cells are confined within one-ended growth channels that lead into a central trench.

We used this idea and modified it to capture only a few *E. coli* cells to provide propulsion. This design allows for at least one cell to remain in each chamber. The number of chambers was varied between 3 and 5 as well as the length of the chambers.

When the chambers is the closed from both the lateral sides and also from the top and bottom sides the bacterial flagella is not able to exert any force of the surrounding fluid. This would result in no propulsion from the inner most bacteria trapped in the the chamber. Only the last bacteria in the chamber with partial flagella outside would provide for any real propulsion. To avoid this the bottom part in the chambers was left open.

These designs initially showed great promise. However, microstructures encompassing bacteria, have can sometimes flip due to a variety of factors and in that case the bacteria in the mother-machine microbot would simple empty out with no way to entrap the bacteria again. Due to these issues the development of in this direction was halted.

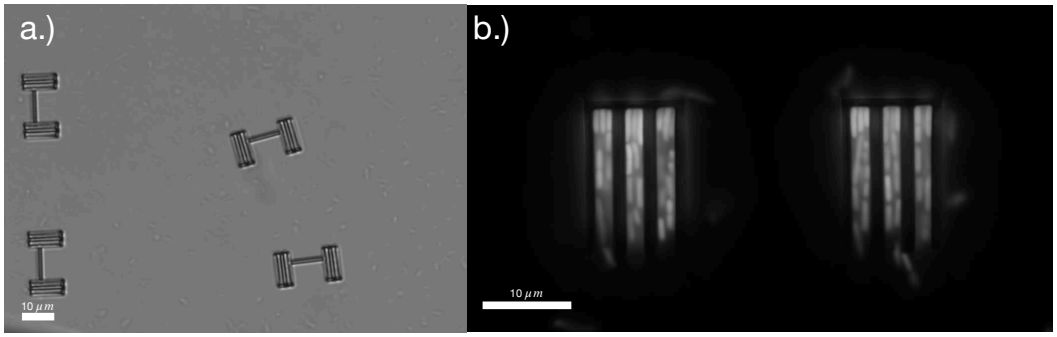

Figure 2.3. Snapshots from the experiment with mother-machine microbot (a) Snapshot of mother-machine microbot during design optimization tests. Image taken under bright-field using a 10X objective. (b) Image of the mother-machine microbot using fluorescent bacteria investigate the filling of chambers using a 100x objective.

2.3 Catamaran design

To better design our microbots, we came to understand that to maximum propulsion from the bacteria is by entrapment of the cell body while most of the flagella has to remain outside the confinement. There also has to be no obstruction to the movement of the flagellar bundle itself.

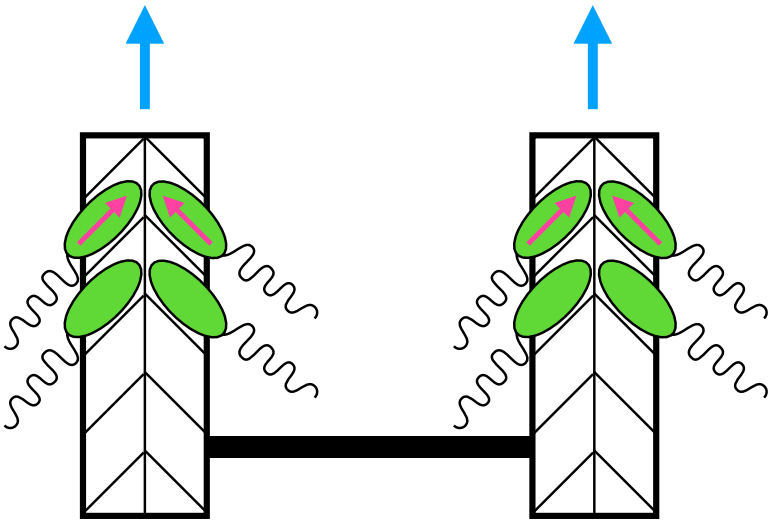

Figure 2.4. Schematic showing the alignment of bacteria in microbot. The microbot chambers are tilted at 45°. Pink vector shows the direction in which the bacteria apply the force while the blue vector shows the direction of net force in the propeller.

Each microbot consists of two identical units, referred to as propellers or engines, which are connected by a 20 μm-long rod. The final optimized dimensions of each unit are 18.6 μm in length, 5.0 μm in width, and 6.1 μm in height, with each unit comprising eight microchambers. These microchambers feature openings measuring 2.8 μm by 3.5 μm (width by height) to accommodate a single cell body while

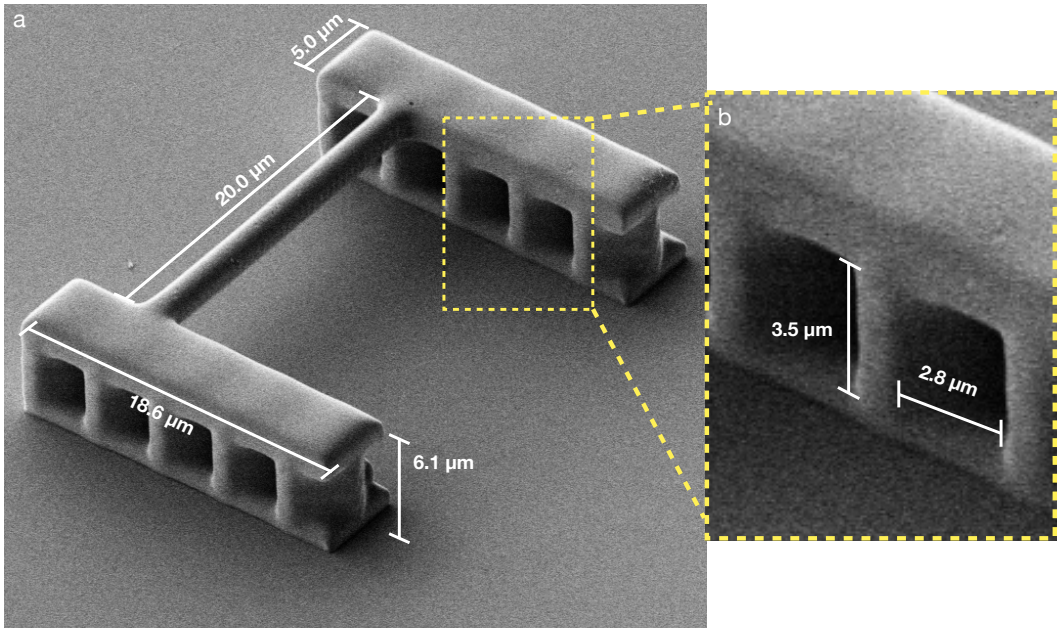

Figure 2.5. SEM image a single microbot a) SEM image with all the dimensions noted. b) Zoomed in view of the chambers that incorporate the bacteria.

leaving the flagellar bundle exposed for optimal propulsion. The microchambers are symmetrically arranged along the engine's major axis and tilted at a 45°angle to maximize the total force exerted on the engine. This was done as it maximizes the translational velocity and the number of bacteria to be assembled in the microbot. Because each cell is self-propelled by a constant force, a pair symmetrically located and represented by pink vectors on Figure 2.4, then the net propulsion will be pointing in the forward direction of the propeller represented by blue vector.

Based on measurements in figure 2.5, we estimate a total volume of 103 μm^3, resulting in a buoyant mass of 0.2 ng (given the SU-8 density of 1.2 g/cm^3) and a minimal sedimentation length of 2 nm, ensuring the empty chassis remains fully sedimented on the bottom cover glass.

The self-assembly of bacteria into the microchambers is remarkably efficient, typically completing within minutes. This was see during the filling of chambers using fluorescent bacteria (see figure 2.7).This efficiency is comparable to that observed in more complex three-dimensional structures. In our case, the process is further facilitated by the high concentration of bacteria on the cover glass plane due to hydrodynamic entrapment. Additionally, the tendency of bacteria to swim with a propulsion direction inclined toward the interior of confining walls likely aids in their entry into the microchambers when they slide along the side walls. Once loaded with bacteria, the microbots self-propel at an average speed of 2 μm/s, tracing circular paths confined to the glass surface. Similar to freely swimming bacteria, these microbots are force-free and generate flagellar flows. When these flows reflect off the no-slip boundary at the bottom, they create a hydrodynamic attraction that stabilizes the microbot within the two-dimensional plane.

2.3.1 Optimization of two photon fabrication parameters and bacterial chamber calibration

Achieving the correct chamber size for the microbot was a critical aspect of my research. The process involved multiple adjustment of several microfabrication parameters to ensure the chambers met the specific requirements for effective microbot performance and capture of bacterial cell.

Sr.	Power (in mW)	Speed (in $\mu m/sec$)	X-Y res (in nm)	Z res (in nm)	Fabrication Time (in Mins)	Height (in μm)
1	8	100	196.17	952.31	1.16	2.87
2	8	80	249.01	1083.91	1.225	4.42
3	8	50	334.00	1359.13	1.436	5.1
4	6	50	175.58	812.07	3.11	5.46
5	6	40	234.90	973.93	2.49	4.34
6	4	20	133.14	688.10	10.08	4.88
7	4	10	302.33	1119.98	8.06	5.37
8	3	10	114.35	447.34	26.4	5.42

Table 2.1. Table specifying the variation done for optimizing microbot fabrication parameters

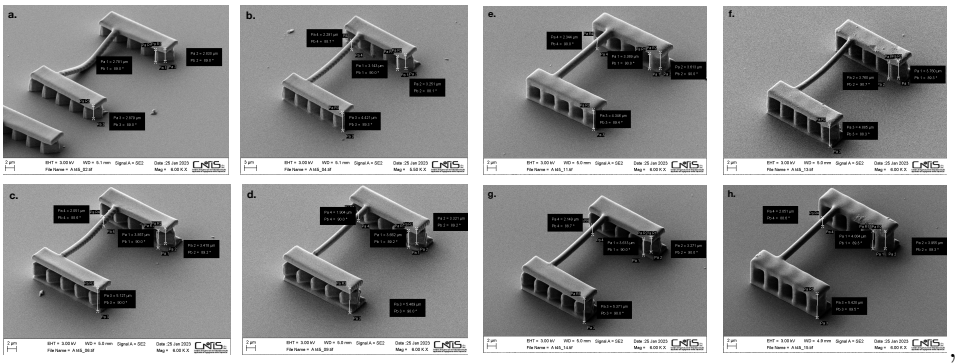

Figure 2.6. SEM images microbot for investigating optimal fabrication parameters (a) Laser Power = 8 mW, speed = 100μm/sec. The structure is compromised structural integrity, with deformed connector rod and no floor. (b) Laser Power = 8 mW, speed = 80μm/sec. The floor has not been well fabricated, the connector has a bend. (c) Laser Power = 8 mW, speed = 50μm/sec. The connector has a bend with the cross-linking at the edges has not occurred. (d) Laser Power = 6 mW, speed = 50μm/sec. same as (c) with the connector having a bend with the cross-linking at edges has not occurred. (e) Laser Power = 6 mW, speed = 40μm/sec. This Microbot has good structural integrity with high resolution and no deformity. (f) Laser Power = 4 mW, speed = 20μm/sec. Slight bending of the connector rod. (g) Laser Power = 4 mW, speed = 10μm/sec. cross-linking at the edges has not occurred. (h) Laser Power = 3 mW, speed = 10μm/sec. This Microbot has the best structural integrity with high resolution and no deformity, however it also has the largest fabrication time

Fine-tuning the fabrication speed and laser intensity during the TPP process was crucial to accurately define the chamber dimensions. Overexposure or underexposure

could lead to incorrect chamber sizes or incomplete pattern transfer. Calibration tests were performed to find the optimal exposure parameters, balancing between adequate cross-linking of the resist and maintaining sharp feature edges.

Therefore, a study of variation in fabrication parameter and its effects o the microbot was carried out. The table 2.1 mentions all the variation done and figure 2.6 show the SEM image analysis carried out on the structures. Here, it can be clearly seen that at higher scan speed and laser power, the structures tend to be deformed. This is due to underexposure and inadequate cross-linking of the photo-resist. On other hand, at lower scan speed and laser power, even if the structure resolution is excellent, the fabrication time require per structure is very high.

To strike a better balance the microstructure resolution and fabrication time, we maintained the scanning speed and laser power at 40 μm/sec and 6mW, respectively. This gave us a fabrication time of 4.34 mins per structure.

The microbots are fabricated in a 3x3 lattice, maintaining a distance of 30 μm between them. After two-photon exposure, the sample under went post-exposure baking at 95°C for 8 mins. The polymerized microstructures are developed using standard SU-8 developer solution (KAYAKU Advanced Materials) for 7 minutes and then dried with nitrogen. These steps are discussed in detail in the Methodologies Part, section 5.2 of this thesis.

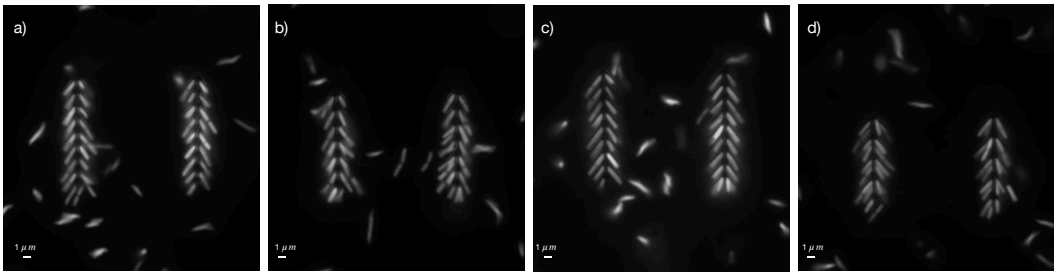

Figure 2.7. Optimization of bacterial chamber size for *E. coli* cells. By conducting a variation in chamber height, width and length Images are taken using fluorescent microscopy setup. The images show variation of number of chambers and cell width. (a) number of chambers equal to 9, (b) Number of chamber equal to 6, (c) Width of chamber equal to 2.5 μm, (c) Width of chamber equal to 3 μm

Once then right fabrication parameters were recognized, a secondary optimization was done for the bacterial chamber size. This involved the use of fluorescent bacteria for imaging the right fit of the *E. coli* cells. A variation in the height and width of the chamber size was carried out to find at which parameter can we capture and hold a single *E. coli* cell per chamber (see figure 2.7).

2.3.2 Measurement of drag coefficients of empty microbot

The translational and rotational drag coefficients of the empty microbot can be measured by tracking its Brownian motion in the absence of bacteria and then using the Einstein-Smoluchowski equation. Generally, the diffusion coefficient D of a particle subjected to Brownian forces can be related to its drag coefficient Γ via the Einstein-Smoluchowski equation:

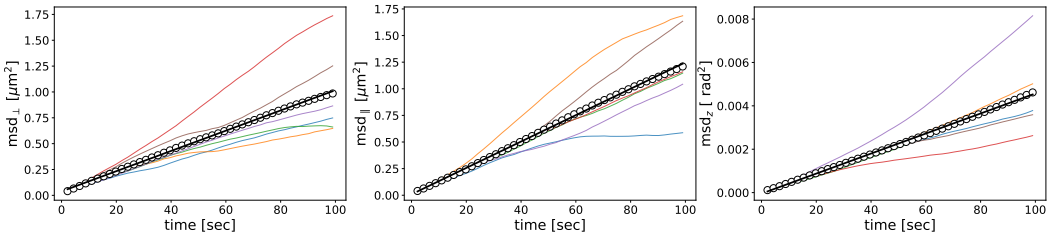

Figure 2.8. Mean square displacements of microbots in motility buffer and in the absence of bacteria. a) msd along the axis of motion ($msd_{\parallel}$), b) msd along the axis perpendicular to motion ($msd_{\perp}$), c) rotational msd. For each graph, we report the msd for 6 microbots as colored lines, the average msd as black empty circles, and the linear fit as a black solid line. The coefficients of the linear fit y=mt+c are used to extract the diffusion coefficient $D = m/2$.

$$D = K_b T/\Gamma \tag{2.4}$$

where D is the diffusion coefficient, K_b is the Boltzmann constant and T is the temperature of the fluid.

We conducted an experiment to monitor the dynamics of six microbots in a motility buffer, devoid of bacteria, over a period of 20 minutes. During this time, we tracked their projected mean square displacement (MSD) in directions both parallel and perpendicular to the main axis of the microbot. The results (see figure 2.8 a and b) allowed us to compute the parallel MSD and perpendicular MSD displacements.

From the averaged MSD data across all six microbots, we determined the diffusion coefficients:

$$D_{\parallel} = 6.20 \pm 0.003 \times 10^{-3} \mu m^2/s$$

and

$$D_{\perp} = 4.90 \pm 0.02 \times 10^{-3} \mu m^2/s$$

Applying the Einstein-Smoluchowski equation, we then calculated the translational drag coefficients:

$$\Gamma_{\parallel} = 0.678 \pm 0.003 pN\mu ms$$

and

$$\Gamma_{\perp} = 0.858 \pm 0.004 pN\mu ms$$

Furthermore, using a similar methodology, we derived the rotational drag coefficient Γ_z from the rotational mean square displacement MSD_z, as depicted in Figure 2.8. The rotational diffusion coefficient was found to be $D_z = 23.1 \pm 0.1 \times 10^{-6} s^{-1}$, leading to a calculated rotational drag coefficient of $\Gamma_z = 181 \pm 1 pNrads$. These measurements of translational and rotational drag coefficients are crucial for understanding the dynamics and optimizing the performance of microbots in fluid environments.

2.4 Effects of connector length on a two propeller design

In designing a microbot where the size of the two individual propulsion units (engines) is fixed, the distance L between these units plays a crucial role in determining the

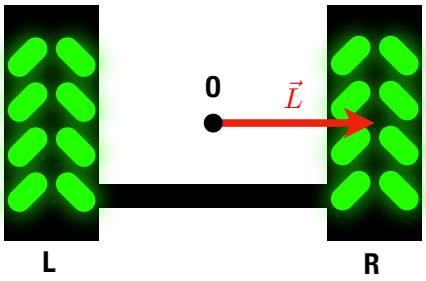

Figure 2.9. General schematic of the microbot with bacteria inside the propellers

maximum steering speed. The applied thrust by the bacteria, and consequently the microbot's torque, depends on this distance. We now look at how to optimize L for achieving the highest steering efficiency by balancing torque and rotational drag.

The torque T generated by the bacteria on the microbot is directly proportional to the distance L between the propulsion units, expressed as $T = f_0 L$. Here, f_0 represents the maximum force exerted by the bacteria on one unit, with the assumption that the force on the other unit is zero. As L increases, so does the torque, facilitating better steering capabilities.

However, increasing L also affects the rotational drag coefficient Γ_z of the microbot. Hence, The rotational drag also increases with L, introducing a counteracting force that hinders rotation. Therefore, to optimize the distance, it is necessary to derive an expression for $\Gamma_z(L)$ and identify the value of L that maximizes the steering speed.

To derive $\Gamma_z(L)$, we consider a microbot moving with a velocity $\vec{U}$ and rotating with an angular velocity $\vec{\Omega}$ around its center O. The velocities of the left and right propulsion units can be decomposed into their translational and rotational components. The rotational drag coefficient Γ_z is a function of L, and it must be expressed in terms of the microbot's physical parameters and the surrounding fluid dynamics.

$$\vec{U}_R = \vec{U} + \vec{\Omega} \times \vec{L}\ , \quad \vec{U}_L = \vec{U} - \vec{\Omega} \times \vec{L} \tag{2.5}$$

and $\vec{L}$ is the vector pointing from O to the center of the right engine. If we project the two velocities on the microbot propulsion axis we obtain:

$$U_R = U + \Omega L\ , \quad U_L = U - \Omega L \tag{2.6}$$

We define $\gamma_\parallel$ and γ_z as the translational (axial) and rotational drag of the isolated left and right units. Then the forces on the two units are:

$$F_R = \gamma_\parallel U_R\ , \quad F_L = \gamma_\parallel U_L \tag{2.7}$$

where we have neglected hydrodynamic interactions between them. The total force on the microbot is

$$F = 2\gamma_\parallel (U_R + U_L) = 2\gamma_\parallel U = \Gamma_\parallel U \tag{2.8}$$

where $\Gamma_{\parallel} = 2\gamma_{\parallel}$ is the total translational drag coefficient of the microbot. On the other hand, the total torque T applied on the microbot is:

$$T = T_R + T_L + F_R L - F_L L = 2\gamma_z \Omega + 2\gamma_{\parallel} \Omega L^2 = \Gamma_z \Omega \tag{2.9}$$

where T_R and T_L are the torque applied on the left and right unit, respectively, while Γ_z is the total rotational drag of the microbot, which we can finally write as:

$$\Gamma_z = 2(\gamma_z + \gamma_{\parallel} L^2) \tag{2.10}$$

We can now express the maximum angular velocity of the microbot ω_0 as a function of L, which is obtained when the force applied by the bacteria is maximum on one unit (f_0) and zero on the other:

$$\omega_0 = f_0 L / \Gamma_z = \frac{f_0 L}{2(\gamma_z + \gamma_{\parallel} L^2)} \tag{2.11}$$

Finally, the optimal distance L^* is the one which maximizes the angular speed, that is, the solution for $\partial\omega_0(L)/\partial L = 0$. Solving the equation, we find that the optimal value of L^* is:

$$L^* = \sqrt{\gamma_z / \gamma_{\parallel}} \tag{2.12}$$

For our choice of the propeller size and L=12.5μm (see figure 2.5), we experimentally found the drag coefficients to be $\Gamma_{\parallel} = 0.678 \pm 0.003$ pN and $\Gamma_z = 181 \pm 1$ pN, from which we can derive the values of $\gamma_{\parallel}$ and γ_z of the single unit:

$$\gamma_z = \frac{1}{2}(\Gamma_z - \Gamma_{\parallel} L^2) \tag{2.13}$$

$$\gamma_{\parallel} = \frac{\Gamma_{\parallel}}{2} \tag{2.14}$$

Using the above expressions and Eq.2.12 we find that the optimal distance for our engine size would be $L^* = \sqrt{\gamma_z/\gamma_{\parallel}} = 10.5$µm which is not far from our design choice of 12.5 μm.

2.5 Conclusion

In this chapter I presented several microbot designs. We found that the best propulsion was obtained with a design incorporating single bacteria. To achieve optimal propulsion, I investigated how, through systematic adjustment of microfabrication parameters, an optimal chamber size could be achieved to incorporate a single bacterium. Optimized chambers provided a suitable design for the bacteria to enter the synthetic chassis and microbots to operate effectively. This was possible due the a fundamental advantage of the Two Photon Polymerization process, where rapid prototyping and precise microfabrication is possible.

We explored the effects of connector length on the microbot and also estimate the drag coefficient.

This has helped to provide a satisfactory answer to the first question asked in the introductory chapter on microbot design. We effectively showcased the integration of phototactic bacteria into a 3D, micro-fabricated artificial chassis.

In next chapter, we take a look at how this bio-hybrid system becomes a light driven microbot, capable of autonomous independent control and what the dynamics of such system are. By engineering the bacteria to actuate via exposure to green light, we can regulate their actions to apply mechanical force on the microbot propellers, thereby moving it and creating a bio-hybrid mechanism.

Chapter 3

Investigation of microbot dynamics

Studies shown in this chapter have been part of our publication; Light Driven Biohybrid Microbot [117].

In addition to propulsion, our microbot also needs a control and guidance mechanism that can autonomously driven the system to complete a set of tasks.

In this chapter, we present a driving strategy for the microbot which takes the advantage of its two propeller design. A feedback algorithm continuously tracks the microbot position and orientation. By projecting dynamically tailored light pattern on the two side of the microbot, we are able to guide iy through a series of checkpoints without any outside interference.

We take a look at the logic behind the development of the algorithm and driving strategy employed to navigate the microbot. We need to understand the forces applied by the bacteria on the microbot and its behavior when the feedback loop is absent. This required a combination of measurements and simulations that are described in the results section. We are also able to estimate the efficiency of this bio-hybrid system.

To begin with, we glance over the DMD microscopy setup used for the microbot experiments and the sample preparation of the microbot detachment. Detailed methodologies about two photon fabrication, sample handling and bacterial cultures are explained later in chapter II.

3.1 Methods

The DMD microscopy setup

Bright-field imaging is performed using a custom inverted optical microscope equipped with a 4X magnification objective (Nikon; NA = 0.13) and a high-sensitivity CMOS camera (Hamamatsu Orca-Flash 2.8). Patterns of green light (520 nm) are generated using a digital micro mirror device (DMD) projector (Texas Instruments DLP Lightcrafter 4500) coupled to the same microscope objective used for imaging through a dichroic mirror [113, 123].

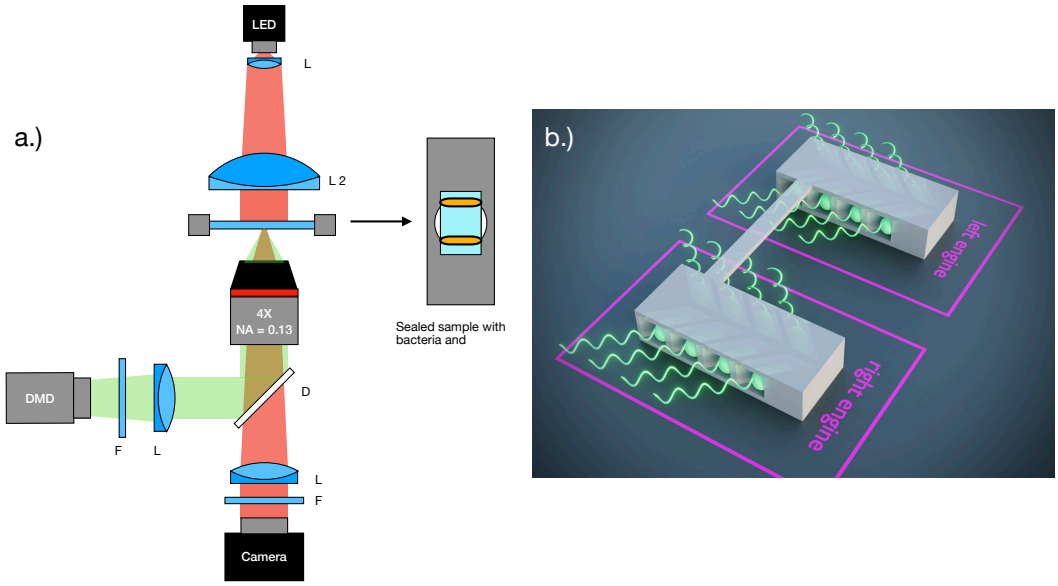

Figure 3.1. Schematic of DMD setup used for the microbot experiment and the microbot (a) Green light from a DMD projector is filtered through a bandpass filter (F1) with a central wavelength of 520 nm, and then directed to the microscope objective via a dichroic mirror (DM). A long-pass filter (F2) is used to block the illumination light from reaching the camera. The bacteria are hermetically sealed using UV glue, between two glass coverslips separated by spacer, which is attached to a metallic sample holder featuring a circular aperture. (b) Schematic of the microbot with bacteria in the propeller chambers.

Microbot- Bacteria sample preparation

The substrate with microbots is covered with a glass coverslip (previously plasma-treated) and hermetically sealed with UV glue (Norland Optical Adhesive NOA81) on opposing sides (see figure 3.2 c). The distance between the coverslip and the glass substrate is maintained by placing a spacer 100 μm thick in the UV glue before sealing the cavity. 40 µL of the prepared bacterial suspension is injected into the glass cavity and is completely sealed on the remaining two sides by the application of Vacuum grease (Sigma-Aldrich). This step is necessary to cut off the system from surrounding oxygen and to avoid the generation of flows in the sample. The microbots detach from the substrate as soon as the bacterial suspension reaches the fabrication site and dissolves the underlying dextran sacrificial layer. The use of ionic species in the bacterial suspension is strictly regulated to avoid any surface charge interactions between the free-floating microbots and the glass surfaces. Bacteria deplete oxygen in around 2-5 mins for OD = 2.0. Once this happens, the bacteria swim only where green light (520 nm) is projected, with their speed increasing as a function intensity of the projected light. [113].

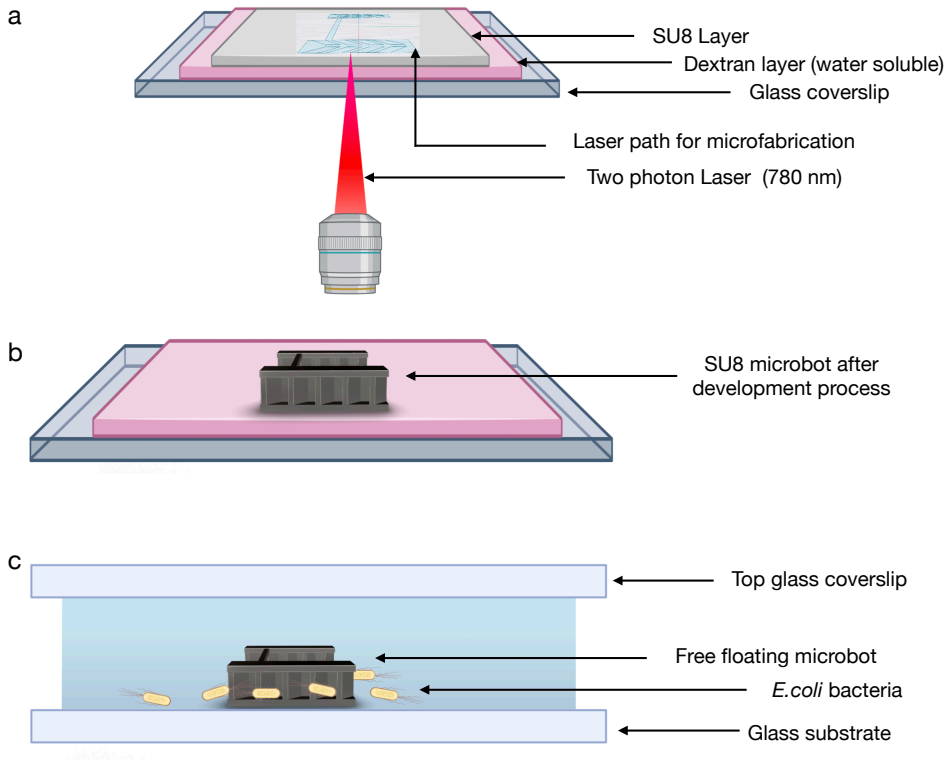

Figure 3.2. Schematic of Microbot sample preparation (a) Two-photon polymerization. (b) SU-8 structures after development. (c) Schematic of the sample chamber.

3.2 Results

3.2.1 Microbots under uniform illumination

Microbots in our study are designed to operate on a two-dimensional plane defined by the glass coverslip surface, allowing translation in this plane and rotation around the normal axis to the surface. We focus on the intricate dynamics of these microbots, looking at their translational and rotational behaviors influenced by bacterial propulsion. We have modeled of their movements, the impact of asymmetries, and the experimental observations that highlight the complexities of their trajectories.

Our microbots can translate along the 2D plane and rotate around the vertical axis passing through their center. The translational drag $\Gamma_{\parallel}$ pertains to the drag experienced by a single structure moving along its axis, while the rotational drag Γ_z relates to the drag around the vertical axis. With a fixed distance $2L = 25\mu m$ between the two engine axes, the microbots' linear speed v and angular speed ω can be expressed as:

$$v = \frac{1}{\Gamma_{\parallel}}(f_R + f_L) \tag{3.1}$$

$$\omega = \frac{L}{\Gamma_z}(f_R - f_L) + \frac{1}{\Gamma_z}(\tau_R + \tau_L) \tag{3.2}$$

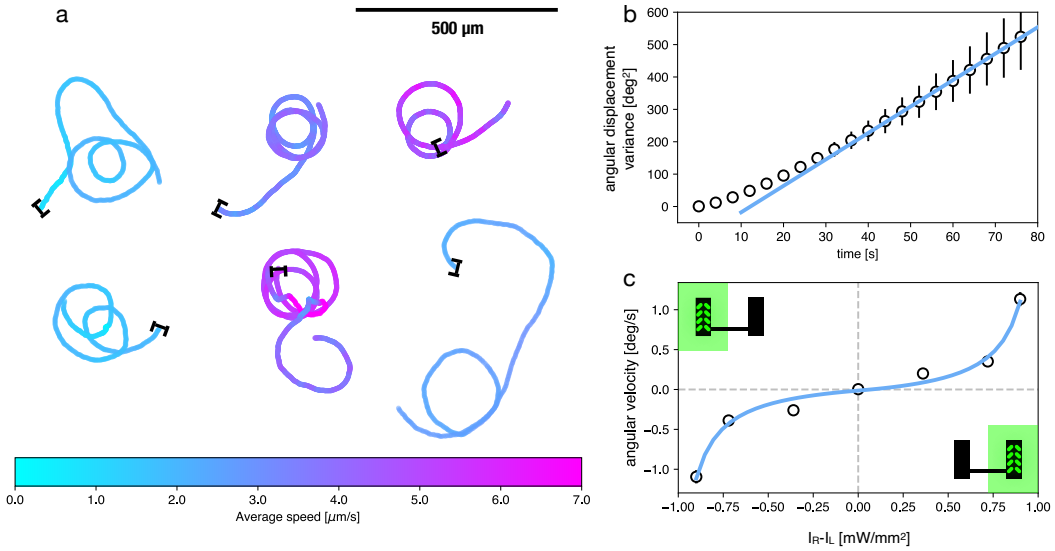

Figure 3.3. Uncontrolled microbot dynamics a) When exposed to a uniform illumination, microbots tend to follow circular trajectories due to the natural propulsion variability of bacteria filling the two engines. Line colors encode instantaneous speed as indicated in the colorbar. b) The variance of angular displacement as a function of elapsed time evidences the presence of fluctuating noise as a diffusive term that increases linearly with time. Circles represent an average over time origin and over seven microbots. Error bars are the standard error of the mean. c) Angular speed as a function of the difference in light intensity between the right and left engine. Solid line is the least-squared fit with the model expressed in Equation 5 and discussed in the text.

where f_R and f_L are the total forces and τ_r and τ_L are the torques applied by bacteria on the right and left engines, respectively.

In a perfectly symmetrical system under homogeneous green light illumination, one would expect zero torque and equal forces on both units, resulting in a straight path for the microbot. However, in practice, we observe circular trajectories (see figure 3.3 a). This non-zero angular velocity may be attributed to asymmetries in f_R and f_L or net torques τ_R and τ_L applied by the bacteria.

Asymmetries arise from natural variations in the thrust force generated by individual bacteria and the occasional presence of more than one bacterial cell in a single microchamber, despite the design intended for single-cell occupancy. Additionally, the inevitable roto-translational coupling with the substrate, which influences bacterial motion over solid surfaces, can contribute to these asymmetries.

Interestingly, we observe circular trajectories in both clockwise and counterclockwise directions, suggesting that roto-translational couplings do not play a major role here. The trajectories of these microbots also exhibit noise, quantified by the variance of angular displacement over time (Figure 3.3). A clear linear increase in variance indicates a diffusive component in the angular displacement, superimposed on the average rotation.

The force generated by each engine depends on light intensity, similar to individual bacterial cells. This relationship can be modeled as:

$$f(I) = f_0 \frac{I}{I+K} \tag{3.3}$$

where I is the power density of the projected green light and K is a threshold value. When $I \gg K$ proteorhodopsin photocurrents saturate, and bacteria trapped inside the microchambers exert a maximal thrust f_0 on each engine. For simplicity, we consider symmetric microbots, assuming $f_R = f(I_R)$ and $f_L = f(I_L)$, neglecting τ_R and τ_L. Substituting these expressions into the equations for linear and angular speeds, we obtain:

$$v = \frac{v_0}{2}\left(\frac{I_R}{I_R+K} + \frac{I_L}{I_L+K}\right) \tag{3.4}$$

$$\omega = \omega_0\left(\frac{I_R}{I_R+K} - \frac{I_L}{I_L+K}\right) \tag{3.5}$$

Here, we can now introduce the maximum value for linear speed $v_0 = 2f_0/\Gamma_\parallel$ and that for angular speed $\omega_0 = f_0 L/\Gamma_z$. The maximum linear speed v_0 occurs when light intensities on both engines are much greater than the threshold K. Maximum angular speed ω_0 is achieved when one engine is illuminated well above the threshold and the other engine is not illuminated.

To validate our theoretical models, we measured the angular velocity of microbots under unbalanced illumination conditions. By averaging the results over time and across multiple microbots, we obtained the data presented as circles in Figure 3.3c. The theoretical expression for angular speed (Equation 5) fits the experimental data well, as indicated by the blue line in Figure 2c. The best-fit parameters were found to be $\omega_0 = 1.30 \pm 0.07 deg/s$ and $K = 0.17 \pm 0.05 mW/mm^2$. These fits are consistent with previous studies on light-driven propulsion in *E. coli*.

3.2.2 Microbots under dynamic feedback

To navigate a microbot towards a predefined target effectively, it is essential to control the power of its two propulsion engines. We can describe the microbot's position vector relative to the target as $\mathbf{r}$ and its orientation as $\hat{\mathbf{e}}$. The angular distance θ between the direction $-\hat{\mathbf{r}}$ and $\hat{\mathbf{e}}$ is crucial in determining the microbot's trajectory. So here we put forth the strategy for adjusting the propulsion forces to ensure the microbot reaches its target. Following [130], the time evolution of θ will be given by

$$\dot{\theta} = \omega(\theta) + \frac{v(\theta)\sin\theta}{r} \tag{3.6}$$

The angular distance θ evolves over time based on the microbot's linear and angular speeds, $v(\theta)$ and $\omega(\theta)$, respectively. These speeds are controlled externally by selecting appropriate response functions $f_R(\theta)$ and $f_L(\theta)$for the right and left engines, tailored to the measured value of θ.

Under uniform, saturating illumination, a symmetric microbot will experience equal forces on both engines ($f_R = f_L = f_0$), resulting in a constant linear speed $v_0 \propto f_R + f_L$ and a vanishing angular speed $\omega \propto f_R - f_L$. Unless the microbot is

initially pointed directly at the target($\theta = 0$), the angular distance will eventually stabilize at a non-zero value $\theta = \pi$, causing the microbot to move away from the target.

To ensure the microbot reaches the target, we need to devise a navigation strategy encoded in the functions $f_R(\theta),\ f_L(\theta)$. The first requirement is that $\theta = 0$ must be a stable fixed point. For small values of θ, we can expand $\omega(\theta) \sim -\omega_0'\theta$ and $v(\theta) \sim v_0$ to linearize the dynamics in Eq.3.6 as:

$$\dot{\theta} = -\left(\omega_0' - \frac{v_0}{r}\right)\theta \tag{3.7}$$

As already discussed in [130], stability requires that $\omega(\theta)$ has a steep negative slope so that $\omega_0' > v_0/r$. The angular speed can only be modulated in a finite range of values $[-\omega_0, \omega_0]$ whose extremes are reached when one motor is running at full power f_0 and the other one is off resulting in $\omega_0 = f_0 L/\Gamma_z$ (Eq.3.2). To ensure aiming stability, it is therefore advisable to increase the slope of $\omega(\theta)$ around $\theta = 0$ by concentrating the entire dynamic range in a restricted angular interval $[-\theta_0, \theta_0]$.

This can be achieved by choosing the functions $f_R(\theta)$ and $f_L(\theta)$ as in Fig.3.4b. The angular speed will then have a constant slope $\omega_0' = \omega_0/\theta_0$ throughout the interval $[-\theta_0, \theta_0]$, see Fig.3.4c.

With this choice for $f_R(\theta)$ and $f_L(\theta)$, aiming stability, as established by Eq.3.6, will be guaranteed until the distance to the target falls below a critical value:

$$r_c = \frac{v_0}{\omega_0'} = \frac{2\Gamma_z}{L\Gamma_\parallel}\theta_0 \tag{3.8}$$

If we aim for a minimum approach distance to the target of less than r_c, the microbot may miss the target and move away from it indefinitely before returning back [130]. However, if we use $f_R(\theta)$ and $f_L(\theta)$ as in Fig.3.4c, *i.e.* such that the angular velocity is maximum when $|\theta| > \theta_0$, then the microbot will hold in an eccentric circular orbit around the target with a minimum approach distance given by $r_c \cos\theta_0/2\theta_0$. In our case we choose $\theta_0 = \pi/4$, so the minimum approach distance is $\simeq r_c/2$.

Real systems will always be affected by a substantial amount of noise from thermal agitation and fluctuations in the propelling force and arrangement of bacteria. In a noisy environment, pointing stability is an even more crucial requirement, and failure to reach the target due to random reorientation requires efficient mitigation strategies to keep the orbit confined within a narrow target zone (Fig.3.4d).

To automate the control of multiple microbots we couple a DMD projector to the microscope objective to address individual microbots with independently controlled illumination on the two engines. Using the same objective for imaging and projection allows us to shape the speed of bacteria with a spatial resolution that matches that of the imaging system[113, 123]. Multiple microbots can be controlled simultaneously by a central computer that continuously monitors their positions and calculates tailor-made light patterns to guide them along a pre-programmed task. In this work, we concentrate on path planning; *i.e.* moving microbots through a sequence of target destinations. To this end, a computer vision algorithm tracks the position and orientation of microbots and computes the angular distance θ from the

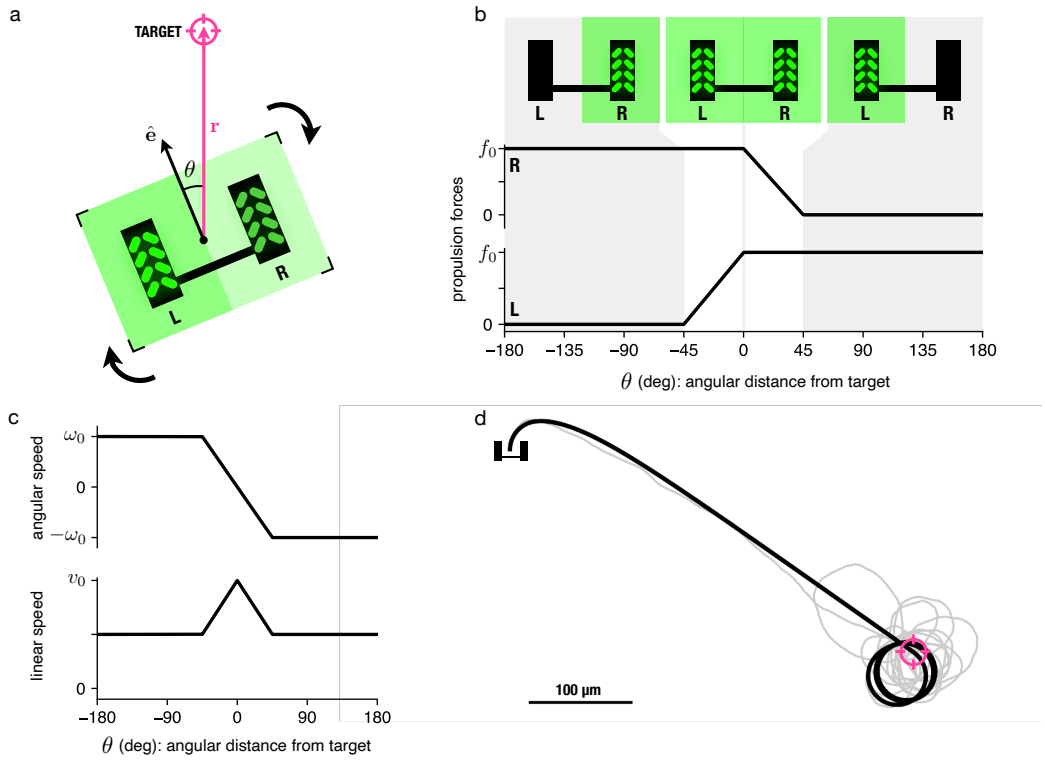

Figure 3.4. Navigation strategy. a) Definition of geometric variables. b) Dependence of left and right force on angular distance from target. When the microbots point in a direction more than 45 degrees away from the target, one motor is switched off while the other runs at maximum speed, achieving maximum torque. For deviations of less than 45 degrees one of the two engines is progressively turned off with a linear dependence on θ. c) Angular and linear speed as a function of angular distance θ when right and left forces are set as in b). d) A numerical calculated trajectory using ω_0 and v_0 parameters as extracted from experiments. The microbot points to the target and then settles in a circular eccentric orbit around it. Gray line is a simulation with the same parameters plus rotational diffusion with diffusivity extracted from the fit in Fig.3.3b.

next target. We then calculate the intensities on the right and left engines in order to implement the navigation strategy $f_R(\theta), f_L(\theta)$ illustrated in Fig.3.4b. When $|\theta| > \theta_0 = 45°$, one engine is turned off while the other one runs at full power so that the microbot rotates at maximum speed to decrease the angular distance to the target. When $|\theta| < \theta_0$, we always keep one engine at full power while lowering light intensity on the other one with a linear dependence on θ (see Fig.3.4b). As discussed before, this choice of navigation strategy guarantees aiming stability and also confined orbiting around the target. We defined a path consisting of three non-aligned targets A,B,C placed at a relative distance of approximately 500 μm (Fig.3.5a). When the distance to the target falls below 50 μm, the microbot turns to reach the next target along the path. Eventually, the final target C is reached, light is turned off on both engines and the microbot stops. Fig.3.5a shows a sample trajectory of a microbot. The black arrows represent the orientation of the microbot, while the magenta arrows point to the target. For most of the trajectory, the black

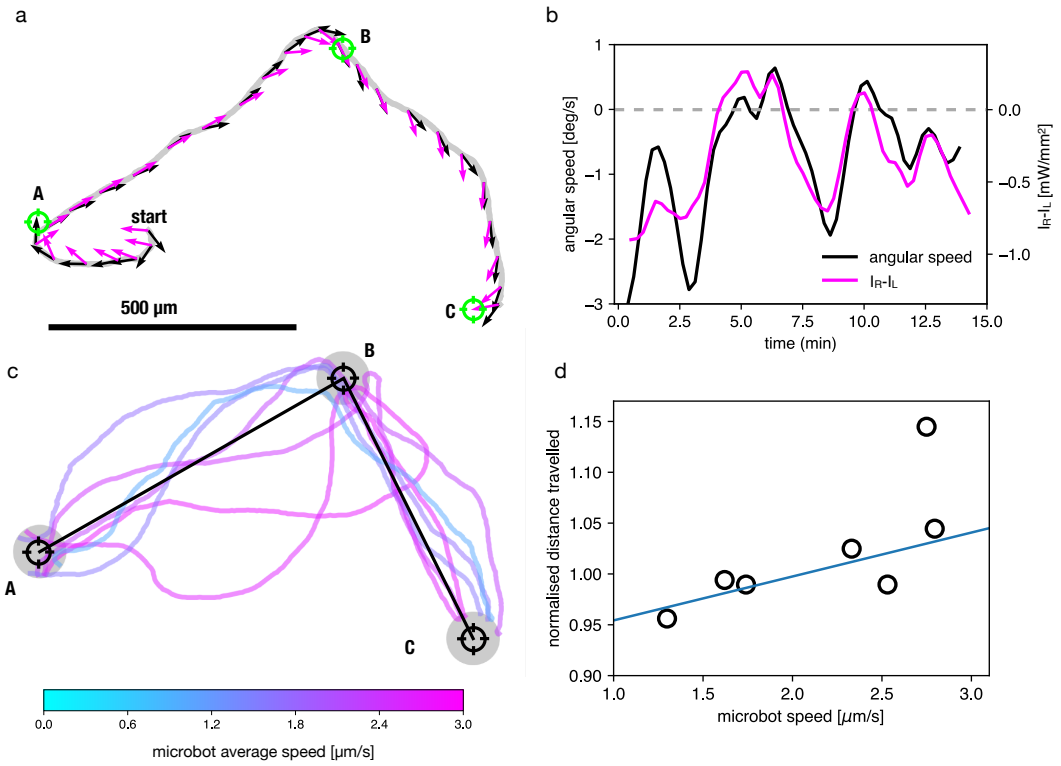

Figure 3.5. Path planning. a) Sample trajectory of a microbot following a path consisting of three non-aligned targets A,B,C. Black arrows indicate microbot orientation $\hat{\mathbf{e}}$ while magenta arrows point to the target. b) The angular speed along the microbot trajectory shown in a) is reported in black together with the right/left imbalance of light intensity on the two engines (magenta). c) Different microbots performing the same three target task (n=7). Line colors encode mean speed as indicated in the colorbar. d) Total traveled distance shows a weak correlation with microbot average speed.

arrow is rotated counterclockwise relative to the direction of the target (positive angular distance θ) and must be corrected with a negative rotation (clockwise). This is most clearly depicted in Fig.3.5b showing the time evolution of the angular velocity of the same microbot. The latter closely resembles the modulation of the difference between the light intensities projected on the left and right engines also reported in figure.

Figure 3.5 c, shows the trajectories of 7 microbots navigating through the same three-target path. The colours of lines encode the average speed over the entire path. Depending on their initial position and orientation, the seven microbots reach the first target (A) following very different paths. When they move towards B, they all start from neighbouring positions, so that their trajectories wander a little less. In the last stage, since they all arrived at B from A, they also share more similar initial orientations, so that the final paths seem less dispersed and more straight. The completion time for this task ranges from 10 to 20 minutes depending on the microbot, with an average value of 13 minutes. In general, the faster microbots appear to wander more and reach the final target after travelling a greater total distance. In Fig.3.5d we report the contour length of each trajectory, normalised to

the minimum distance given by the length of the straight paths joining the target centers (black line). Because target regions are not point-like, some trajectories may be shorter than the distance between target centers. Interestingly the dispersion of the total travelled distance is only of about a few 10%. Moreover, almost all of the shuttles travelled a total distance greater than the optimum by only $2\% - 15\%$. This distance is clearly correlated to microbot speed with the slower shuttles staying closer to the optimal trajectory. This observation may seem to be in agreement with what was already pointed out in [130] and expressed by Eq.3.7, namely that a higher velocity v_0 reduces the stability of pointing. It should be noted, however, that in our case, v_0 and ω_0 should vary in a correlated way being both proportional to f_0. One possible explanation for the increased tortuosity of fast microbots could be that the propulsion of each motor fluctuates with multiplicative noise.

The main advantage of using light as an external control field is that multiple microbots can be controlled independently to collaborate on the same task. To demonstrate this, we simultaneously programmed two microbots to move along the same three targets path. Fig.3.6 shows four frames of experiment video showing two microbots independently programmed to move from one target to another. Again, as with the individually guided microbots in figure3.5c, we note that while from A to B the trajectories are quite far apart, in the last section they become very close. The central control algorithm ignores possible collisions between two microbots. These aspects could become important when the number of microbots grows, but fortunately, their management would only require a modification of the algorithm by introducing, for example, effective interactions that mimic visual perception between the different microbots [131].

3.2.3 Tracking and control algorithms

The python script we designed for controlling and tracking the movement of a microstructure uses image processing and pattern projection techniques. The code utilizes a combination of hardware control, image processing, and machine learning libraries to accomplish its tasks. The main components of the code include a class defined to handle template extraction and manipulation while the main control class is responsible for the main functionality, including the control loop, tracking, and intensity adjustments for driving the microstructure to the target.

The code utilizes several libraries to serve different purposes, namely; cv2 (OpenCV): For image processing and computer vision tasks and torch: For tensor operations and GPU acceleration, while also having custom function to acquire images from the camera and project patterns from the DMD.

The algorithm is designed to handle the creation and manipulation of templates used for tracking. The constructor allows for a region of interest (ROI) to be passed. The template is extracted from the image data itself, and is stored for future reference. We developed methods that allow dynamic manipulation of the template, enabling operations like rotating the template for alignment and cutting out specific regions.

The main section of the algorithm handles the primary control loop for tracking and driving the microstructure towards predefined targets. The class initializes various parameters, like template, duration of the experimental run, processing the feedback and updating the projected pattern. It also periodically shows images

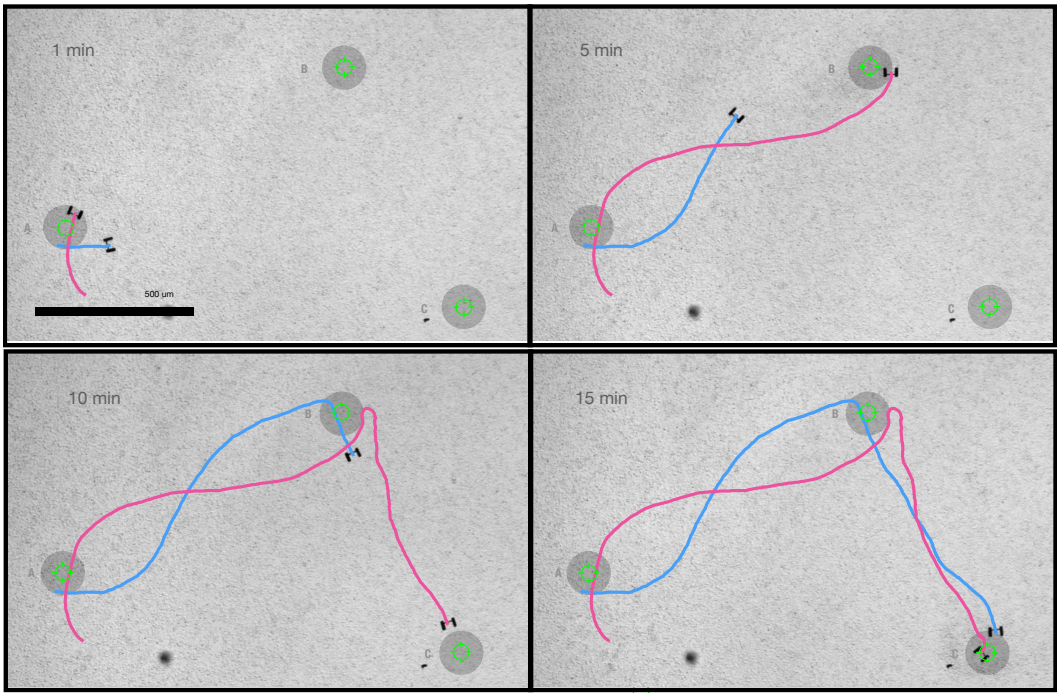

Figure 3.6. Simultaneous control of multiple microbots. Frames from experiment video showing two microbots that are being simultaneously programmed to perform the three-target task. Scale bar on the first frame is 200 μm.

to visualize the current state of the experiment and patterns superimposed on the microbot, while continuously saving the results for analysis. If the total tracking time is exceeded, it stops the loop and saves the final state.

The tracking is based on correlation-based template matching to find the position and rotation of the microstructure and updates the position and angle of the microstructure based on the acquired image with respect to that of the given target. Depending on the availability of CUDA, it uses GPU-acceleration method.

3.3 Efficiency of the microbot

Using simple scaling arguments we can discuss the possibility of scaling up the size of our microbots. For example, by increasing the length of the engine we could accommodate more microchambers, the number of bacteria would increase, and proportionally so would the applied thrust f_0. At the same time, the translational viscous drag $\Gamma_{\|}$ would also increase linearly with the propeller length so that the propulsion speed would not change with size. Thus, there is no clear advantage in increasing the size of the propulsion units, especially considering that one of the most promising applications for the microbots might be in single-cell transport. For a fixed propeller size the distance between the two units should be chosen in order to increase the steering speed Ω. Calling $\gamma_{\|}$ and γ_z the translational and rotational drag of the isolated left and right units, we can obtain the drag on the composed

structure as a function of the distance L[132]:

$$\Gamma_{\parallel} = 2\gamma_{\parallel} \ , \ \ \Gamma_z = 2(\gamma_z + L^2\gamma_{\parallel}) \tag{3.9}$$

where we have neglected hydrodynamic interactions between the two units . We can then express the maximum angular speed ω_0 as a function of L

$$\omega_0 = \frac{f_0 L}{\Gamma_z} = \frac{f_0 L}{2(\gamma_z + L^2\gamma_{\parallel})} \tag{3.10}$$

where $f_0 L$ is the maximum torque applied by the bacteria. We find that there's an optimal value for L which maximizes ω_0 and it is given by $\sqrt{\gamma_z/\gamma_{\parallel}}$. Experimental estimates for $\gamma_{\parallel}$ and γ_z confirm that our choice for L is very close to this optimal value (check section 2.4). Let us now turn to energy considerations. Within our microbots, bacteria work to push the SU-8 chassis at a speed $v \simeq 2$ µm/s. The viscous medium resists this motion with a drag coefficient $\Gamma_{\parallel} = 0.67$ pN s/µm that we extracted from the Brownian mean square displacement of the empty structures (check section 2.3.2). The energy output can be defined as the mechanical work performed by the bacterial thrust $P_{out} = \Gamma_{\parallel} v^2 \simeq 3$ aW. On the input side, flagellar motors are ultimately powered by projected light whose integrated flux over the two engines running at maximum power is about $P_{in} = 100$ nW resulting in an overall efficiency of light to work conversion of $3 \cdot 10^{-11}$. This figure is consistent with that reported for rotary machines actuated by light-driven bacteria [114] and, as already discussed there, it is orders of magnitude larger than the efficiency of light-driven micromachines actuated by radiation pressure [56, 53].

3.4 Conclusion

We show how photokinetic bacteria can self-organize within a 3D microfabricated structure to produce a light-controlled microbot. These microbots can be individually programmed by a central computer to move over a sequence of checkpoints located arbitrarily over a millimeter-sized area on a microscope cover glass. In addition to acting as a remote control of the microbots' direction, the light also provides the energy needed to generate self-propulsion. Previously proposed light-controlled biohybrid microbots used light as an on/off switch to control unidirectional rotational or translational motion [115, 116]. Other possible strategies for using light to guide microbots on a pre- scribed path involve the use of focused laser light to generate propulsion through cavitation-induced flows [133] or radiation pressure [5]. Typical power in these cases is on the order of tens of milliwatts per microstructure, whereas our microbots can operate with less than a microwatt of total power. This is due to the high efficiency of proteorhodopsin in converting energy from optical to electrochemical, so in principle it is possible to control hundreds of these microbots using only a few milliwatts of light, thus avoiding photodamage in biological applications and paving the way for swarm micro-robotics in lab-on-chip.

Chapter 4

Applications of the biohybrid microbot and 3D microstructures

After successfully demonstrating controlled movement of multiple microbots, the project shifted towards exploring different applications for them.

The original goal was to develop a micro robot for cell sorting in a microfluidic environment. However, as our capabilities grew and we gained a better understanding of the system, we realized that the microbots could be used to investigate other phenomena. One such project involved approximating geometric optics to guide our microbot using static light pattern.

In this chapter, I will discuss our current progress in use the microbot for studying the two projects. This involved creating new protocols for microbot post-development and better models for optimal driving strategies.

In the last section, we will explore the development of other 3D microstructures used for studying bacterial systems. These include investigations into defining pressure in active systems, as well as studying torque generation in the bacterial flagellar motor.

All of these works are part of ongoing research projects.

4.1 Application of microbot for transporting cargo beads

As our microbots can freely translate and be controlled in 2D space, their long term development is geared towards developing application in cell sorting in 2D sample space, like within microfluidic chips or petri dish. The two propeller design of the microbot enables capture of particles in between the propellers and the connector. The microbot, according to our design consideration can trap particles up to 20 μm. However, for all tests performed, we use silica beads of 10μm in diameter.

In the previous experiment, where we just wanted to guide the microbot through a series of check points, targets given to the microbot are simply coordinates in 2D space. Hence the reference point of the target with respect to the orientation of the microbot is fixed. Also, the algorithm considers the target completed if the microbot passes within the range on 50 μm from the center of target coordinate.

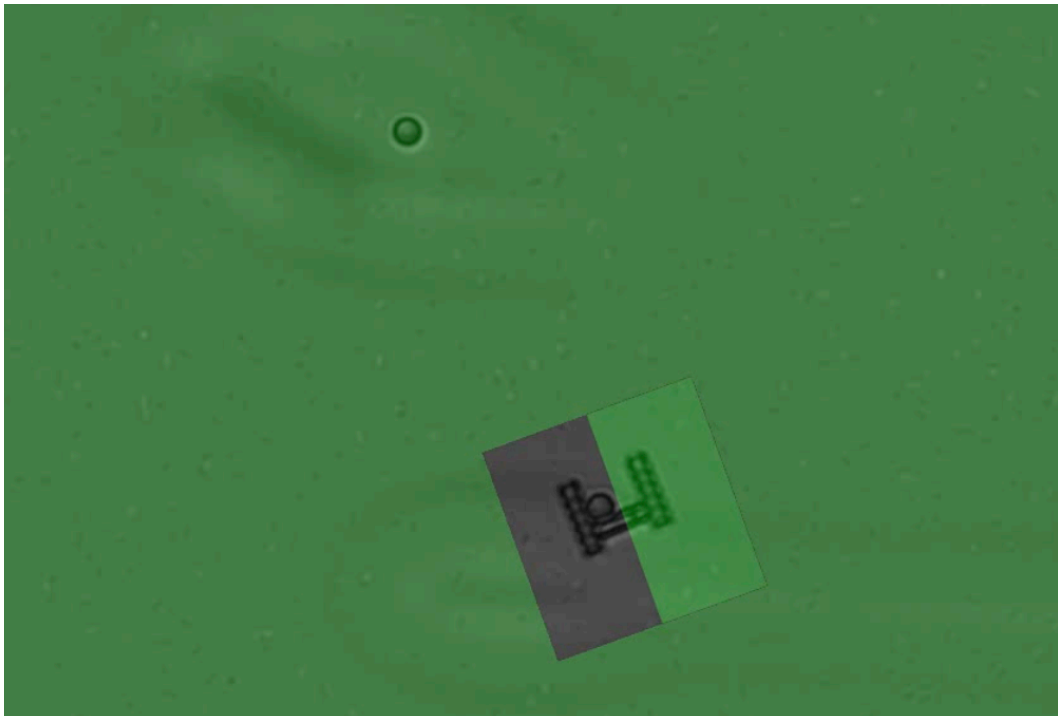

Figure 4.1. Frame from experiment showing a microbot under dynamic feedback transporting a bead of 10 μm. Image taken under 10X.

This distance is reasonable considering that it is approximately twice the body length of the microbot, but this range is quite large than the 10 μm diameter of the bead. Therefore, the control system of the microbot need to be improved more than what was previously reported.

If the microbot fails to capture the bead, it goes into an orbit like trajectory around the bead. This was already predicted by our numerical simulation (see reference 3.4) and other works [130].

Complexity also arises in this case of cargo transport because of the diffusivity of silica bead. As the bead diffuses and continuously shifts randomly within a range, the microbot needs to be constantly updated of the beads position. We manage this by using a simultaneous double tracking method, for the microbot and the bead it wants to capture. This allows us to continuously updated the target position. This tracking also helps us get a better estimate of the diffusivity of silica bead.

Diffusivity of a spherical object can simply be calculated by using the Stokes-Einstein equation:

$$D = \frac{k_B T}{6\pi\eta r} \tag{4.1}$$

where, D is the diffusivity, T is the temperature, η is the dynamic viscosity of the water and r is the radius of the particle.

In water, silica bead of 10μm carries a diffusivity of $4.37 \times 10^{-2} \mu m^2/sec$. However, our silica bead is in a bath of smooth swimming bacteria, whose speed changes by green light intensity. Therefore, the effective temperature around the bead itself can be considered as varying, as the number of collisions of the bacteria and the bead is

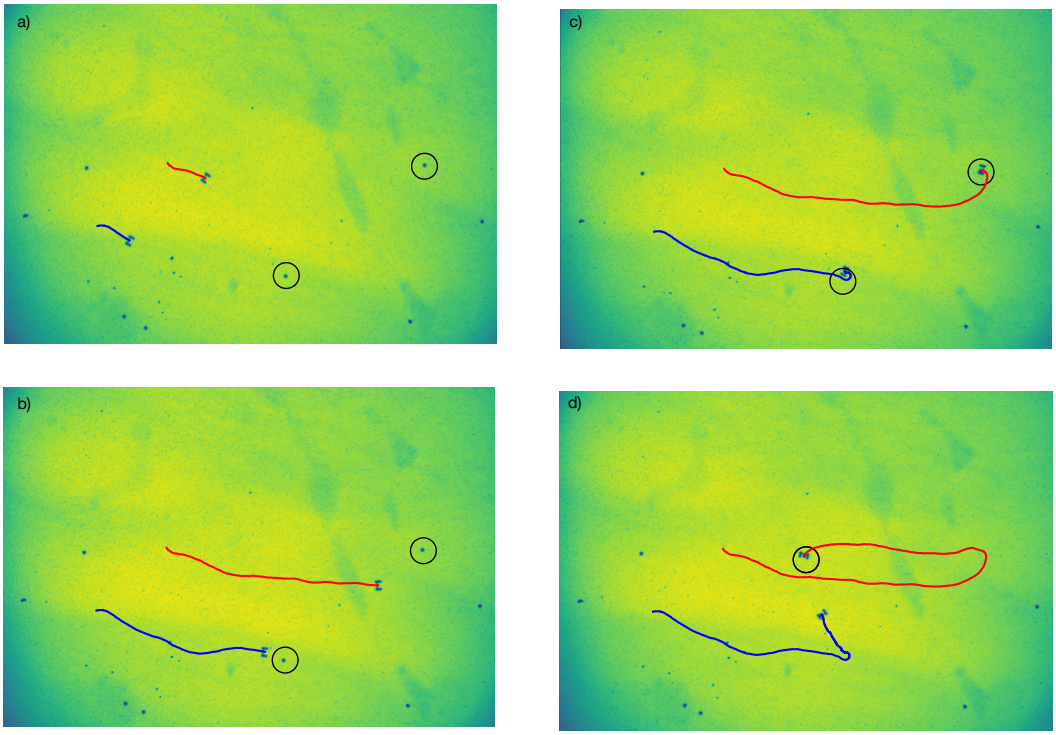

Figure 4.2. Frames from experiment video showing multiple microbots capturing and transporting beads of 10 μm. The images showing capture and transporting of silica beads. Images taken under 4X.

dependent on the density and motile fraction of the bacteria around the bead. For this we can use the previously mentioned tracking data to compute the MSD of the particle and adjust the navigation strategy of the microbot. This estimate is useful to make better driving models for the our microbot.

We have managed to capture and transport 10μm silica beads multiple times(see figure 4.2. However, we are facing problems regarding particle sticking. Currently we are working towards practically implementing theoretical strategies discussed for capture of passive particles by active agents using predator-prey pursuit strategies [134, 135, 130], and improving the systems capabilities and reproducibility. It also needs to be investigated further, if the capture of the bead, which is of similar dimensions to that of the microbot, changes the flow profile of the fluid around the microbot and its effects of the drag of the microbot-bead system.

4.2 Dynamics of microbots in geometric optics approximation

In 2022, Tyler Ross and colleagues explored the analogy between the principles of ray optics and the motion of self-propelled particles across resistance discontinuities [136]. This hypothesized a way to control the trajectories of self-propelled particles using a variant of Snell's law, traditionally used to describe the refraction of light.

Similar to how the ratio of refractive indices determines the path of a light ray,

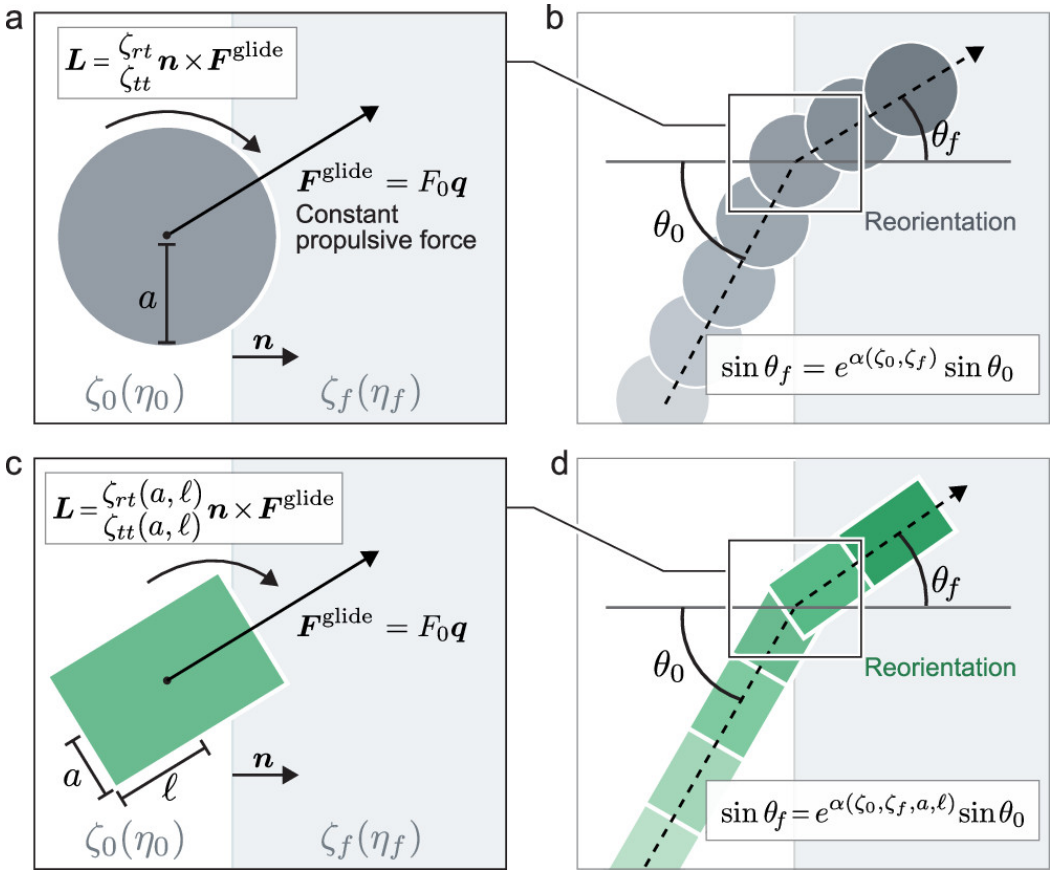

Figure 4.3. Illustration of disk-shaped and rectangular gliders moving over a resistance discontinuity. (a) Shows the forces and torques acting on a glider as it crosses a friction discontinuity. (b) These forces and torques result in the glider reorienting its trajectory around the resistance discontinuity. (c,d) The forces and reorientation of a rectangular glider vary based on its aspect ratio. Figure take from reference [136]

the ratio of resistance coefficients defines the trajectories of gliders. When a glider moves from a low-resistance to a high-resistance region (or vice versa), its speed and direction change due to differential resistance across its body, causing it to rotate and align along the normal to the discontinuity. This behavior is mathematically captured through torque and force balances, resulting in a reorientation akin to light refraction.

This presents an excellent opportunity to investigate the phenomenon using our microbots, which have self-propelling bacteria integrated into them, fitting the definition of an active colloid.

Eikonal equation for microbot path tracing

Lets start with tracing the path of our microbot, using the eikonal equation. We can describe the forward orientation of the microbot, moving with a velocity v, with a unit vector $\hat{e}$ and represent the vector pointing in its orthogonal direction as $\hat{t}$.

Now consider s, as the distance of the microbot from the point of origin and $\vec{R}(s)$ be the path curvature parameterized by the distance s and radius of curvature R.

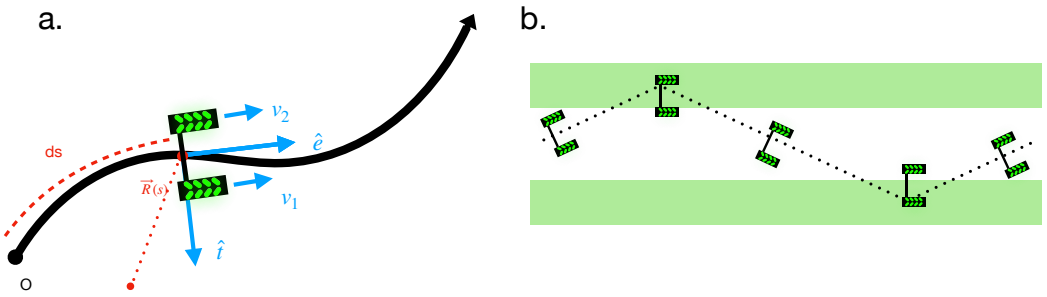

Figure 4.4. Illustration of microbot trajectory in a static pattern. (a) Shows the trajectory of the microbot along a curvilinear path, where, s is the distance of the microbot from the point of origin, $\vec{R}(s)$ is the path curvature parameterized by the distance s and radius of curvature R. v is the velocity, with a unit vector $\hat{e}$ describing the forward orientation of the microbot and the vector pointing in its orthogonal direction is $\hat{t}$. The velocities of the two propellers are v_1 and v_2 (b) Shows the hypothetical trajectory of the microbot in a static light pattern. The reorientation occurs as the propeller of the microbot moves into the high illumination region, forcing it to undergo a "reflection". This happens again of the opposing propeller makeing the trajectory analogous to "total internal reflection"

.

So, we can say that,

$$\hat{e} = \frac{d\vec{R}}{ds} \tag{4.2}$$

We can describe the velocity of each propeller as,

$$v_1 = v_0 + \frac{l}{2}\hat{t} \cdot \vec{\nabla} v \tag{4.3}$$

and

$$v_2 = v_0 - \frac{l}{2}\hat{t} \cdot \vec{\nabla} v \tag{4.4}$$

Therefore, the angular speed of the microbot, ω is,

$$\omega = \frac{v_1 - v_2}{l} \tag{4.5}$$

where, v_1 and v_2 are the velocities of the microbot propellers and l is the lenght of the connector rod (see figure 4.4).

Now multiplying by $\frac{1}{v}$, equation 4.2 becomes,

$$\frac{d}{ds}\frac{1}{v}\frac{d\vec{R}}{ds} = \frac{d}{ds}\frac{1}{v}\hat{e} \tag{4.6}$$

$$= \frac{1}{v}\frac{d\hat{e}}{ds} - \frac{\hat{e}}{v^2}\frac{dv}{ds} \tag{4.7}$$

But, we know that $ds = vdt$. So,

$$\frac{d\hat{e}}{ds} = \frac{d\hat{e}}{vdt} \tag{4.8}$$

$$= -\frac{1}{v}\hat{t}\omega \tag{4.9}$$

$$= -\frac{1}{v}\hat{t}\hat{t}\cdot\vec{\nabla}v \tag{4.10}$$

and we say that,

$$\frac{dv}{ds} = \hat{e}\cdot\vec{\nabla}v \tag{4.11}$$

Substituting the expressions for $\frac{d\hat{e}}{ds}$ and $\frac{dv}{ds}$ in equation 4.6, we get,

$$\frac{d}{ds}\frac{1}{v}\frac{d\vec{R}}{ds} = -\frac{1}{v^2}\hat{t}\hat{t}\cdot\vec{\nabla}v - \frac{\hat{e}}{v^2}\hat{e}\cdot\vec{\nabla}v \tag{4.12}$$

$$= -\frac{1}{v^2}(\hat{t}\hat{t} + \hat{e}\hat{e})\cdot\vec{\nabla}v \tag{4.13}$$

$$= -\frac{1}{v^2}\vec{\nabla}v \tag{4.14}$$

$$\frac{d}{ds}\frac{1}{v}\frac{d\vec{R}}{ds} = \vec{\nabla}\frac{1}{v} \tag{4.15}$$

Now, from the formal definition of the eikonal equation, we know that,

$$\frac{d}{ds}n\frac{d\vec{R}}{ds} = \vec{\nabla}n \tag{4.16}$$

where, n is the refractive index of the medium.

But, from equation 4.12, we show that,

$$n = \frac{1}{v} \tag{4.17}$$

So, in case of our microbots, we can make an analogy to the ray path of light, where the refractive index is substituted by inverse of the microbot's velocity. This can be further utilized to see, if by placing the microbot in a static gradient of light, there can be a change in the orientation of the microbot, due to the change in its speed and whether the microbot can trace a path analogous to "total internal reflection" (see figure 4.4 b).

However, there are some practical considerations in this system before setting up the experiment. These are partially due to the design of the chassis and how microbots behave in uniform light as seen in section 3.2.1. Under homogeneous illumination, the microbots tend to go under a circular trajectory due to the asymmetrical filling of the propeller chambers by the bacteria. This tendency can hinder the accurate measurements of the change in trajectory angle as the microbot crosses a sharp gradient head-on. Additionally, the bacteria face a slight delay in changing the speed from low intensity to high intensity of green light, usually of a few seconds.

To address these considerations, we designed an experiment where we shone a long tube-like light pattern curved around a center (see figure 4.5). This pattern has

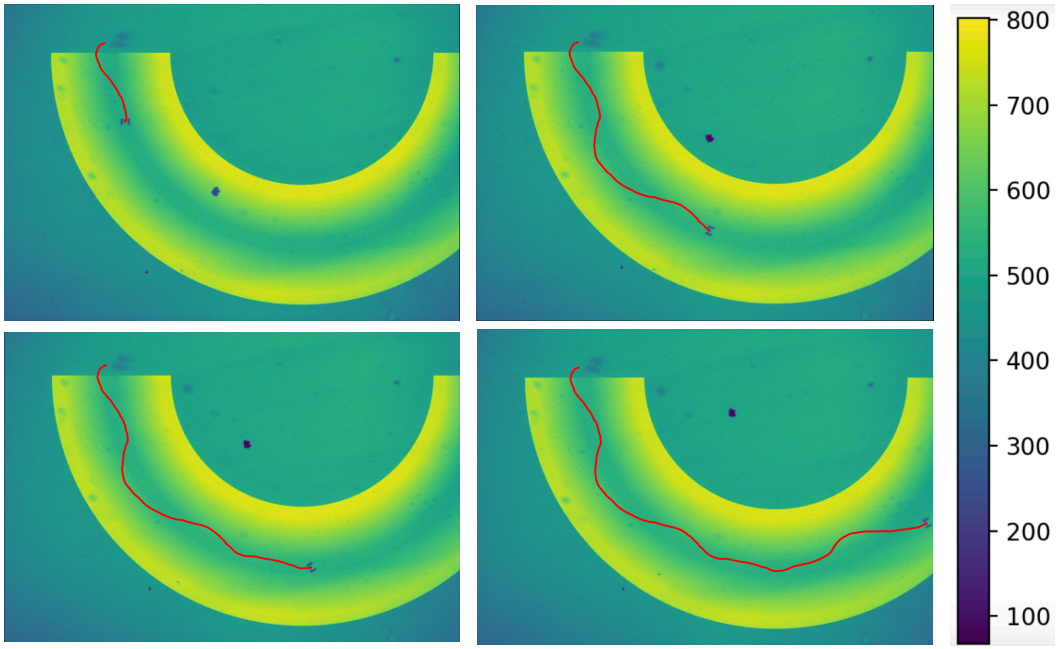

Figure 4.5. Frames from the experiment video showing the microbot in the static gradient pattern. The microbot is reflected when it enters a high intensity zone (yellow). The oscillatory behavior can be seen in the trajectory. Intensity (colour bar on right) shown yellow as the highest intensity region.

a low-intensity region (low velocity) in the center and high-intensity (high velocity) regions on both sides. There is no sharp transition between the high-intensity and the low-intensity region, but a transition gradient with a quadratic potential. In the experiment, the microbot is guided to the central region from one end of the tube, and then the dynamic feedback control is switched off. As the microbot starts moving forward, it is forced to stay in the low-intensity region. Whenever it drifts into the high-intensity region exposing one of its propellers to higher light intensity, the bacteria in that propeller start pushing at a higher speed, thus reorienting the entire structure toward the other edge of the tube where there is another high light intensity region and repeating the cycle of moving forward while reorienting toward the opposite edge.

In this case, the trajectory of the microbot should be analogous to a light ray propagating through a curved graded index fiber. We know that, in this case, rays follow sinusoidal paths. Indeed oscillatory behavior can be observed in the reported trajectories (see figure 4.5). Since this work is still in progress, many aspects need to be explored, with the most important one being identifying any critical angle that keeps the microbot on its oscillatory but steady path. It necessitates precise tracking and detailed measurement of the bacteria's speed. This marks a non-traditional approach to exploring new potential phenomena and driving strategy using our light-driven bio-hybrid microbot.

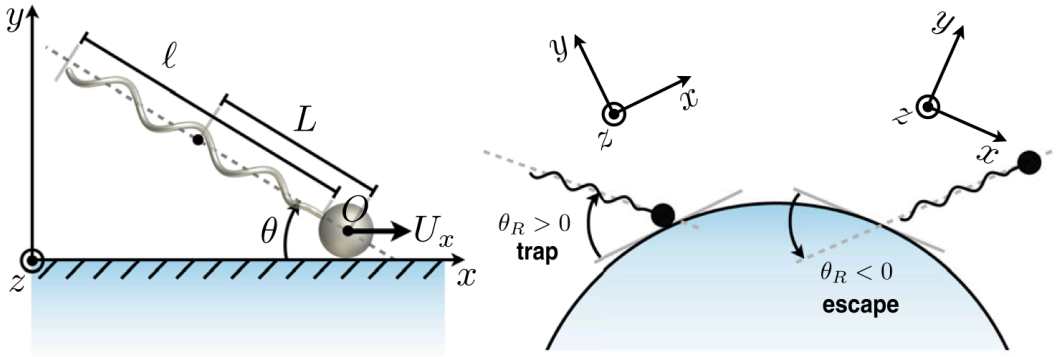

Figure 4.6. Schematic hydrodynamic model of convex wall entrapment. Trapped cells swim at a finite angle with the wall and a precise relation exists between the swimming angle at a flat wall and the critical radius of curvature for entrapment. Figure taken from the reference [140]

4.3 Active pressure around curved boundaries

Active matter is a driven system in which energy is supplied directly, isotropically and independently at the level of the individual constituents, which in turn dissipate it to achieve persistent motion [118]. While it can be concluded that active particles are well capable of generating mechanical power, the thermodynamic concepts like temperature and pressure in these cases are not very well defined.

Currently there are multiple schools of thought trying to define the concept of pressure and often contradicting each other [137, 138]. All of these arguments are mostly based on simulation and theoretical studies, as currently there are only limited number of experimental studies conducted to explore these concepts.

One example of an attempt to experimentally verify this concept was done by Pellicciotta and colleagues, by studying the transportation of colloidal bead by shaping the pressure exerted by the bacteria around it [139].

We define bacterial active pressure simply as the force swimming bacteria exert on the container wall holding them. In previous studies in our lab, it was found that swimming bacteria can get entrapped, due to hydrodynamic interaction with a convex wall (see figure 4.6) [140]. This was due to the bacterial cell swimming at an angle respect to the surface. This has been further studies and confirmed by tracking individual bacterial cell under three-axis holographic microscopy [141]. However, wall entrapment occurs only below a certain radius of curvature. This relation is derived as :

$$R^* \approx \frac{2}{3}\frac{l}{\sin\theta_\infty} \tag{4.18}$$

where, R^* is the radius of entrapment, l is the length of flagellar bundle and θ_∞ is the swimming angle at stable equilibrium for an *E. coli* cell. This entrapment radius can therefore easily be calculated to be $R^* \approx 57\mu m$.

Mallory and colleagues have shown that a curved passive tracer particle becomes effectively active when placed in an active bath, using numerical simulations [142]. This activity of the tracer particle is a function of its curvature.

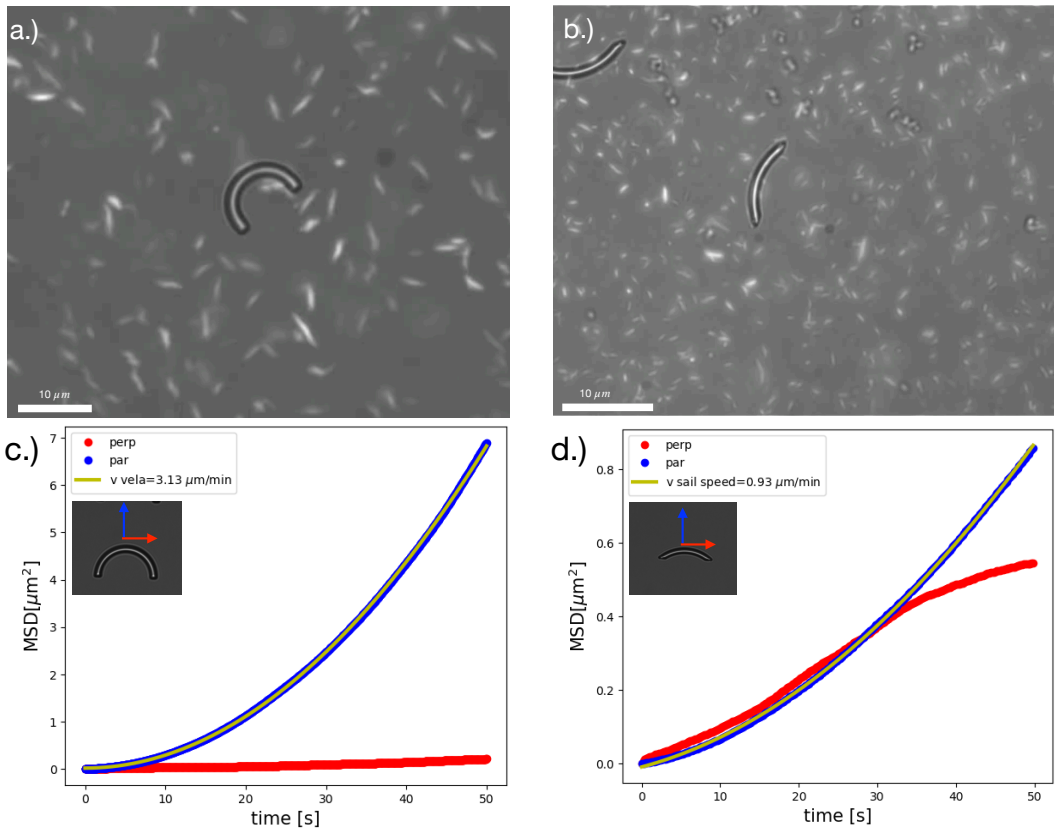

Figure 4.7. Curved passive tracers in a bath of florescent bacteria (a) Curved tracer with radius of curvature equal to 10 μm, (b) Curved tracer with radius of curvature equal to 20 μm. c) Speed calculation of curved tracer with radius of curvature equal to 10 μm using MSD. (b) Speed calculation of Curved tracer with Radius of curvature equal to 20 μm.

Based on this information, we propose that when a curved free-floating boundary is placed in a bath of swimming bacteria, the bacteria can only exert pressure from the concave side of the boundary if the radius of curvature is less than 57 μm. We can obtain a more accurate measurement of the pressure exerted by the bacteria by calculating the speed of the curved boundary. Then, we can compare the speeds of different structures with the same length but different curvature.

We fabricated these curved tracer particles of the same arc length but different radius of curvature, 10 μm and 20 μm, using the two photon polymerization and placed them in a bacterial bath. We used smooth swimming strain of bacteria with florescence for better visualization. We found that there is a significant difference of speed in these two structures. The structure with lower radius of curvature,10μm, has a speed of 3.13 μm/min, while the one with high radius of curvature, 20μm has a speed of 0.93μm (see figure 4.7).

This is consistent with the theoretical results, however this work is still under progress and therefore we require more data to investigate this phenomenon further.

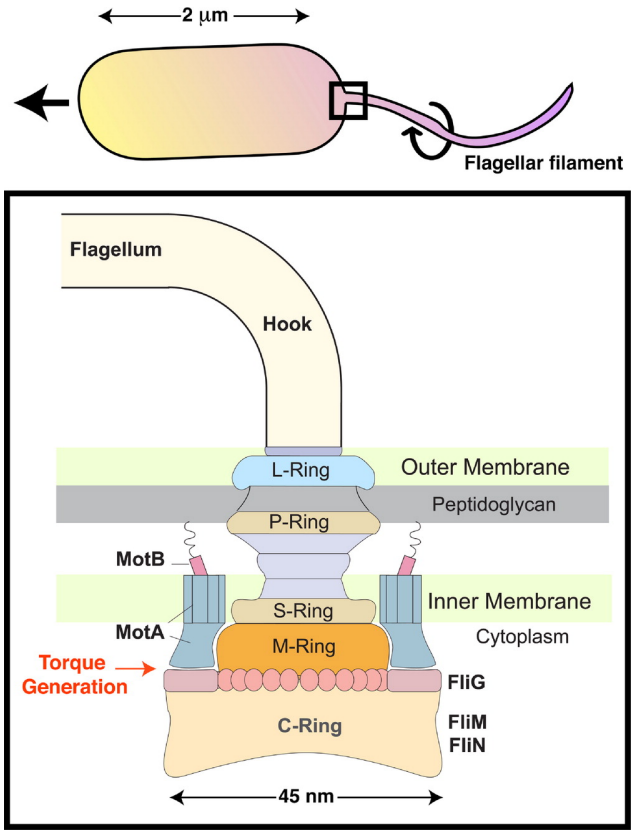

Figure 4.8. Schematic of a bacteria Flagellar motor of a gram negative bacteria, like *E. coli*. The rotor of the flagellar motor's basal body is surrounded by FliG proteins, forming the C-ring. These proteins interact with the stator-unit loops to produce torque and spin the flagellum. Each stator unit consists of MotA and MotB proteins, with the latter anchoring the stator to the peptidoglycan layer, enabling torque generation through the MotA–FliG interaction. The motor can support up to 11 active stator units, depending on the load. Image taken from the reference [144].

4.4 Light-mills for measurement in torque generated by a bacterial motor

A rotory motor can only be found in two places. In a human machinery or in flagellated bacteria. The bacterial flagellar motor (BFM) is a uniquely interesting nanomachine, which is purely a product of evolutionary pressures of natural selection (see figure 4.8). This motor, which is responsible for the fundamental biological processes like chemotaxis due to its role in bacterial locomotion, is just 45 nm in diameter and is composed 25 different proteins. BFM functions with nearly 100% efficiency. Spinning at around 300 Hz or 18000 rpm , the *E. coli* motor is capable of producing a power of roughly 1.5 × 105 pN nm/s [143].

The connection between the torque of the motor and its speed is a fundamental dynamic characteristic of the BFM. The torque applied by this motor can be studied by attaching a polystyrene bead to the flagellar of an *E. coli* cell (attached to the surface) and driving it externally using optical tweezers [143, 145]. This gives the

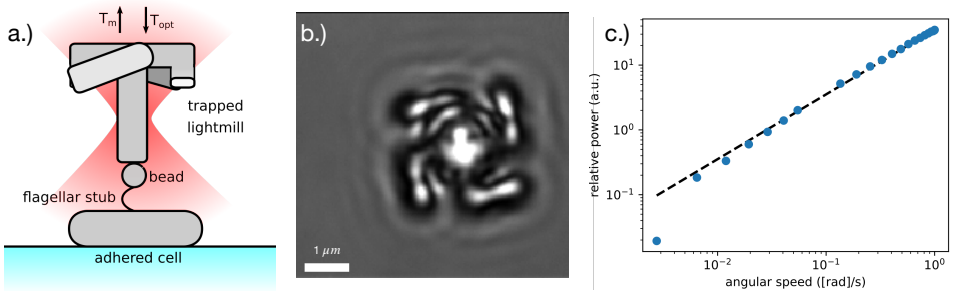

Figure 4.9. Study of bacteria flagellar motor of *E. coli* using 3D fabricated light mills and optical tweezers. (a) A schematic of the experiment showing attachment of the microfabricated light mill and to the bacteria with bead. (b) Snapshot of the experiment showing a optically trapped light mill. (c) Plot of power applied using optical trap vs angular speed. The plot shows that the angular speed scales linearly with laser power.

possibility of applying external torque to the motor in either same direction as to the motor (clockwise) or opposing (anti-clock wise) direction.

Measurements using this method have shown some anomaly in the torque vs speed curve of the motor. When driven backward, there seems to be a sharp increase in the motor torque. This bring up the question of whether this anomaly is an artifact in the measurements or its origin lies in the torque generating mechanism of the motor due to some non hydrodynamic internal friction?

To investigate this, we fabricate light driven mill using the two photon polymerization. These light driven mills generate torque when trapped using optical tweezers due to light scattering [146, 56]. This torque has its origin due to the helical shape of the light mills. The concentrated beam from the optical tweezers creates a trapping force to keep the light mill in place and also induces rotation. By attaching such a structure to the hook of the flagellar motor we can precisely calculate the applied external torque as the rate of rotation is dependent upon the laser intensity. As for the bacteria we use a non tumbling strain with sticky flagella for bead and microstructure attachment, which has been adhered to the surface.

The rotation dynamics of the light-mills are simple: The change in momentum of the light as it is reflected by the spiral structure applies a force to the object, and this force is balanced by the resistance from the spinning particle's viscosity [146]. It is given by:

$$M = D\omega \tag{4.19}$$

where, M is the angular momentum, exerted on the body by the momentum change of the deflected photon, D is the viscous drag coefficient of the rotating body, and ω is the angular speed.

The angular speed of the microstructure can be calculated by tracking its rotation under different laser power. The tracking is done by a template matching algorithm similar to take explained in section 3.2.3. The plot of angular speed vs laser trapping power shows that the angular speed scales linearly with laser power, figure 4.9 c. This in coherence with previous studies [146].

This provides us with tools to study and explore the working of bacterial flagellar motor further.

4.5 Conclusion

The microbots, with dual propeller designs, can capture and transport 10 μm silica beads in a 2D samples. Challenges here include enhancing control systems to improve precision, managing bead diffusivity through simultaneous tracking , implementing theoretical predator-prey pursuit strategies and understanding the fluid dynamics alterations due to bead capture.

We explore the application of the microbot to study phenomenon inspired by principles of ray optics. While it is possible to control of microbot trajectories using light intensity gradients, akin to Snell's law in optics, experiments should be designed to overcome practical issues like the asymmetrical filling of propeller chambers and the bacteria's response time to light intensity changes. Preliminary results suggest potential new applications to study active matter related phenomenon using these light-driven microbots.

Using the two photon polymerization's ability to rapidly prototype new structures, we also investigate other research problems in the field of active matter and bacterial motility.

Investigations in active pressure exerted by bacteria on curved boundaries suggests that pressure varies with the curvature radius. Experimental results align with theoretical predictions but require further data for comprehensive understanding.

Using light-driven mills fabricated through two-photon polymerization, studies were conducted in torque-speed relationship of bacterial flagellar motors. This method aims to resolve anomalies observed in previous measurements and understand torque generation mechanisms in bacterial motors.

Part II

Methodologies

Chapter 5

Two photon micro-fabrication

5.1 Two photon polymerization

Two-photon polymerisation (TPP) is a sophisticated fabrication technology crucial for constructing microscale and nanoscale structures. This process is fundamentally based on the principle of two-photon absorption (TPA). In TPA, the photoinitiator (PI) within the two-photon polymerizable resins (TPPR), also called photo-resist, is sensitized through the simultaneous absorption of two photons. This absorption occurs via an intense pulsed laser beam that provides the necessary photon flux. The core mechanism of TPP is a two step process. First is the sensitization of the photoinitiator; where the PI is activated by two-photon excitation, a nonlinear optical process that allows the use of near-infrared light rather than ultraviolet. This enables deeper penetration of the light with minimal damage to surrounding materials. Second is the cross-linking of the TPPR. where, once the PI is activated, it initiates the polymerization of the surrounding monomer or oligomer mixture. The cross-linking of these materials forms the solid structures designed in the TPP process. The distinct advantage of TPP over conventional single-photon polymerization lies in its ability to fabricate complex three-dimensional structures with extremely high resolution and precision. The localized polymerization at the focal point of the laser minimizes scattering and allows for the construction of features that are smaller than the diffraction limit of the light.

Two-photon polymerization (TPP) achieves high-resolution fabrication critical for microscale and nanoscale structures. The resolution, including linewidth and voxel dimensions, in TPP is highly sensitive to several process parameters. These parameters, namely the numerical aperture of the objective (NA), the writing speed, the average laser power and exposure time are integral in determining the feature size, shape, and overall resolution of the microstructures[147]. The numerical aperture (NA) significantly affects the focusing capability of the laser beam, influencing the minimum feature size achievable. Higher NAs lead to a tighter focus, which allows for smaller feature sizes and higher resolution[148]. The speed at which the laser moves over the photoresist affects exposure time per unit area, impacting how thoroughly cross-linking occurs. Faster speeds can lead to less complete polymerization, thus affecting the structural integrity and resolution. The average laser power and exposure time determine the amount of energy delivered to the photoresist. Adequate

exposure ensures complete polymerization, while excessive exposure can lead to unwanted broadening of features due to overexposure.

Additionally, the choice of photoinitiator (PI) and two-photon polymerizable resin (TPPR) or photoresist (PR) plays a major role in the resolution of TPP-fabricated microstructures. The type of PI used influences the efficiency of two-photon absorption. PIs designed specifically for TPP can offer higher sensitivity and resolution due to their optimized absorption characteristics at the laser wavelength used. While, the molecular properties of the photo-resist (PR), including its viscosity, reactivity, and cross-linking density, affect how finely the resin can be structured. The composition of the resin determines its ability to resolve fine details without bleeding or spreading during the polymerization process.

Furthermore, the integration of various dopants into the photo-resist is employed to induce additional properties that are crucial for both the fabrication process and the functionality of the developed structures. These dopants can be organic dyes, carbon-based materials, magnetic nanoparticles, or metallic salts. Each type of dopant offers unique benefits. organic dyes like Rhodamine B and Methylene Blue, enhance the photosensitivity of the resin by increasing the efficiency of two-photon absorption. This improvement can lead to greater resolution and finer feature definition. They can also impart specific optical properties to the microstructures, such as fluorescence, which is useful in biomedical imaging and photonic devices. CNTs can improve the mechanical strength and thermal stability of the structures. Their high aspect ratio and conductivity also enhance the electrical properties of the resin. These structures are suitable for applications requiring robust mechanical properties and electrical conductivity, such as microelectromechanical systems (MEMS) and nano-electronic devices. Iron Oxide nanoparticle doping allows the structures to respond to magnetic fields, enabling controlled movement or alignment during and after fabrication. Theis magnetic responsiveness is particularly valuable in targeted drug delivery systems and in the creation of actuators and sensors.

The introduction of sensitizers to the photoinitiator (PI) mix can significantly augment the efficiency of the light absorption process, which is crucial for initiating polymerization. Sensitizers such as plasmonic nanoparticles (NPs), fluorescent NPs, or semiconductor quantum dots (QDs) play a pivotal role by enhancing the photophysical properties of the PI, leading to more effective and efficient polymerization at lower laser powers. CdSe/CdS seeded nanorods have facilitated the polymerization of hydroxyethyl acrylate, demonstrating not only enhanced polymerization efficiency but also the capability of the structures to act as fluorescent markers within the polymerized material. This dual functionality is particularly advantageous for applications in bioimaging and advanced material diagnostics[149]. Microstructures fabricated using two photon polymerization have been used in micro-optics [150, 151, 152] and micro-fluidic devices, transdermal drug delivery[153], bio-degradable cell scafolding and cell growth studies[154], and fabrication of NEMS and MEMS[155].

5.1.1 Basics of two photon polymerization

In 1930, Marie Göppert-Mayer introduced the concept of two-photon absorption (TPA) in her doctoral thesis. She posited that if the combined energies of two photons matched the energy gap between two electronic states within a material, it

would be feasible for the material to absorb light through a simultaneous two-photon process. This prediction laid the foundational principles for understanding nonlinear optical phenomena. Despite Göppert-Mayer's significant theoretical contributions, the experimental verification of TPA was not feasible at the time due to the lack of a light source intense enough to facilitate such phenomena. The invention of the laser in the 1960s provided the necessary high-intensity light source to explore and confirm these nonlinear optical effects. The first experimental demonstration of TPA occurred when physicist Werner Kaiser detected two-photon-excited fluorescence in a europium-doped crystal. This experiment validated Göppert-Mayer's theory and proved that materials could indeed absorb light through the mechanism of two-photon absorption. The confirmation of two-photon absorption opened up new avenues for the development two-photon microscopy which eventually paved way for the realization of Two-photon polymerization [156].

Two-photon absorption (TPA) is a nonlinear optical phenomenon utilized in Two-Photon Polymerization (TPP). The photoinitiator (PI) in TPP absorbs two photons simultaneously and transitions to an excited state, bypassing the need for higher-energy UV light exposure. Unlike linear absorption processes, TPA does not require each photon to individually match the energy needed to reach an excited state. Instead, the combined energy of the two photons must be sufficient to bridge this gap. The sum of the energies of the two absorbed photons must match the energy difference between the ground state and the desired excited state of the PI. This matching is critical as it dictates the wavelength of the light sources used in TPP and influences the efficiency of the photopolymerization process. The process includes a 'virtual intermediate state,' which is not an actual energy level within the molecule but a transient state that facilitates the energy absorption process. This intermediate state is crucial as it allows the molecule to effectively 'wait' for the second photon if the two photons do not arrive simultaneously. The existence of this intermediate state is extremely short-lived, typically on the order of a few femtoseconds. To successfully induce TPA, the two photons must be absorbed while the molecule is within this fleeting intermediate state. Ultra-short laser pulses, commonly in the femtosecond range, are crucial because they concentrate a high number of photons into a very brief burst of energy. This concentration increases the probability that two photons will interact with the PI or PS simultaneously or within the short lifetime of the intermediate state.

TPA occurs exclusively in regions where the light intensity is extremely high, typically at the focal point of a laser beam. This confinement to high-intensity light areas allows TPP to induce targeted photo-chemical and photo-physical changes within the material bulk and not just at the surface. This localized absorption also restricts the activation of the photoinitiators (PIs) to a very small volume in the order of femtoliters. Hence, creation of features that are smaller than the diffraction limit of light is possible, thereby surpassing traditional lithography limits. The resolution of the features can be considered in terms of Volumetric-Pixels or 'Voxel', which is the smallest volume polymerised by the activation of the photoinitiators (PIs).

The density of radicals, $\rho(r, z, t)$, generated by femtosecond laser pulses can be

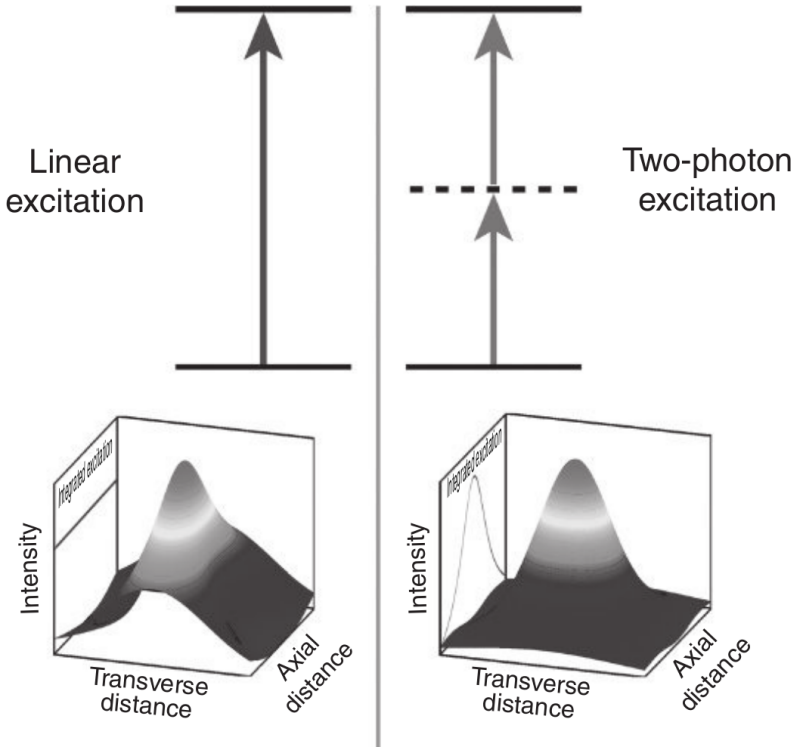

Figure 5.1. Linear and nonlinear absorption Energy-level diagrams are shown, with linear excitation on the left and two-photon excitation on the right. At the bottom are spatial intensity profiles in the center of the beam for both scenarios. Additionally, the profile of stimulated molecules integrated in the transverse direction is displayed to the left of each 3D plot. Figure taken from the reference [157]

determined by solving a basic rate equation.

$$\frac{\partial \rho}{\partial t} = (\rho_0 - \rho)\sigma_2 N^2, \tag{5.1}$$

where,

$$\sigma_2 = \sigma_2^a \eta$$

Here, σ_2 represents the effective two-photon cross-section for radical generation, while σ_2^a is the standard two-photon absorption cross-section. η, which is less than 1, indicates the efficiency of the initiation process. $N = N(r, z, t)$ is the photon flux, and ρ_0 is the density of the primary initiator particles.

The light distribution at the main maximum on the focal plane ($z = 0$) can be approximated by a Gaussian distribution, described as follows:

$$N(r, t) = N_0(t) exp\left(\frac{-2r^2}{r_0^2}\right) \tag{5.2}$$

The photon flux along the optical axis, $N_0(t) = N_0$, is assumed to be constant throughout the laser pulse duration because reaching the polymerization threshold typically requires multiple laser pulses. Ignoring any loss of radicals between laser

pulses, one can estimate the pixel diameter (d), defined as the area where the radical density $\rho(r, z)$ meets or exceeds the threshold ρ_{th}, as follows:

$$d(N_0, t) = r_0 \left[ln \left(\frac{\sigma_2 N_0^2 n \tau_L}{C} \right) \right] \tag{5.3}$$

where, $n = \nu t$ represents the number of pulses, with ν being the laser-pulse repetition rate, t the total processing-irradiation time, and τ_L the duration of each laser pulse. The constant C in this context is defined by the following equation:

$$C = ln[\rho_0(\rho_0 - \rho_{th})] \tag{5.4}$$

To estimate the maximum voxel length along the beam axis at $r = 0$, one can utilize the formula for the axial light distribution,

$$N(z) = N_0/(1 + z^2/z_R^2)$$

, which is typical for a Gaussian laser pulse. In this approximation, the pixel length l is determined by the following expression:

$$l(N_0, t) = 2z_R \left[\left(\frac{\sigma_2 N_0^2 n \tau_L}{C} \right)^{1/2} - 1 \right]^{1/2} \tag{5.5}$$

where z_R is the Rayleigh length.

By applying Equations (3.4) and (3.6), the diameter and length of a polymerized voxel can be calculated. Figure 5 presents a comparison between the predicted and measured data, with the left side showing the diameter and the right side showing the length. In this comparison, N_0 is substituted by the following term:

$$N_0 = \frac{2}{\pi r_0^2 \tau_L} \frac{P\Phi}{\nu \hbar \omega_L} \tag{5.6}$$

Here, P represents the average laser power, Φ is the fraction of light transmitted through the objective, and ω_L is the frequency of the laser light.

In Two-Photon Polymerization (TPP), the lateral resolution of fabricated lines is a critical metric that defines the level of detail and precision achievable in the microstructures. The lateral resolution or width of the fabricated line (w), can be mathematically expressed as follows [158]:

$$w = r_0 \left[ln \left(\frac{\sigma \left(\frac{\eta \rho_0}{\rho_t h} \right) \left(\frac{TP}{\hbar \omega_L} \right)^2}{\pi^{\frac{3}{2}} V_b \nu \tau_L r_0^3} \right) \right]^{\frac{1}{2}} \tag{5.7}$$

Where ν is the pulse repetition rate in MHz, V_b is scan speed in μm/s, τ_L is pulse width (in femtosecond), σ is the TPA cross-section of the PI, η is the two-photon quantum efficiency of the TPPR, r_0 is the laser beam waist radius, $\rho_t h$ is threshold photoacid concentration for initiation of polymerization,ρ_0 is the concentra- tion of photoacid generated, T is the fraction of light transmitted through the microscope objective, and P is the average laser power to the microscope.

From the equation presented above, it's clear that attaining optimal resolution for TPPR hinges on the critical interplay between composition and process parameters. This dependence extends to factors such as excitation wavelength, excitation power, exposure time or scan speed, the resin's monomer curability, quencher concentration, and the TPA cross-section of the PI. Conveniently, process parameters like laser dosage and exposure time or scan speed can be precisely managed using components within the TPP system. Moreover, TPPR formulation can be tailored to bolster its TPA cross-section, further enhancing resolution capabilities.

Hence, we can say that the efficiency of TPP is predominantly determined by three key factors: (1) Cross-Section (σ) of the Photosensitizer (PS), (2) PS / PI Energy Transfer Efficiency, (3) Quantum Efficiency of the Photoinitiator (PI). These factors interplay to dictate the success of the polymerization process and the quality of the resultant structures. The interdependence of these factors means that optimizing one without considering the others may not yield improvements in the overall efficiency of TPP. For example, a PS with a high two-photon absorption cross-section is less effective if the energy transfer to the PI is inefficient, or if the PI itself has low quantum efficiency. Thus, a balanced approach that considers the compatibility and performance of all three factors is essential for enhancing TPP outcomes. The resin formulation can be optimized by selecting a PI with a high quantum yield, ensuring that most of the absorbed energy leads to polymerization. This strategy can compensate for lower energy absorption rates and enhance the sensitivity and efficiency of the TPP process[159]. For a material to be effective as a two-photon polymerization resin (TPPR), it must exhibit specific properties that ensure efficient and precise polymerization, as well as durability and functionality of the final product. The essential characteristics required for an optimal TPPR can be listed as High Two-Photon Absorption (TPA) Cross-Section, High Quantum Yield of Radical Generation, Rapid Curability of Monomers, Good Mechanical Strength of the Crosslinked Chain, Optical Transparency to the Writing Wavelength [160]. These parameters ensure that polymerization only occurs at the focal point of the laser, avoiding unintended photochemical changes in the resin due to linear light interactions, reduced energy loss through non-productive pathways and provide a good mechanical stability to the structure.

Fine details typically require lower laser powers in two-photon polymerization (TPP) because of the nonlinear absorption involved and the risk of overexposure and damage when concentrating the laser into a smaller area. Damage to the features can happen if an area is exposed to the laser for too long, leading to heat accumulation and gas formation, often observed as bubbling during printing. This is a sign of suboptimal dosing conditions.

Two-Photon Polymerization (TPP) enables the fabrication of highly precise microstructures, but the resolution achieved can vary significantly between the x–y plane and the z-axis. This difference arises due to the nature of the optical focusing process involved in TPP. During TPP, the laser beam converges to a focal point where two-photon absorption occurs. Due to the focusing and defocusing of the beam before and after this focal point, the resultant polymerized voxel extends along the z-axis, creating a mirrored volume above and below the focal point. In contrast, the x–y dimensions of the voxel are confined more tightly to the beam waist, where the light intensity is highest. This results in higher resolution in the lateral plane

(x–y) compared to the axial direction (z). Traditional single-photon polymerization techniques are generally limited by diffraction to feature sizes of approximately half the wavelength of the incident light. However, TPP surpasses this limit by utilizing nonlinear absorption, allowing for feature sizes below 100 nm even when using a 780 nm light source. This significant reduction in feature size is possible because TPP confines the polymerization reaction to the very focal volume where two-photon absorption occurs[161].

5.1.2 TPP setup

Two-Photon Polymerization (TPP) systems are generally configured as "inverted microscopes." This setup is integral to achieving precise control over the photopolymerization process and optimizing the resolution of the fabricated microstructures. Objective lenses focus the femtosecond laser source into the desired region of the photoresist, where two-photon absorption induces photopolymerization. The selection of the objective lens significantly impacts the resolution and efficiency of the TPP process. Higher magnification objectives can achieve finer resolutions but may also increase the processing time. Various techniques are incorporated to enhance the precision and efficiency of the microfabrication process. Among these, oil immersion lithography and air interface lithography play critical roles, each with its own advantages and limitations. Oil immersion lithography uses an inert oil in contact with the objective lens and the photoresist. This approach helps to prevent potential damage to the objective lens, particularly when working with photoresists that contain solvents, strong acids, or bases. The oil used must have a refractive index matched to that of the substrate through which the microstructures are being printed. This matching is essential to avoid unnecessary diffraction and to maintain the accuracy of the laser focus. Air interface lithography operates at the air–photoresist interface. While this method avoids the need for immersion oil, it can introduce issues such as reflection interference from the photoresist surface, which can distort the laser focus and affect the precision of the printed structures. To mitigate reflection interference, the objective lens can be angled with respect to the substrate. This adjustment reduces the likelihood of reflective artifacts and enables more accurate and freeform printing of optical devices and other complex microstructures [162].

Our custom-designed two-photon polymerization setup is depicted in Figure 5.2. We utilize a near-infrared femtosecond fiber laser beam (FemtoFiber pro NIR, TOPTICA Photonics AG) with specific parameters: a center wavelength of 780 nm, a pulse width of 87 fs, a repetition rate of 80 MHz, and an optical power of 160 mW for TPP processes. Fabrication exposure is regulated by an optical shutter (SH). Laser power for fabrication is adjusted using a rotatable half-wave plate followed by a polarizing beam splitter cube (PBS). The laser beam is expanded by lenses L1 and L2 and directed onto a holographic spatial light modulator (SLM) (X10468-02, Hamamatsu Photonics). Simultaneously, lenses L3 and L4 enable the SLM to be in 4f conjugation with the back focal plane of a high numerical aperture oil immersion objective (Nikon Plan Apo Lambda 60x 1.4). The SLM facilitates the creation of multiple fabrication foci and enables wavefront correction on the fabrication beam. In the focal plane of L3, the zero and high diffraction orders are obstructed by

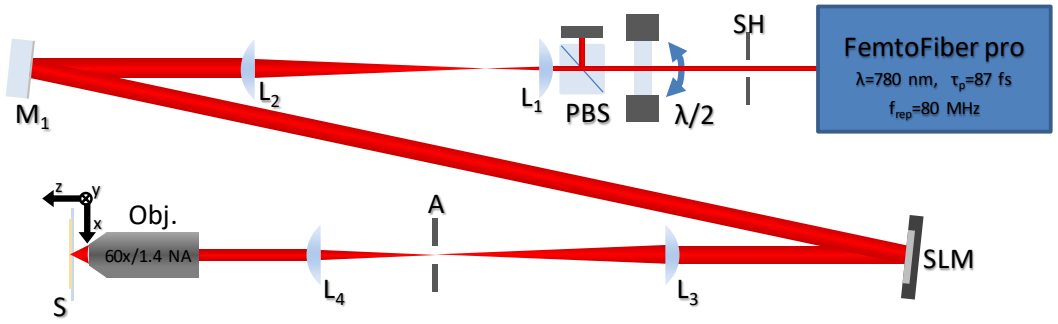

Figure 5.2. Schematic of coustom built TPP setup used for microfabrication Exposure during fabrication is toggled by an optical shutter (SH). The fabrication laser power is set by a rotatable half-wave plate followed by a polarizing beam splitter cube (PBS). After expansion by lenses L1 and L2 the laser beam is reflected onto a holographic spatial light modulator (SLM), which is in 4f conjugation to the back focal plane of a high numerical aperture oil immersion objective by lenses L3 and L4. The SLM is used to generate multiple fabrication foci and to impose wavefront correction on the fabrication beam. The zero and the high diffraction orders can be blocked in the focal plane of L3 by a thin wire and by an adjustable rectangular aperture (A). During fabrication the high NA focus of the laser is scanned inside a photoresist layer (S) carried on a microscope cover glass. Scanning is done by a 3-axis piezo translation stage. Figure taken from the reference [114]

a thin wire and an adjustable rectangular aperture (A). During fabrication, the high numerical aperture focus of the laser is scanned within a photoresist layer (S) situated on a microscope cover glass. This scanning in three dimensions is achieved using a 3-axis piezo translation stage (P563.3CD, Physik Instrumente (PI) GmbH Co. KG) controlled via a NI-DAQ DA card.

5.1.3 Epoxy based photo-resists

For the scope of this thesis and the studies included we limit ourself to the use of unmodified epoxy based polymers resins. Epoxy resins are well-known for their versatility and robustness, finding widespread use across various industries due to their exceptional mechanical properties, chemical resistance, and adhesive qualities. Their application extends into the realm of Two-Photon Polymerization (TPP), where these materials offer unique benefits for creating precise microstructures. They offer several advantages that make them ideal candidates for fabricating high-resolution microstructures and mechanical stability. Epoxy resins cure to form rigid, mechanically robust polymers. This rigidity is essential for maintaining the integrity of microstructures, particularly in applications requiring dimensional stability and load-bearing capacity. Their inherent resistance to thermal degradation and chemical attack ensures that the fabricated microstructures can withstand harsh environments, making them suitable for various industrial and biomedical applications. They can be formulated with photoinitiators type additives used that enable polymerization through two-photon absorption [163].

Epoxy resins typically require postprocessing baking steps to fully develop the microstructures after photopolymerization. The necessity for post-baking can in-

crease processing time and complexity, potentially limiting the rapid prototyping capabilities of TPP. One significant advantage of Epoxy resins is their low degree of shrinkage during polymerization. This property is crucial for applications where maintaining exact dimensions and structural integrity of the microfabricated components is essential. This low shrinkage makes Epoxy resins particularly appealing for fabricating microstructures that require high precision, such as in microelectromechanical systems (MEMS) and precision optical components. They polymerize through a ring-opening cationic polymerization process. While undergoing polymerization via the nucleophilic attack of the epoxide monomers on the cationic carbon, typically targeting the most substituted carbon, This reaction is facilitated by photoacid initiators rather than radical initiators. The presence of electron-withdrawing substituents on the epoxide ring can increase the susceptibility of the carbon-oxygen bond to nucleophilic attack, enhancing the reactivity of the monomer. Photoacid initiators generate acidic species upon exposure to light, initiating the cationic ring-opening polymerization of epoxy resins. This process is crucial for achieving the desired polymerization without the need for free radical generation[164].

Despite the additional processing steps required for epoxy resins, commercially available epoxide-based photoresists like SU-8 have been widely adopted for various applications due to their favorable properties. SU-8 is an epoxide-based negative photo-resist that is well-known for its high mechanical strength, chemical resistance, and ability to form thick, high-aspect-ratio structures. It has been extensively used in the fabrication of medical devices, microfluidic channels, and MEMS components due to its robustness and precision. The biocompatibility and structural integrity of SU-8 make it ideal for medical implants, sensors, and microfluidic devices and microrobotics where precise and reliable performance is crucial.

In our experiments, we employ commercial photoresist SU-8 2015, a negative, epoxy-based material commonly utilized for fabricating high-aspect ratio microstructures. Upon reaching the polymerization threshold, the extended molecular chains within SU-8 undergo crosslinking, resulting in a final microstructure resistant to development by commertially used SU-8 developer solutions.

5.2 Fabrication sample preparation

The substrate selected for generating SU-8 microstructures is a 24 mm $\times$ 32 mm soda lime glass coverslip. Ensuring a uniform and defect-free deposition of the photoresist requires the substrate surface to be completely free of dust and other contaminants.

In this procedure, the coverslips are immersed in a solution of sulfuric acid and Nochromix (5% w/v) for at least 24 hours. After soaking, the coverslips are carefully removed from the acid solution using stainless steel acid-proof tweezers and thoroughly rinsed with pure water. Immediately after rinsing, the coverslips are blow-dried using a hot air gun.

Wettability is crucial for ensuring that the photoresist spreads uniformly and forms strong chemical bonds with the surface molecules [165]. To enhance the wettability of the coverslips, a plasma treatment with oxygen at 1 bars for 10 minutes is applied. Post-treatment, the coverslips should be stored in a clean

container to avoid contamination from the atmosphere or oils from skin contact. Due to hydrophobic recovery, it is advisable to proceed with the next steps as soon as possible after the plasma treatment [166].

Dextran sacrificial layer

Experiments in this thesis involve the creation of free-floating microstructures. Usually, mechanical micromanipulators are used to detach microstructures from the substrate. However, this method is often slow and can potentially damage the structures.

An alternative method involves using a sacrificial layer to release microstructures. While conventional techniques for this purpose often require toxic chemicals, water-soluble polymers offer a safer and more efficient solution. These polymers can be easily applied through spin-coating, dissolve in water, and do not need corrosive reagents or organic solvents. Linder et al. showed that use of Dextran thin film as a water soluble sacrificial layer between the SU-8 and the glass substrate is a chemically stable and cost-effective choice [167].

To create the sacrificial layer, 2.5% w/v of dextran solution is spin-coated at 1000 rpm on the glass substrate right before the creation of SU-8 layer. The substrate is then placed on the hotplate at 95°C for 2 minutes to allow the film to dry. To prepare the dextran solution, dissolve 0.25 grams of dextran in 10 ml of double distilled water and place it in a hot water bath for 30 mins at 95°C and filter the solution using a 0.45 μm sterile syringe filter once it is cooled.

SU-8 spin-coating

Considering both the viscosity of SU-8 and its storage in a cold environment, it is crucial to allow the photoresist to reach room temperature before application to prevent bubble formation. Using a micropipette, 300 μL of SU-8 is evenly dispensed onto the coverslip, starting from the center and moving towards the corners. The sample is then placed as centrally as possible on the spin coater . The spin coating process involves two stages: 1) Spin at 500 rpm for 15 seconds to allow the viscous SU-8 to spread evenly across the coverslip. 2) Increasing the speed to 2000 rpm for 30 seconds to achieve a uniform layer.

After spin coating, the SU-8 layer reaches an approximate thickness of 25 μm. Any excess material on the edges of the coverslip is removed using lens paper. The samples are then stored in a clean, light-protected container until the soft bake process.

Throughout the photoresist application, it is essential to keep lights off to prevent premature exposure of the photoresist. This ensures the integrity and quality of the SU-8 layer before proceeding to the next steps.

Soft baking

The purpose of soft-baking the photoresist layer prior to exposure is to evaporate the remaining solvent from the spin coating process. Research has shown a strong correlation between solvent content and the aspect ratio of microstructures, indicating that maintaining around 7% solvent results in high fidelity microfabrication [168].

A hot plate was used for the soft-bake, offering several advantages over an oven. Heating from the bottom up with a hot plate promotes more efficient solvent evaporation, whereas an oven can create a hardened layer on the surface of the SU-8, slowing down solvent evaporation in the bulk.

Given the thickness of the photoresist layer obtained from spin coating, the soft-bake was conducted at 95°C, as recommended by the manufacturer. While the manufacturer suggests a soft-bake time of approximately 10 minutes, our optimization process indicated that a 30-minute bake was more effective. During calibration, it was observed that extending the bake to 2 hours produced high-aspect ratio microstructures. Consequently, a 2-hour soft-bake was established as the new standard.

After soft-baking, the samples are stored in a clean, light-protected container to prevent any premature exposure.

Post exposure baking

After the photoresist absorbs energy through two-photon absorption, the photoactive components in SU-8 are activated. However, additional energy from the post exposure baking is required to continue and complete the chemical reactions initiated during exposure. This step ensures the mechanical stability and proper cross-linking of the photoresist.

To manage the mechanical stress within the SU-8 photoresist, it is essential to heat and cool the sample gradually. So first, we set the hot plate to an initial temperature of 65°C and then gradually increase the temperature by 5°C per minute until reaching 95°C. Once 95°C is achieved, maintain this temperature for 7 minutes to ensure complete reaction of the photoactive components. After 7 minutes, turn off the hot plate but leave the sample on it to cool down gradually to room temperature.

This controlled heating and cooling process minimizes mechanical stress and ensures the integrity of the microstructures.

Development of microstructures

The development process is essential for removing the non-crosslinked SU-8 photoresist from the sample, revealing the microstructures on the substrate. Since SU-8 is a negative photoresist, the unexposed regions will dissolve during development, while the exposed regions remain polymerized. The SU-8 developer, primarily composed of propylene glycol monomethyl ether acetate (PGMEA), is used to dissolve the unlinked SU-8. To develop, submerge the sample with the fabricated microstructures in the SU-8 developer solution for 7 minutes. Then, transfer the sample to a fresh developer solution bath for an additional 7 minutes to ensure thorough removal of any remaining non-crosslinked photoresist.

5.3 Protocols for microbot post-processing

This section details an important protocol developed in the duration of this thesis. In the process of conducting the microbot experiments, it was noticed that the

microstructures have a high tendency of getting stuck to the sample surface. This can happen due to a combination of factors.

The dextran used for water soluble sacrificial layer can form filament-like structures that adhere to the glass as well as microbot surface. Another major contributor is the presence of salts in the bacterial growth medium. These salt ions can induce some strong attractive interactions between the structure and the sample surfaces. We therefore do not use salts while preparing any growth media.

As for dextran, the sample is plasma cleaned for 20 mins to remove the excess. In addition, the plasma treatment increases the wettability of the SU-8 microbots [169, 166]. We also coat the microbots with 10% BSA (Bovine Serum Albumin). This protein is used for surface passivation in microfluidic chips. BSA is adsorbed both on hydrophilic and hydrophobic surfaces, albeit with different mechanisms, but creates an outer passivation layer which is identical in both cases [170]. This results the microbot not being 'sticky' to the sample surfaces. For better both the sample surface and the microbot are coated with BSA. The BSA coating is carried out at 40°C to enhance the process [171].

However, to achieve this the microbots must be transferred to a different sample then the one where it has been fabricated. For this reason, the following protocol has been developed and adopted in the duration of the study.

Protocol for Microbot Post-processing

1. After development of the microbot, allow the fabrication sample to dry completely.

2. Place the microbot sample into the plasma cleaner and treat for 20 mins to remove extra dextran and to hydrophilize the surfaces.

3. seal the sample with a smaller top cover slip (9mm x 18mm), using 100μm spacers. Use the spacers in such a way as to create a small channel on the microbot sample, with the microbot in the center.

4. using a micro-pipette, slowly start filling up the channel on sealed sample with double distilled H_2O . Once the channel is filled start sucking out the water carefully from the other side of the channel using another micropipette. Repeat this channel washing process multiple times to be sure you've collected all the microbots and check this under a microscope. Collect the liquid containing microbots in a 1 ml eppendorf tube.

5. centrifudge the microbots in the eppendorf tube at 300 rcf for 5 mins. discard the supernatant while keping the bottom 100μl.

6. fill the eppendorf with 10% BSA solution and keep in an incubator at 40°C overnight.

7. before starting the experiment, again centrifudge the microbots in the eppendorf at 300 rcf for 5 mins while discarding the supernatant and keping the bottom 100μl. add 500μl of double distilled H_2O with 0.02% tween 20 and repeat the centrifudge step to wash away excess BSA.

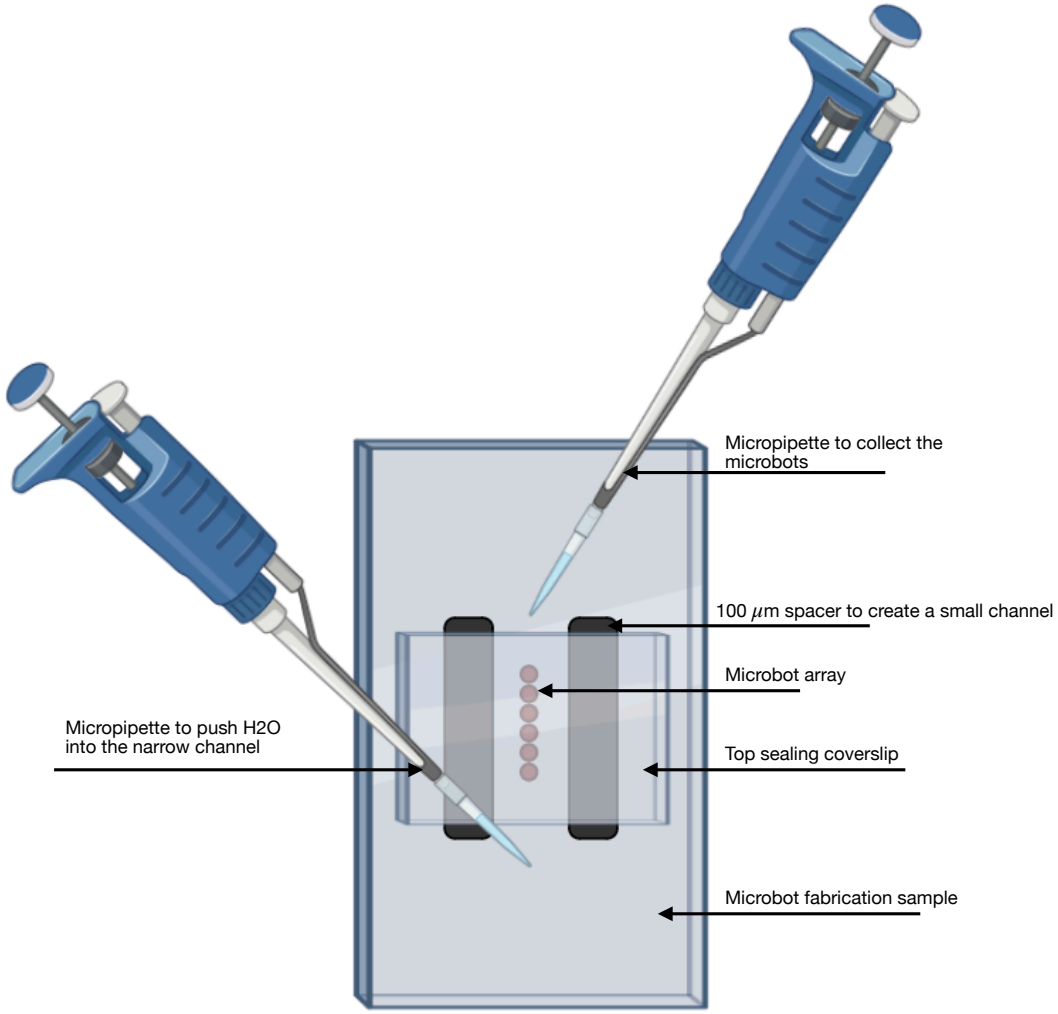

Figure 5.3. Illustration of channel on microbot fabrication sample to collect the microbots for BSA coating

8. add 2μl of the microbot dispersion to BSA coated leja slides before loading it with the bacterial motility buffer.

Chapter 6

Bacterial cultures

6.1 Cell culture

Bacteria, one of the earliest life forms on Earth, have evolved to thrive in a diverse array of environments. *Escherichia coli* (*E. coli*), in particular, can inhabit various substrates such as food, water, and the gut. Because environmental conditions significantly influence bacterial motility, it is crucial to select appropriate growth media and temperatures for laboratory studies based on the desired experimental outcomes.

Cultivating bacteria in a liquid medium is the most prevalent method due to the high bacterial yield and ease of harvesting. This process typically starts with a single, well-isolated colony picked from an agar plate to minimize variability within the bacterial culture. The selected colony is then inoculated into a fresh medium. The dynamics of bacterial growth in this culture can be segmented into four distinct phases.

Growth Phases

1. **Lag Phase:** This initial period is characterized by a lack of cell growth while bacteria produce the necessary molecular machinery to adapt to the new environment. Cellular activity is high as bacteria synthesize essential enzymes and adjust their metabolism, but there is little to no cell division.

2. **Log (Exponential) Phase:** During this phase, bacterial cell numbers increase exponentially through binary fission, with typical doubling times ranging from 20 minutes to 1 hour, depending on the growth conditions. This phase continues until the nutrient's energy yield in the medium decreases to a level that can no longer sustain exponential growth.

3. **Stationary Phase:** In this phase, the bacterial population stabilizes as the growth rate equals the death rate, resulting in a constant cell number. This equilibrium eventually breaks down as nutrients are depleted and waste products accumulate.

4. **Death Phase:** Over the long term, in the absence of nutrients, bacterial cells stop duplicating, and the number of live cells decreases. The decline phase

marks a significant reduction in the viable cell population due to the continued lack of resources and increasing toxicity from waste products.

To minimize the risk of growing contaminants and unwanted mutants along with the desired bacterial strain, it is crucial to supplement the growth medium with antibiotics to which the strain is resistant. Among the most commonly used growth media for motility experiments are tryptone broth (TB) and Luria-Bertani broth (LB). The nutrient energy yield of these media can influence the growth rate and the achievable density in the stationary phase, which is measurable via optical density (OD_{600})

The optical density at 600 nm is a common metric for estimating bacterial concentration in a culture. For *E. coli*, the OD_{600} in the low-density regime is directly proportional to the bacterial concentration. However, at higher densities, multiple scattering events disrupt this linear relationship, necessitating dilution of the culture to obtain reliable measurements. The preparation of *E. coli* for motility experiments involves several steps to ensure consistent cultures.

General Protocol for Preparing *E. coli* for Motility Experiments

1. **Inoculation and Initial Growth:** Streak a single colony of *E. coli* from a glycerol stock or previous plate onto a fresh agar plate containing the ampicillin antibiotic. Incubate the plate overnight at 33°C until individual colonies are visible.

2. **Overnight Culture Preparation:** Select a single, well-isolated colony from the agar plate to minimize culture variability. Inoculate the selected colony into 10 mL of LB medium containing ampicillin in 1:100 dilution ratio. Incubate the culture at 30°C with shaking at 180 rpm.

3. **Refresh Culture:** After 12 hours the culture has reached the saturation phase. A 1:100 dilution is prepared in a new fresh TB medium(5 mL) . This step should partially synchronize the cell cycle such to reduce the population variability. This refresh culture is grown at 30°C in a shaking incubator at 180 rpm.

4. **Motility buffer:** The cells are harvested after reaching late-exponential phase. This typically requires 5 hours after inoculation of refresh culture. One hour prior to harvesting, when the cell are still in the exponential phase, they are induced with 1μL of al-Trans Retinal and 10 μL of 1mM L-arabinose. After harvesting the cells, are placed in double-distilled water and 0.2% tween20 and centrifuged twice to removed al motility buffer. The OD of motility buffer is maintain at 1 so the bacteria can finish the oxygen in the sample in appropriate time. If you use the BSA coated microbot increase the bacteria density. This is because adding the microbot dispersion before the bacterial motility buffer will reduce th OD significantly in small channels, that hold just a few μliters of volume and are used in the microbot experiments.

6.2 Investigating bacterial speed using differential dynamic microscopy

In this experiment, we require the data about bacterial speed with reference to the intensity of green light shown. Due to a small but noticeable variability in the expression proteorhodopsin in daily experiments, we require accurate information regarding the bacterial speed. This information can be used to fine tune the intensity spectrum on the navigation algorithm. To investigate it we developed a routine by the use of Differential Dynamic Microscopy.

Differential Dynamic Microscopy (DDM) is a video-based analytical technique used to measure the dynamics of suspended particles by examining the fluctuations in pixel intensity over time [172]. Unlike traditional tracking methods that necessitate identifying individual particles, DDM utilizes dynamic light scattering principles. This allows for the simultaneous analysis of large populations of particles.

In 2011, Wilson and colleagues showcased the use of Differential Dynamic Microscopy (DDM) to investigate the motility of *E. coli*. By analyzing Differential Intensity Correlation Functions (DICFs) from video microscopy data, they measured the swimming speed distribution and the fraction of motile cells in *E. coli* suspensions [173].

Although this technique can be limited when bacteria exhibit complex and non-uniform behavior which requires advanced modeling and parameters fitting, in our case, where the bacteria are only smooth swimmers and can be fit into a relatively simple model.

In order to investigate the actual speed of bacteria at different intensity levels, we divided the field of view in six equal regions. Uniform green light of maximum saturation intensity is projected over the region of interest, for one minute before gathering any data. This makes sure that all motile bacteria have reached the saturation speed. Each of the six regions is shown different intensity of green light, starting from zero to maximum, increasing at each region by a step of 20%.

The images are acquired in Bright Field using a 4x objective (N.A. = 0.13), the same objective used for the experiments. Subsequently, DDM analysis was carried out on each of the six regions to gain an understanding of the best intensity level to be used for the experiments.

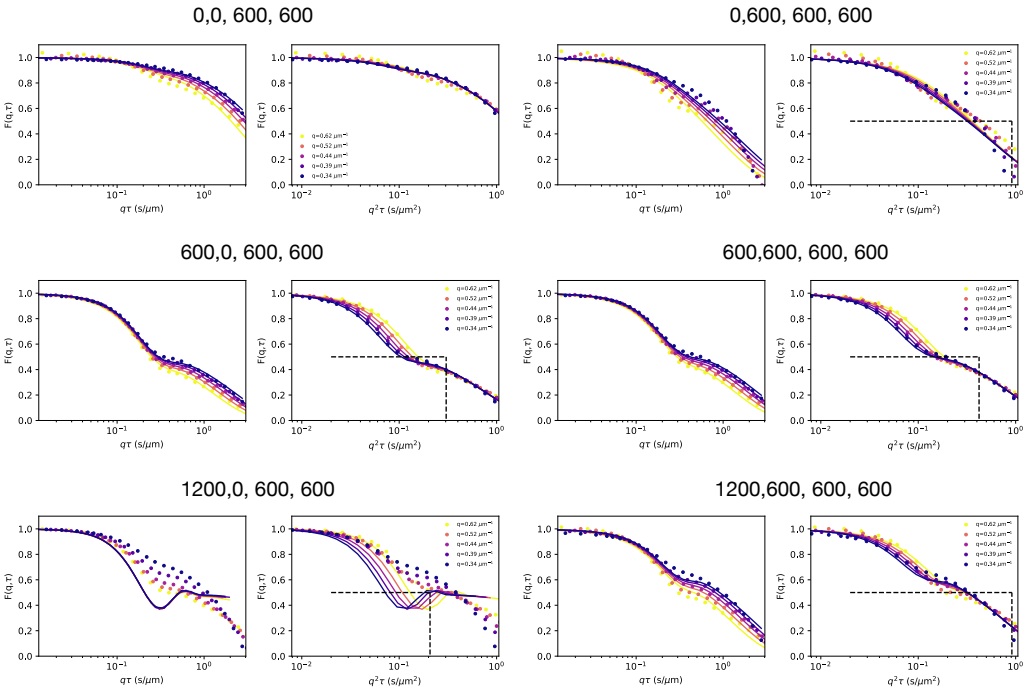

Figure 6.1. DDM analysis for 6 regions from the same field of view for optimizing green light intensity for the microbot experiment. Graphs are identified by the assigned region number

Chapter 7

Conclusion

One of the main challenges in the development of microrobots is consistent behavior and the ability to be controlled independently to perform complex tasks. The scaling effect of various forces on micron scaled system makes it difficult for such consistent behavior to occur. The independent control on other hand, using traditional methods like optical tweezers make these micro-robots extremely energy inefficient. The practicality of using these systems along with biological samples remains questionable due the possibility of destroying the sample.

Therefore, we focus on the development of low energy consuming, highly efficient bio-hybrid mechanism to control our microbots. In the first part of my PhD, I learned the handling and the basics of the two photon polymerization setup and development of precise 3D microfabricated synthetic structures. I also had to gain experience with proper handling of bacterial cultures and basics of gene editing and bacterial transformation.

Combing the bacterial motion and an optimized 3D microfabricated chassis we were able to get a moving microstructures powered by light driven bacteria. These microbots use light-driven bacteria as propellers, allowing them to be steered by varying light intensity on different parts of the microbot. A feedback loop involving a central computer projects custom light patterns to guide each microbot independently. Multiple such microbot were able to navigate through a series of predetermined check points by the means of an autonomous tracking and intensity control algorithm which efficiently calculates the linear and angular distances between the microbot and the target coordinates. We were able to study and model the forces applied by the bacterial propellers and simulated trajectories of the microbot that are consistent with our experiments and designs. This design enables high efficiency, with the potential to control hundreds of microbots using minimal optical power.

Applications of targeted cargo delivery and studies in approximation of geometric optics was also carried out. While preliminary reports look promising, more research need to be carried out to determine it is a feasible approach for the microbot use. Other microstructures fabricated using the two photon polymerization were used to study bacteria motility and pressure in active systems.

Protocols developed during this thesis regarding the coating of SU8 microbots with BSA for surface passivation can be applied to other such microrobotic systems that posses the tendency to stick to surfaces in microfluidic environments.

Overall, the field of biohybrid microrobotics has many open questions regarding the problem of guidance and control, due to the diverse environments in which the systems operate and the actuation methods available to them. This leaves scope for a lot of fascinating research topics to be investigated in future.

Bibliography

[1] Islam SM Khalil, Herman C Dijkslag, Leon Abelmann, and Sarthak Misra. Magnetosperm: A microrobot that navigates using weak magnetic fields. *Applied Physics Letters*, 104(22), 2014.

[2] Xiaoguang Dong and Metin Sitti. Controlling two-dimensional collective formation and cooperative behavior of magnetic microrobot swarms. *The International Journal of Robotics Research*, 39(5):617–638, 2020.

[3] Junyang Li, Xiaojian Li, Tao Luo, Ran Wang, Chichi Liu, Shuxun Chen, Dongfang Li, Jianbo Yue, Shuk-han Cheng, and DJSR Sun. Development of a magnetic microrobot for carrying and delivering targeted cells. *Science robotics*, 3(19):eaat8829, 2018.

[4] Stefano Palagi, Andrew G Mark, Shang Yik Reigh, Kai Melde, Tian Qiu, Hao Zeng, Camilla Parmeggiani, Daniele Martella, Alberto Sanchez-Castillo, Nadia Kapernaum, et al. Structured light enables biomimetic swimming and versatile locomotion of photoresponsive soft microrobots. *Nature materials*, 15(6):647–653, 2016.

[5] Mark Jayson Villangca, Darwin Palima, Andrew Rafael Banas, and Jesper Glückstad. Light-driven micro-tool equipped with a syringe function. *Light: Science & Applications*, 5(9):e16148–e16148, 2016.

[6] Shuailong Zhang, Erica Y Scott, Jastaranpreet Singh, Yujie Chen, Yanfeng Zhang, Mohamed Elsayed, M Dean Chamberlain, Nika Shakiba, Kelsey Adams, Siyuan Yu, et al. The optoelectronic microrobot: A versatile toolbox for micromanipulation. *Proceedings of the National Academy of sciences*, 116(30):14823–14828, 2019.

[7] Yo Tanaka, Keisuke Morishima, Tatsuya Shimizu, Akihiko Kikuchi, Masayuki Yamato, Teruo Okano, and Takehiko Kitamori. An actuated pump on-chip powered by cultured cardiomyocytes. *Lab on a Chip*, 6(3):362–368, 2006.

[8] Janna C Nawroth, Hyungsuk Lee, Adam W Feinberg, Crystal M Ripplinger, Megan L McCain, Anna Grosberg, John O Dabiri, and Kevin Kit Parker. A tissue-engineered jellyfish with biomimetic propulsion. *Nature biotechnology*, 30(8):792–797, 2012.

[9] John T Sauls, Sarah E Cox, Quynh Do, Victoria Castillo, Zulfar Ghulam-Jelani, and Suckjoon Jun. Control of bacillus subtilis replication initiation during physiological transitions and perturbations. *MBio*, 10(6):10–1128, 2019.

[10] Metin Sitti and Diederik S Wiersma. Pros and cons: Magnetic versus optical microrobots. *Advanced Materials*, 32(20):1906766, 2020.

[11] Jake J Abbott, Zoltan Nagy, Felix Beyeler, and Bradley J Nelson. Robotics in the small, part i: microbotics. *IEEE Robotics & Automation Magazine*, 14(2):92–103, 2007.

[12] Yaozhen Hou, Huaping Wang, Rongxin Fu, Xian Wang, Jiangfan Yu, Shuailong Zhang, Qiang Huang, Yu Sun, and Toshio Fukuda. A review on microrobots driven by optical and magnetic fields. *Lab on a Chip*, 23(5):848–868, 2023.

[13] David L Christensen, Elliot W Hawkes, Srinivasan A Suresh, Karen Ladenheim, and Mark R Cutkosky. μtugs: Enabling microrobots to deliver macro forces with controllable adhesives. In *2015 IEEE International Conference on Robotics and Automation (ICRA)*, pages 4048–4055. IEEE, 2015.

[14] Minjeong Jang, Chan Kyung Park, and Nae Yoon Lee. Modification of polycarbonate with hydrophilic/hydrophobic coatings for the fabrication of microdevices. *Sensors and Actuators B: Chemical*, 193:599–607, 2014.

[15] Michel Wautelet. Scaling laws in the macro-, micro-and nanoworlds. *European Journal of Physics*, 22(6):601, 2001.

[16] Orphee Cugat, Jerome Delamare, and Gilbert Reyne. Magnetic micro-actuators and systems (magmas). *IEEE Transactions on magnetics*, 39(6):3607–3612, 2003.

[17] Alexandre Munnier and Thomas Chambrion. Generalized scallop theorem for linear swimmers. *arXiv preprint arXiv:1008.1098*, 2010.

[18] Edward M Purcell. Life at low reynolds number. In *Physics and our world: reissue of the proceedings of a symposium in honor of Victor F Weisskopf*, pages 47–67. World Scientific, 2014.

[19] Dennis Bray. *Cell movements: from molecules to motility*. Garland Science, 2000.

[20] David Kafkewitz. Physiology of the bacterial cell: a molecular approach. *BioScience*, 41(3):172–173, 1991.

[21] Jessica C Wilks and Joan L Slonczewski. ph of the cytoplasm and periplasm of escherichia coli: rapid measurement by green fluorescent protein fluorimetry. *Journal of bacteriology*, 189(15):5601–5607, 2007.

[22] Howard C Berg. *E. coli in Motion*. Springer, 2004.

[23] Eric Lauga and Thomas R Powers. The hydrodynamics of swimming microorganisms. *Reports on progress in physics*, 72(9):096601, 2009.

[24] Eric Lauga, Willow R DiLuzio, George M Whitesides, and Howard A Stone. Swimming in circles: motion of bacteria near solid boundaries. *Biophysical journal*, 90(2):400–412, 2006.

[25] Eric Lauga. Bacterial hydrodynamics. *Annual Review of Fluid Mechanics*, 48:105–130, 2016.

[26] AT Chwang and Th Y Wu. A note on the helical movement of micro-organisms. *Proceedings of the Royal Society of London. Series B. Biological Sciences*, 178(1052):327–346, 1971.

[27] Y Magariyama, S Sugiyama, K Muramoto, I Kawagishi, Y Imae, and S Kudo. Simultaneous measurement of bacterial flagellar rotation rate and swimming speed. *Biophysical journal*, 69(5):2154–2162, 1995.

[28] Sir James Lighthill. *Mathematical biofluiddynamics*. SIAM, 1975.

[29] Alberto Lolli, Giovanni Corsi, and Antonio DeSimone. Control and navigation problems for model bio-inspired microswimmers. *Meccanica*, 57(10):2431–2445, 2022.

[30] Yunkyong Hyon, Thomas R Powers, Roman Stocker, Henry C Fu, et al. The wiggling trajectories of bacteria. *Journal of Fluid Mechanics*, 705:58–76, 2012.

[31] Mark C van Loosdrecht, Johannes Lyklema, Willem Norde, and AJ Zehnder. Influence of interfaces on microbial activity. *Microbiological reviews*, 54(1):75–87, 1990.

[32] Rasika M Harshey. Bacterial motility on a surface: many ways to a common goal. *Annual Reviews in Microbiology*, 57(1):249–273, 2003.

[33] Allison P Berke, Linda Turner, Howard C Berg, and Eric Lauga. Hydrodynamic attraction of swimming microorganisms by surfaces. *Physical Review Letters*, 101(3):038102, 2008.

[34] Howard C Berg and Linda Turner. Chemotaxis of bacteria in glass capillary arrays. escherichia coli, motility, microchannel plate, and light scattering. *Biophysical Journal*, 58(4):919–930, 1990.

[35] Paul D Frymier, Roseanne M Ford, Howard C Berg, and Peter T Cummings. Three-dimensional tracking of motile bacteria near a solid planar surface. *Proceedings of the National Academy of Sciences*, 92(13):6195–6199, 1995.

[36] Darwin Palima and Jesper Glückstad. Gearing up for optical microrobotics: micromanipulation and actuation of synthetic microstructures by optical forces. *Laser & Photonics Reviews*, 7(4):478–494, 2013.

[37] Ada-Ioana Bunea and Jesper Glückstad. Strategies for optical trapping in biological samples: Aiming at microrobotic surgeons. *Laser & Photonics Reviews*, 13(4):1800227, 2019.

[38] Theodor Asavei, Timo A Nieminen, Vincent LY Loke, Alexander B Stilgoe, Richard Bowman, Daryl Preece, Miles J Padgett, Norman R Heckenberg, and Halina Rubinsztein-Dunlop. Optically trapped and driven paddle-wheel. *New Journal of Physics*, 15(6):063016, 2013.

[39] Shoji Maruo, Akira Takaura, and Yohei Saito. Optically driven micropump with a twin spiral microrotor. *Optics express*, 17(21):18525–18532, 2009.

[40] NK Metzger, M Mazilu, L Kelemen, P Ormos, and K Dholakia. Observation and simulation of an optically driven micromotor. *Journal of Optics*, 13(4):044018, 2011.

[41] Stefano Palagi, Dhruv P Singh, and Peer Fischer. Light-controlled micromotors and soft microrobots. *Advanced Optical Materials*, 7(16):1900370, 2019.

[42] M Pilz Da Cunha, Michael G Debije, and Albert PHJ Schenning. Bioinspired light-driven soft robots based on liquid crystal polymers. *Chemical Society Reviews*, 49(18):6568–6578, 2020.

[43] Hao Zeng, Piotr Wasylczyk, Diederik S Wiersma, and Arri Priimagi. Light robots: bridging the gap between microrobotics and photomechanics in soft materials. *Advanced Materials*, 30(24):1703554, 2018.

[44] Leilei Xu, Fangzhi Mou, Haotian Gong, Ming Luo, and Jianguo Guan. Light-driven micro/nanomotors: from fundamentals to applications. *Chemical Society Reviews*, 46(22):6905–6926, 2017.

[45] Katherine Villa and Martin Pumera. Fuel-free light-driven micro/nanomachines: Artificial active matter mimicking nature. *Chemical Society Reviews*, 48(19):4966–4978, 2019.

[46] Arthur Ashkin and James M Dziedzic. Optical trapping and manipulation of viruses and bacteria. *Science*, 235(4795):1517–1520, 1987.

[47] Michelle D Wang, Hong Yin, Robert Landick, Jeff Gelles, and Steven M Block. Stretching dna with optical tweezers. *Biophysical journal*, 72(3):1335–1346, 1997.

[48] Iddo Heller, Tjalle P Hoekstra, Graeme A King, Erwin JG Peterman, and Gijs JL Wuite. Optical tweezers analysis of dna–protein complexes. *Chemical reviews*, 114(6):3087–3119, 2014.

[49] Arthur Ashkin. Optical trapping and manipulation of neutral particles using lasers. *Proceedings of the National Academy of Sciences*, 94(10):4853–4860, 1997.

[50] Arthur Ashkin. History of optical trapping and manipulation of small-neutral particle, atoms, and molecules. *IEEE Journal of Selected Topics in Quantum Electronics*, 6(6):841–856, 2000.

[51] Miles Padgett and Roberto Di Leonardo. Holographic optical tweezers and their relevance to lab on chip devices. *Lab on a Chip*, 11(7):1196–1205, 2011.

[52] Steven L Neale, Michael P MacDonald, Kishan Dholakia, and Thomas F Krauss. All-optical control of microfluidic components using form birefringence. *Nature materials*, 4(7):530–533, 2005.

[53] Silvio Bianchi, Gaszton Vizsnyiczai, Stefano Ferretti, Claudio Maggi, and Roberto Di Leonardo. An optical reaction micro-turbine. *Nature communications*, 9(1):4476, 2018.

[54] Unė G Būtaitė, Graham M Gibson, Ying-Lung D Ho, Mike Taverne, Jonathan M Taylor, and David B Phillips. Indirect optical trapping using light driven micro-rotors for reconfigurable hydrodynamic manipulation. *Nature communications*, 10(1):1215, 2019.

[55] Xiaobin Zou, Qing Zheng, Dong Wu, and Hongxiang Lei. Controllable cellular micromotors based on optical tweezers. *Advanced Functional Materials*, 30(27):2002081, 2020.

[56] Roberto Di Leonardo, András Búzás, Lóránd Kelemen, Gaszton Vizsnyiczai, László Oroszi, and Pál Ormos. Hydrodynamic synchronization of light driven microrotors. *Physical review letters*, 109(3):034104, 2012.

[57] Jonathan Leach, Hasan Mushfique, Roberto Di Leonardo, Miles Padgett, and Jon Cooper. An optically driven pump for microfluidics. *Lab on a Chip*, 6(6):735–739, 2006.

[58] Xiao-Feng Lin, Guo-Qing Hu, Qi-Dai Chen, Li-Gang Niu, Qi-Song Li, Andreas Ostendorf, and Hong-Bo Sun. A light-driven turbine-like micro-rotor and study on its light-to-mechanical power conversion efficiency. *Applied Physics Letters*, 101(11), 2012.

[59] Shuailong Zhang, Bingrui Xu, Mohamed Elsayed, Fan Nan, Wenfeng Liang, Justin K Valley, Lianqing Liu, Qiang Huang, Ming C Wu, and Aaron R Wheeler. Optoelectronic tweezers: a versatile toolbox for nano-/micro-manipulation. *Chemical Society Reviews*, 51(22):9203–9242, 2022.

[60] Pei Yu Chiou, Aaron T Ohta, and Ming C Wu. Massively parallel manipulation of single cells and microparticles using optical images. *Nature*, 436(7049):370–372, 2005.

[61] Hyundoo Hwang and Je-Kyun Park. Optoelectrofluidic platforms for chemistry and biology. *Lab on a Chip*, 11(1):33–47, 2011.

[62] Ming C Wu. Optoelectronic tweezers. *Nature Photonics*, 5(6):322–324, 2011.

[63] Shuailong Zhang, Weizhen Li, Mohamed Elsayed, Jiaxi Peng, Yujie Chen, Yanfeng Zhang, Yibo Zhang, Moein Shayegannia, Wenkun Dou, Tiancong Wang, et al. Integrated assembly and photopreservation of topographical micropatterns (small 37/2021). *Small*, 17(37):2170193, 2021.

[64] Shuailong Zhang, Mohamed Elsayed, Ran Peng, Yujie Chen, Yanfeng Zhang, Jiaxi Peng, Weizhen Li, M Dean Chamberlain, Adele Nikitina, Siyuan Yu, et al. Reconfigurable multi-component micromachines driven by optoelectronic tweezers. *Nature communications*, 12(1):5349, 2021.

[65] Zhihan Chen, Jingang Li, and Yuebing Zheng. Heat-mediated optical manipulation. *Chemical reviews*, 122(3):3122–3179, 2021.

[66] Fengrui Liu, Zhigang Zhang, Yufeng Wei, Qingchuan Zhang, Teng Cheng, and Xiaoping Wu. Photophoretic trapping of multiple particles in tapered-ring optical field. *Optics express*, 22(19):23716–23723, 2014.

[67] Liguo Dai, Zhixing Ge, Niandong Jiao, and Lianqing Liu. 2d to 3d manipulation and assembly of microstructures using optothermally generated surface bubble microrobots. *Small*, 15(45):1902815, 2019.

[68] Liguo Dai, Daojing Lin, Xiaodong Wang, Niandong Jiao, and Lianqing Liu. Integrated assembly and flexible movement of microparts using multifunctional bubble microrobots. *ACS Applied Materials & Interfaces*, 12(51):57587–57597, 2020.

[69] Mariana Medina-Sánchez, Veronika Magdanz, Maria Guix, Vladimir M Fomin, and Oliver G Schmidt. Swimming microrobots: Soft, reconfigurable, and smart. *Advanced Functional Materials*, 28(25):1707228, 2018.

[70] Nazek El-Atab, Rishabh B Mishra, Fhad Al-Modaf, Lana Joharji, Aljohara A Alsharif, Haneen Alamoudi, Marlon Diaz, Nadeem Qaiser, and Muhammad Mustafa Hussain. Soft actuators for soft robotic applications: a review. *Advanced Intelligent Systems*, 2(10):2000128, 2020.

[71] Marc Hippler, Eva Blasco, Jingyuan Qu, Motomu Tanaka, Christopher Barner-Kowollik, Martin Wegener, and Martin Bastmeyer. Controlling the shape of 3d microstructures by temperature and light. *Nature communications*, 10(1):232, 2019.

[72] RAM Hikmet and DJ Broer. Dynamic mechanical properties of anisotropic networks formed by liquid crystalline acrylates. *Polymer*, 32(9):1627–1632, 1991.

[73] Dylan Shah, Bilige Yang, Sam Kriegman, Michael Levin, Josh Bongard, and Rebecca Kramer-Bottiglio. Shape changing robots: bioinspiration, simulation, and physical realization. *Advanced Materials*, 33(19):2002882, 2021.

[74] Yoshitsugu Hirokawa and Toyoichi Tanaka. Volume phase transition in a nonionic gel. *The Journal of chemical physics*, 81(12):6379–6380, 1984.

[75] Stefano Fusco, Mahmut Selman Sakar, Stephen Kennedy, Christian Peters, Rocco Bottani, Fabian Starsich, Angelo Mao, Georgios A Sotiriou, Salvador Pané, Sotiris E Pratsinis, et al. An integrated microrobotic platform for on-demand, targeted therapeutic interventions. *Adv. Mater*, 26(6):952–957, 2014.

[76] Hang Zhang, Ahmed Mourran, and Martin Möller. Dynamic switching of helical microgel ribbons. *Nano letters*, 17(3):2010–2014, 2017.

[77] Ahmed Mourran, Hang Zhang, Rostislav Vinokur, and Martin Möller. Soft microrobots employing nonequilibrium actuation via plasmonic heating. *Advanced Materials*, 29(2):1604825, 2017.

[78] Ivan Rehor, Charlie Maslen, Pepijn G Moerman, Bas GP Van Ravensteijn, Renee Van Alst, Jan Groenewold, Huseyin Burak Eral, and Willem K Kegel. Photoresponsive hydrogel microcrawlers exploit friction hysteresis to crawl by reciprocal actuation. *Soft Robotics*, 8(1):10–18, 2021.

[79] Christopher J Barrett, Jun-ichi Mamiya, Kevin G Yager, and Tomiki Ikeda. Photo-mechanical effects in azobenzene-containing soft materials. *Soft matter*, 3(10):1249–1261, 2007.

[80] Christian Ohm, Martin Brehmer, and Rudolf Zentel. Liquid crystalline elastomers as actuators and sensors. *Advanced materials*, 22(31):3366–3387, 2010.

[81] Timothy J White and Dirk J Broer. Programmable and adaptive mechanics with liquid crystal polymer networks and elastomers. *Nature materials*, 14(11):1087–1098, 2015.

[82] Haifeng Yu and Tomiki Ikeda. Photocontrollable liquid-crystalline actuators. *Advanced Materials*, 23(19):2149, 2011.

[83] Benjamin A Kowalski, Tyler C Guin, Anesia D Auguste, Nicholas P Godman, and Timothy J White. Pixelated polymers: directed self assembly of liquid crystalline polymer networks, 2017.

[84] Laurens T de Haan, Albertus PHJ Schenning, and Dirk J Broer. Programmed morphing of liquid crystal networks. *Polymer*, 55(23):5885–5896, 2014.

[85] Yuanyuan Shang, Jingxia Wang, Tomiki Ikeda, and Lei Jiang. Bio-inspired liquid crystal actuator materials. *Journal of Materials chemistry C*, 7(12):3413–3428, 2019.

[86] Daniele Martella, Sara Nocentini, Filippo Micheletti, Diederik S Wiersma, and Camilla Parmeggiani. Polarization-dependent deformation in light responsive polymers doped by dichroic dyes. *Soft Matter*, 15(6):1312–1318, 2019.

[87] Paolo Sartori, Rahul Singh Yadav, Jesús Del Barrio, Antonio DeSimone, and Carlos Sánchez-Somolinos. Photochemically induced propulsion of a 4d printed liquid crystal elastomer biomimetic swimmer. *Advanced Science*, page 2308561, 2024.

[88] S Nocentini, D Martella, DS Wiersma, and C Parmeggiani. Beam steering by liquid crystal elastomer fibres. *Soft Matter*, 13(45):8590–8596, 2017.

[89] Hao Zeng, Piotr Wasylczyk, Camilla Parmeggiani, Daniele Martella, Matteo Burresi, and Diederik Sybolt Wiersma. Light-fueled microscopic walkers. *Advanced Materials (Deerfield Beach, Fla.)*, 27(26):3883, 2015.

[90] Daniele Martella, Sara Nocentini, Dmitry Nuzhdin, Camilla Parmeggiani, and Diederik S Wiersma. Photonic microhand with autonomous action. *Advanced Materials*, 29(42):1704047, 2017.

[91] D Martella, Diego Antonioli, S Nocentini, DS Wiersma, Giancarlo Galli, Michele Laus, and C Parmeggiani. Light activated non-reciprocal motion in liquid crystalline networks by designed microactuator architecture. *RSC advances*, 7(32):19940–19947, 2017.

[92] Daniele Martella, Sara Nocentini, Diego Antonioli, Michele Laus, Diederik S Wiersma, and Camilla Parmeggiani. Opposite self-folding behavior of polymeric photoresponsive actuators enabled by a molecular approach. *Polymers*, 11(10):1644, 2019.

[93] Akihiro Nishiguchi, Hang Zhang, Sjren Schweizerhof, Marie Friederike Schulte, Ahmed Mourran, and Martin Moller. 4d printing of a light-driven soft actuator with programmed printing density. *ACS applied materials & interfaces*, 12(10):12176–12185, 2020.

[94] Leonardo Ricotti and Arianna Menciassi. Bio-hybrid muscle cell-based actuators. *Biomedical microdevices*, 14:987–998, 2012.

[95] Jianzhong Xi, Jacob J Schmidt, and Carlo D Montemagno. Self-assembled microdevices driven by muscle. *Nature materials*, 4(2):180–184, 2005.

[96] Jinseok Kim, Jungyul Park, Sungwook Yang, Jeongeun Baek, Byungkyu Kim, Sang Ho Lee, Eui-Sung Yoon, Kukjin Chun, and Sukho Park. Establishment of a fabrication method for a long-term actuated hybrid cell robot. *Lab on a Chip*, 7(11):1504–1508, 2007.

[97] Adam W Feinberg, Alex Feigel, Sergey S Shevkoplyas, Sean Sheehy, George M Whitesides, and Kevin Kit Parker. Muscular thin films for building actuators and powering devices. *Science*, 317(5843):1366–1370, 2007.

[98] Vincent Chan, Kidong Park, Mitchell B Collens, Hyunjoon Kong, Taher A Saif, and Rashid Bashir. Development of miniaturized walking biological machines. *Scientific reports*, 2(1):857, 2012.

[99] Brian J Williams, Sandeep V Anand, Jagannathan Rajagopalan, and M Taher A Saif. A self-propelled biohybrid swimmer at low reynolds number. *Nature communications*, 5(1):3081, 2014.

[100] Sung-Jin Park, Mattia Gazzola, Kyung Soo Park, Shirley Park, Valentina Di Santo, Erin L Blevins, Johan U Lind, Patrick H Campbell, Stephanie Dauth, Andrew K Capulli, et al. Phototactic guidance of a tissue-engineered soft-robotic ray. *Science*, 353(6295):158–162, 2016.

[101] Sylvain Martel, Mahmood Mohammadi, Ouajdi Felfoul, Zhao Lu, and Pierre Pouponneau. Flagellated magnetotactic bacteria as controlled mri-trackable propulsion and steering systems for medical nanorobots operating in the human microvasculature. *The International journal of robotics research*, 28(4):571–582, 2009.

[102] Metin Sitti. Voyage of the microrobots. *Nature*, 458(7242):1121–1122, 2009.

[103] Sylvain Martel. Bacterial microsystems and microrobots. *Biomedical microdevices*, 14:1033–1045, 2012.

[104] Matthew R Edwards, Rika Wright Carlsen, and Metin Sitti. Near and far-wall effects on the three-dimensional motion of bacteria-driven microbeads. *Applied Physics Letters*, 102(14), 2013.

[105] Sung Jun Park, Seung-Hwan Park, Sunghoon Cho, Deok-Mi Kim, Yeonkyung Lee, Seong Young Ko, Yeongjin Hong, Hyon E Choy, Jung-Joon Min, Jong-Oh Park, et al. New paradigm for tumor theranostic methodology using bacteria-based microrobot. *Scientific reports*, 3(1):3394, 2013.

[106] Ajay Vikram Singh, Zeinab Hosseinidoust, Byung-Wook Park, Oncay Yasa, and Metin Sitti. Microemulsion-based soft bacteria-driven microswimmers for active cargo delivery. *ACS nano*, 11(10):9759–9769, 2017.

[107] Jiang Zhuang and Metin Sitti. Chemotaxis of bio-hybrid multiple bacteria-driven microswimmers. *Scientific reports*, 6(1):32135, 2016.

[108] John M Pawelek, K Brooks Low, and David Bermudes. Bacteria as tumour-targeting vectors. *The lancet oncology*, 4(9):548–556, 2003.

[109] Zeinab Hosseinidoust, Babak Mostaghaci, Oncay Yasa, Byung-Wook Park, Ajay Vikram Singh, and Metin Sitti. Bioengineered and biohybrid bacteria-based systems for drug delivery. *Advanced drug delivery reviews*, 106:27–44, 2016.

[110] Byung-Wook Park, Jiang Zhuang, Oncay Yasa, and Metin Sitti. Multifunctional bacteria-driven microswimmers for targeted active drug delivery. *ACS nano*, 11(9):8910–8923, 2017.

[111] Ouajdi Felfoul, Mahmood Mohammadi, Samira Taherkhani, Dominic De Lanauze, Yong Zhong Xu, Dumitru Loghin, Sherief Essa, Sylwia Jancik, Daniel Houle, Michel Lafleur, et al. Magneto-aerotactic bacteria deliver drug-containing nanoliposomes to tumour hypoxic regions. *Nature nanotechnology*, 11(11):941–947, 2016.

[112] Lief Fenno, Ofer Yizhar, and Karl Deisseroth. The development and application of optogenetics. *Annual review of neuroscience*, 34:389–412, 2011.

[113] Giacomo Frangipane, Dario Dell'Arciprete, Serena Petracchini, Claudio Maggi, Filippo Saglimbeni, Silvio Bianchi, Gaszton Vizsnyiczai, Maria Lina Bernardini, and Roberto Di Leonardo. Dynamic density shaping of photokinetic e. coli. *Elife*, 7:e36608, 2018.

[114] Gaszton Vizsnyiczai, Giacomo Frangipane, Claudio Maggi, Filippo Saglimbeni, Silvio Bianchi, and Roberto Di Leonardo. Light controlled 3d micromotors powered by bacteria. *Nature communications*, 8(1):15974, 2017.

[115] Edward Steager, Chang-Beom Kim, Jigarkumar Patel, Socheth Bith, Chandan Naik, Lindsay Reber, and Min Jun Kim. Control of microfabricated structures

powered by flagellated bacteria using phototaxis. *Applied Physics Letters*, 90(26), 2007.

[116] Edward B Steager, Mahmut Selman Sakar, Dal Hyung Kim, Vijay Kumar, George J Pappas, and Min Jun Kim. Electrokinetic and optical control of bacterial microrobots. *Journal of Micromechanics and Microengineering*, 21(3):035001, 2011.

[117] Nicola Pellicciotta, Ojus Satish Bagal, Viridiana Carmona Sosa, Giacomo Frangipane, Gaszton Vizsnyiczai, and Roberto Di Leonardo. Light controlled biohybrid microbots. *Advanced Functional Materials*, 33(39):2214801, 2023.

[118] Sriram Ramaswamy. The mechanics and statistics of active matter. *Annu. Rev. Condens. Matter Phys.*, 1(1):323–345, 2010.

[119] Wouter D Hoff, Michael A van der Horst, Clara B Nudel, and Klaas J Hellingwerf. Prokaryotic phototaxis. *Chemotaxis: Methods and Protocols*, pages 25–49, 2009.

[120] Anselm Levskaya, Aaron A Chevalier, Jeffrey J Tabor, Zachary Booth Simpson, Laura A Lavery, Matthew Levy, Eric A Davidson, Alexander Scouras, Andrew D Ellington, Edward M Marcotte, et al. Engineering escherichia coli to see light. *Nature*, 438(7067):441–442, 2005.

[121] Oded Béja, L Aravind, Eugene V Koonin, Marcelino T Suzuki, Andrew Hadd, Linh P Nguyen, Stevan B Jovanovich, Christian M Gates, Robert A Feldman, John L Spudich, et al. Bacterial rhodopsin: evidence for a new type of phototrophy in the sea. *Science*, 289(5486):1902–1906, 2000.

[122] Jessica M Walter, Derek Greenfield, Carlos Bustamante, and Jan Liphardt. Light-powering escherichia coli with proteorhodopsin. *Proceedings of the National Academy of Sciences*, 104(7):2408–2412, 2007.

[123] Helena Massana-Cid, Claudio Maggi, Giacomo Frangipane, and Roberto Di Leonardo. Rectification and confinement of photokinetic bacteria in an optical feedback loop. *Nature Communications*, 13(1):2740, 2022.

[124] Kirill A Datsenko and Barry L Wanner. One-step inactivation of chromosomal genes in escherichia coli k-12 using pcr products. *Proceedings of the National Academy of Sciences*, 97(12):6640–6645, 2000.

[125] Jochen Arlt, Vincent A Martinez, Angela Dawson, Teuta Pilizota, and Wilson CK Poon. Painting with light-powered bacteria. *Nature communications*, 9(1):768, 2018.

[126] Sho C Takatori, Wen Yan, and John F Brady. Swim pressure: stress generation in active matter. *Physical review letters*, 113(2):028103, 2014.

[127] Frank Smallenburg and Hartmut Löwen. Swim pressure on walls with curves and corners. *Physical Review E*, 92(3):032304, 2015.

[128] A Kaiser, HH Wensink, and H Löwen. How to capture active particles. *Physical review letters*, 108(26):268307, 2012.

[129] Ping Wang, Lydia Robert, James Pelletier, Wei Lien Dang, Francois Taddei, Andrew Wright, and Suckjoon Jun. Robust growth of escherichia coli. *Current biology*, 20(12):1099–1103, 2010.

[130] Segun Goh, Roland G Winkler, and Gerhard Gompper. Noisy pursuit and pattern formation of self-steering active particles. *New Journal of Physics*, 24(9):093039, 2022.

[131] François A Lavergne, Hugo Wendehenne, Tobias Bäuerle, and Clemens Bechinger. Group formation and cohesion of active particles with visual perception–dependent motility. *Science*, 364(6435):70–74, 2019.

[132] John Happel, Howard Brenner, John Happel, and Howard Brenner. Wall effects on the motion of a single particle. *Low Reynolds number hydrodynamics: with special applications to particulate media*, pages 286–357, 1983.

[133] Wenqi Hu, Kelly S Ishii, Qihui Fan, and Aaron T Ohta. Hydrogel microrobots actuated by optically generated vapour bubbles. *Lab on a Chip*, 12(19):3821–3826, 2012.

[134] Marcel Gerhard, Ashreya Jayaram, Andreas Fischer, and Thomas Speck. Hunting active brownian particles: Learning optimal behavior. *Physical Review E*, 104(5):054614, 2021.

[135] J Quetzalcoatl Toledo-Marin, Denis Boyer, and Francisco J Sevilla. Predator-prey dynamics: Chasing by stochastic resetting. *arXiv preprint arXiv:1912.02141*, 2019.

[136] Tyler D Ross, Dino Osmanovic, John F Brady, and Paul WK Rothemund. Ray optics for gliders. *ACS nano*, 16(10):16191–16200, 2022.

[137] Alexandre P Solon, Yaouen Fily, Aparna Baskaran, Mickael E Cates, Yariv Kafri, Mehran Kardar, and Julien Tailleur. Pressure is not a state function for generic active fluids. *Nature physics*, 11(8):673–678, 2015.

[138] Ahmad K Omar, Zhen-Gang Wang, and John F Brady. Microscopic origins of the swim pressure and the anomalous surface tension of active matter. *Physical Review E*, 101(1):012604, 2020.

[139] Nicola Pellicciotta, Matteo Paoluzzi, Dario Buonomo, Giacomo Frangipane, Luca Angelani, and Roberto Di Leonardo. Colloidal transport by light induced gradients of active pressure. *Nature Communications*, 14(1):4191, 2023.

[140] Orsolya Sipos, Katalin Nagy, R Di Leonardo, and Peter Galajda. Hydrodynamic trapping of swimming bacteria by convex walls. *Physical review letters*, 114(25):258104, 2015.

[141] Silvio Bianchi, Filippo Saglimbeni, and Roberto Di Leonardo. Holographic imaging reveals the mechanism of wall entrapment in swimming bacteria. *Physical Review X*, 7(1):011010, 2017.

[142] SA Mallory, C Valeriani, and A Cacciuto. Curvature-induced activation of a passive tracer in an active bath. *Physical Review E*, 90(3):032309, 2014.

[143] William S Ryu, Richard M Berry, and Howard C Berg. Torque-generating units of the flagellar motor of escherichia coli have a high duty ratio. *Nature*, 403(6768):444–447, 2000.

[144] Jasmine A Nirody, Yi-Ren Sun, and Chien-Jung Lo. The biophysicist's guide to the bacterial flagellar motor. *Advances in Physics: X*, 2(2):324–343, 2017.

[145] Xiaobing Chen and Howard C Berg. Torque-speed relationship of the flagellar rotary motor of escherichia coli. *Biophysical journal*, 78(2):1036–1041, 2000.

[146] Péter Galajda and Pál Ormos. Complex micromachines produced and driven by light. In *Summaries of Papers Presented at the Lasers and Electro-Optics. CLEO'02. Technical Diges*, pages 634–635. IEEE, 2002.

[147] T-W Lee, Oleg Mitrofanov, and Julia WP Hsu. Pattern-transfer fidelity in soft lithography: The role of pattern density and aspect ratio. *Advanced Functional Materials*, 15(10):1683–1688, 2005.

[148] WH Teh, U Dürig, U Drechsler, CG Smith, and H-J Güntherodt. Effect of low numerical-aperture femtosecond two-photon absorption on (su-8) resist for ultrahigh-aspect-ratio microstereolithography. *Journal of applied physics*, 97(5), 2005.

[149] Lior Verbitsky, Nir Waiskopf, Shlomo Magdassi, and Uri Banin. A clear solution: semiconductor nanocrystals as photoinitiators in solvent free polymerization. *Nanoscale*, 11(23):11209–11216, 2019.

[150] Rui Guo, Shizhou Xiao, Xiaomin Zhai, Jiawen Li, Andong Xia, and Wenhao Huang. Micro lens fabrication by means of femtosecond two photon photopolymerization. *Optics express*, 14(2):810–816, 2006.

[151] Mangirdas Malinauskas, Holger Gilbergs, Albertas Žukauskas, Vytautas Purlys, Domas Paipulas, and Roaldas Gadonas. A femtosecond laser-induced two-photon photopolymerization technique for structuring microlenses. *Journal of optics*, 12(3):035204, 2010.

[152] R Houbertz, V Satzinger, V Schmid, Walter Leeb, and G Langer. Optoelectronic printed circuit board: 3d structures written by two-photon absorption. In *Organic 3D Photonics Materials and Devices II*, volume 7053, pages 42–54. SPIE, 2008.

[153] A Ovsianikov, B Chichkov, P Mente, NA Monteiro-Riviere, A Doraiswamy, and RJ Narayan. Two photon polymerization of polymer–ceramic hybrid materials for transdermal drug delivery. *International journal of applied ceramic technology*, 4(1):22–29, 2007.

[154] Frederik Claeyssens, Erol A Hasan, Arune Gaidukeviciute, Demetra S Achilleos, Anthi Ranella, Carsten Reinhardt, Aleksandr Ovsianikov, Xiao Shizhou, Costas Fotakis, Maria Vamvakaki, et al. Three-dimensional biodegradable structures fabricated by two-photon polymerization. *Langmuir*, 25(5):3219–3223, 2009.

[155] Oliver Vanderpoorten, Quentin Peter, Pavan K Challa, Ulrich F Keyser, Jeremy Baumberg, Clemens F Kaminski, and Tuomas PJ Knowles. Scalable integration of nano-, and microfluidics with hybrid two-photon lithography. *Microsystems & nanoengineering*, 5(1):40, 2019.

[156] WGCGB Kaiser and CGB Garrett. Two-photon excitation in ca f 2: Eu 2+. *Physical review letters*, 7(6):229, 1961.

[157] Tommaso Baldacchini. *Three-dimensional microfabrication using two-photon polymerization: fundamentals, technology, and applications*. William Andrew, 2015.

[158] Shobha Shukla, Xavier Vidal, Edward P Furlani, Mark T Swihart, Kyoung-Tae Kim, Yong-Kyu Yoon, Augustine Urbas, and Paras N Prasad. Subwavelength direct laser patterning of conductive gold nanostructures by simultaneous photopolymerization and photoreduction. *Acs Nano*, 5(3):1947–1957, 2011.

[159] Raghvendra P Chaudhary, Arun Jaiswal, Govind Ummethala, Suyog R Hawal, Sumit Saxena, and Shobha Shukla. Sub-wavelength lithography of complex 2d and 3d nanostructures without two-photon dyes. *Additive Manufacturing*, 16:30–34, 2017.

[160] Arun Jaiswal, Chandresh Kumar Rastogi, Sweta Rani, Gaurav Pratap Singh, Sumit Saxena, and Shobha Shukla. Two decades of two-photon lithography: Materials science perspective for additive manufacturing of 2d/3d nano-microstructures. *Iscience*, 2023.

[161] Frank Burmeister, Sönke Steenhusen, Ruth Houbertz, Uwe D Zeitner, Stefan Nolte, and Andreas Tünnermann. Materials and technologies for fabrication of three-dimensional microstructures with sub-100 nm feature sizes by two-photon polymerization. *Journal of Laser Applications*, 24(4), 2012.

[162] Jiawen Li, Peter Fejes, Dirk Lorenser, Bryden C Quirk, Peter B Noble, Rodney W Kirk, Antony Orth, Fiona M Wood, Brant C Gibson, David D Sampson, et al. Two-photon polymerisation 3d printed freeform micro-optics for optical coherence tomography fibre probes. *Scientific reports*, 8(1):14789, 2018.

[163] Hongbo Gu, Chao Ma, Junwei Gu, Jiang Guo, Xingru Yan, Jiangnan Huang, Qiuyu Zhang, and Zhanhu Guo. An overview of multifunctional epoxy nanocomposites. *Journal of Materials Chemistry C*, 4(25):5890–5906, 2016.

[164] Simon Grabowsky, Tanja Schirmeister, Carsten Paulmann, Thomas Pfeuffer, and Peter Luger. Effect of electron-withdrawing substituents on the epoxide ring: an experimental and theoretical electron density analysis of a series of epoxide derivatives. *The Journal of Organic Chemistry*, 76(5):1305–1318, 2011.

[165] Michel Andre Aegerter and Martin Mennig. *Sol-gel technologies for glass producers and users*. Springer Science & Business Media, 2013.

[166] Joanna Izdebska-Podsiadły. Application of plasma in printed surfaces and print quality. In *Non-thermal plasma technology for polymeric materials*, pages 159–191. Elsevier, 2019.

[167] Vincent Linder, Byron D Gates, Declan Ryan, Babak A Parviz, and George M Whitesides. Water-soluble sacrificial layers for surface micromachining. *small*, 1(7):730–736, 2005.

[168] Henry Williams. Photophysical and photochemical factors affecting multi-photon direct laser writing using the cross-linkable epoxide su-8. 2013.

[169] Ferdinand Walther, Polina Davydovskaya, Stefan Zürcher, Michael Kaiser, Helmut Herberg, Alexander M Gigler, and Robert W Stark. Stability of the hydrophilic behavior of oxygen plasma activated su-8. *Journal of Micromechanics and Microengineering*, 17(3):524, 2007.

[170] Beata Sweryda-Krawiec, Halagowder Devaraj, George Jacob, and James J Hickman. A new interpretation of serum albumin surface passivation. *Langmuir*, 20(6):2054–2056, 2004.

[171] Jungyul Park, Il Chaek Kim, Jeongeun Baek, Misun Cha, Jinseok Kim, Sukho Park, Junghoon Lee, and Byungkyu Kim. Micro pumping with cardiomyocyte–polymer hybrid. *Lab on a Chip*, 7(10):1367–1370, 2007.

[172] Roberto Cerbino and Veronique Trappe. Differential dynamic microscopy: probing wave vector dependent dynamics with a microscope. *Physical review letters*, 100(18):188102, 2008.

[173] Laurence G Wilson, Vincent A Martinez, Jana Schwarz-Linek, J Tailleur, Gary Bryant, PN Pusey, and Wilson CK Poon. Differential dynamic microscopy of bacterial motility. *Physical review letters*, 106(1):018101, 2011.